UNIVERSIDADE
DE SANTIAGO
DE COMPOSTELA

CENTRO INTERNACIONAL DE ESTUDOS
DE DOUTORAMENTO E AVANZADOS
DA USC (CIEDUS)

TESE DE DOUTORAMENTO

A FIRST-PRINCIPLES STUDY AND SOME APPLIED RESEARCHES OF HIGH-TEMPERATURE SUPERCONDUCTORS AND OTHER LOW-DIMENSIONAL FUNCTIONAL MATERIALS.

Jose Lorenzo Castaño Verde

ESCOLA DE DOUTORAMENTO INTERNACIONAL

PROGRAMA DE DOUTORAMENTO EN CIENCIA DE MATERIAIS

SANTIAGO DE COMPOSTELA

ANO 2019


USC
UNIVERSIDADE
DE SANTIAGO
DE COMPOSTELA

DECLARACIÓN DO AUTOR/A DA TESE

A FIRST-PRINCIPLES STUDY AND SOME APPLIED RESEARCHES ON HIGH-TEMPERATURE SUPERCONDUCTORS AND OTHER LOW-DIMENSIONAL FUNCTIONAL MATERIALS

D. Jose Lorenzo Castaño Verde

Presento a miña tese, seguindo o procedemento axeitado ao Regulamento, e declaro que:

1) A tese abarca os resultados da elaboración do meu traballo.
2) De selo caso, na tese faise referencia ás colaboracións que tivo este traballo.
3) A tese é a versión definitiva presentada para a súa defensa e coincide coa versión enviada en formato electrónico.
4) Confirmo que a tese non incorre en ningún tipo de plaxio doutros autores nin de traballos presentados por min para a obtención doutros títulos.

En Santiago de Compostela, 7 de Maio de 2019

Asdo.
Jose Lorenzo Castaño Verde


USC
UNIVERSIDADE
DE SANTIAGO
DE COMPOSTELA

UNIVERSIDADE
DE SANTIAGO
DE COMPOSTELA

AUTORIZACIÓN DO DIRECTOR / TITOR DA TESE

A FIRST-PRINCIPLES STUDY AND SOME APPLIED RESEARCHES ON HIGH-TEMPERATURE SUPERCONDUCTORS AND OTHER LOW-DIMENSIONAL FUNCTIONAL MATERIALS

D. Manuel Vázquez Ramallo

INFORMA/N:

Que a presente tese, correspóndese co traballo realizado por D/Dna. ***Jose Lorenzo Castaño Verde****, baixo a miña dirección, e autorizo a súa presentación, considerando que reúne os requisitos esixidos no Regulamento de Estudos de Doutoramento da USC, e que como director desta non incorre nas causas de abstención establecidas na Lei 40/2015.*

En Santiago de Compostela, 12 de Maio de 2019

Asdo
Manuel Vázquez Ramallo


USC
UNIVERSIDADE
DE SANTIAGO
DE COMPOSTELA

Aos meus pais, á miña irmá
e aos meus avós.

Acknowledgments

Almost at the end of this stage, I would like to thank some people and institutions for their support and help. Without them this PhD thesis would have not been possible.

Firstly, I want to acknowledge Manuel V. Ramallo for the supervision of this thesis and his guidance in all the steps of this path. His scientific knowledge and his experience were crucial at every time to take decisions. His invaluable help and orientation have been pivotal to reach all the aims of this work.

I performed a very important part of this thesis in the University of Illinois at Urbana-Champaign (USA) in 2016 and 2017. I would like to express my gratitude to Professor Anthony James Leggett for all the advices related to the research work performed in the first part of the thesis. I also want to remark the kindness and the treatment that I have received from him during my two visits to Urbana. They were a key to help me to have a much more comfortable stay.

I would also like to acknowledge the rest of our research group for their support and help with experimental procedures. First of all, I would like to mention specially the help received by Jesus Mosqueira, that has been crucial to carry out the SQUID measurements, the evaporations and the deposition of the contacts in the samples. His advices have also been pivotal to perform the resistance measurements, and to analyze the SQUID measurements. I want also to thank Antonio Veira for the growth of the samples and for their experimental advices, that also have been a key contribution to finish this work. The other tenures of the group, Carolina, Carlos, and Jesús were also always available when I needed their help. I want also to thank Magdalena and Benito, the technicians of our group, for their inestimable help in all the experimental details of my work. Without their support, this work wouldn't have been possible.

También me gustaría aprovechar este espacio para mencionar a todos los doctorandos y estudiantes de trabajos de fin de grado y de fin de máster con los que he compartido despacho a lo largo de estos años. Quiero dar las gracias a Alberto Ramos, Juan Doval, Daniel Failde, Alejandro Gómez, Alberto Sebastián, y Martín Martínez por los buenos ratos pasados en el despacho estos años. Además, me gustaría mencionar con especial atención a Daniel Sóñora Vidal, con el que además de haber compartido estos años de despacho, mantengo una gran amistad desde que comenzámos juntos el grado en Física. Su compañía, y sus gustos musicales similares a los míos han ayudado a amenizar las largas horas en el despacho.

Por otro lado también quiero agradecer a todos mis companñeros y amigos doctorandos que han formado también parte de mi vida desde que empecé el grado en Física. En concreto, gracias a Manuel Blanco, Damián García, Javier Díaz, Manuel Feijoo, Juan Prieto, Víctor Vila y María Aymerich, por todas esas comidas, las películas que hemos ido a ver juntos al cine, y por todas las cenas que hemos compartido. Además, gracias a Daniel, Lucía, Amina y Eli por estar ahí también estos últimos años. No me olvido tampoco de personas como Pablo Lombao, Ángel Feiván, Henrique García y Simón Bujía, grandes amigos que escogieron otros caminos al terminar la carrera.

Me gustaría también agradecer por su apoyo a todas aquellas personas que no han tenido un papel directo en el devenir de mi investigacíon, pero que a través de su compañía han sabido darme el mejor de los apoyos a lo largo de todos estos años. En concreto, me gustaría agradecerle el apoyo a Alba Mariño su apoyo durante los últimos meses.

Finalmente, tengo que agradecer a mi familia todo el tiempo y esfuerzo que han invertido en mí durante todos estos años. Todos los posibles éxitos que pueda cosechar a lo largo de mi vida son en gran parte debidos a todos ellos. Gracias a mis padres, María de la Concepción Verde y Francisco Castaño por los valores que me han inculcado y la educación recibida. Gracias a mi hermana, que siempre ha sido y será un ejemplo para mí. Por último, quiero dar las gracias también a mis abuelos Marino Lorenzo Verde y Carmen Lusquiños, por todo su apoyo y cariño.

I acknowledge the financial support of the Spanish Ministry of Education for the FPU grant FPU14/00838, and the Xunta de Galicia for predoctoral grant. The research group has received support from the Spanish Ministry of Economy, Industry and Competitiveness MINECO (FIS2016-79109-P) and by the Xunta de Galicia under the programs Consolidación e Estruturación (2014-PG050 and PG

ED431C 2016/11) and Agrupacións Estratéxicas (AGRUP2015/11 and ED431E 2018/08). Also from the ESF-European Council Network COST Actions MP1201 (NanoSC) and CA16218 (Nanocohybri).


USC
UNIVERSIDADE
DE SANTIAGO
DE COMPOSTELA

"The people who do make big discoveries are the ones who somehow manage to free themselves from conventional ways of thinking and to see the subject from a new perspective"

Anthony James Leggett.

"Siempre que enseñes, enseña a dudar de lo que enseñes"

José Ortega y Gasset.

"Muchos años después, frente al pelotón de fusilamiento, el coronel Aureliano Buendía había de recordar aquella tarde remota en que su padre lo llevó a conocer el hielo"

Gabriel García Márquez.


USC
UNIVERSIDADE
DE SANTIAGO
DE COMPOSTELA

Contents

I: A FIRST-PRINCIPLES STUDY OF SOME INTERPLAYS BETWEEN STRUCTURAL AND SUPERCONDUCTING ENERGIES IN CUPRATE SUPERCONDUCTORS

II: SOME APPLIED RESEARCHES OF MICRO- AND NANO-STRUCTURED SUPERCONDUCTORS AND OTHER MATERIALS

IIA: SUPERCONDUCTING DEVICES

IIB: ELECTROSTATIC NANOSTRUCTURED MICROPOROUS MEDIA FOR NANOFLUID FILTRATION

Chapter 1

Introduction

This thesis presents research done with funding grants from Xunta de Galicia[1] and the Spain's Ministery of Education[2]. Both of these funding agencies required the research to include not only fundamental aspects but also applied studies. Correspondingly, this doctoral work comprises two parts:

Part I presents novel results using a first-principle study of the high-temperature cuprate superconductor (HTS) materials, performed in the framework of a collaboration with Professor A.J. Leggett, in whose laboratory I performed different stays[3].

The study presents an extension, to the case of HTS, of equations originally derived for simple superconductors by G.V. Chester. They link the energy saved by the superconductivity with the structural properties of the materials. Then, we apply these extended equations to various prototypical HTS.

Part II is devoted to various applied studies in different micro and nanostructured functional materials and devices. We divided these studies in two groups: In part IIA, we focus again on HTS and propose structuration designs that optimize their functionality as bolometric sensors of electromagnetic radiation (a development that led to our Spain's patent application coded P201930020) and we also study other structured HTS systems (2D dot-pattern structured films; hybrid superconductor+piezoelectric films).

In part IIB, we study instead electrostatic nanostructured micropore (ENM) media of the type recently introduced by industry in various forms (among other,

---

[1] predoctoral grant from Xunta de Galicia during 6 months.

[2] predoctoral FPU grant during 3.5 years.

[3] I performed a 1-month stay in 2016 and a second 3-month stay in 2017, both of them in the Institute of Condensed Matter Theory (ICMT) of the University of Illinois at Urbana-Champaign, USA, under the direct supervision of Professor A.J. Leggett.

nanoalumina-coated microporous membranes) for filtration of nanofluids (liquids carrying nanoentities in suspension). By employing model equations previously developed in Santiago de Compostela, we find microgeometry configurations able to optimize the energy efficiency and performance of filters based on such media.

We now present a brief but more detailed introduction to these different fundamental and applied researches:

- **Part I: First-principles study of the interplays between structural and superconducting energies in cuprate superconductors**

In contrast to the classic, BCS superconductors in which a phononic mechanism for Cooper pairing is well accepted and is thoroughly understood, [1] the high-temperature superconducting cuprates (and other complexly strongly-correlated superconductors) are still a fully open puzzle in what concerns the microscopic mechanism for superconducting pairing. [2, 3] Putting light, even if only partially, on such pairing mechanism remains of maximum interest. [4]

Probably due to the past success of the BCS theory, most part of the community has focused their attempts to explain this non-conventional materials trying to introduce some form of *effective* Hamiltonian, describing the system in terms of a few degrees of freedom (often different in each approach: phononic, different magnetic models, etc.) that, hopefully, could dominate the wide variety of phenomenology measured for this type of superconductivity. [5–8] However, until this date, no theory has arisen with a good level of acceptance in the research community able to explain all the relevant properties of these compounds. Moreover, most of these superconductors are complexly correlated electron systems, what means, among other features, that it could be expected to be hard, or even impossible, to reduce one of such effective Hamiltonians (for instance, taking into account the long-range part of the Coulomb interaction, believed to play an important role in HTS). [2]

All of this raises the issue of whether this is the only way to study this problem or if we should also try some other methodology.

Following this line of ideas, a different approach to the problem is to start from a first-principles general Hamiltonian and try to obtain the properties of the superconductor from it. The exact solution of all the statistical mechanics properties of the system is of course impossible to reach with today's computing power. However, it is possible to obtain directly from these approaches some general, but very important properties. [3, 9]

One promising way to seek information from the general Hamiltonian is focusing on the evolution of the general thermodynamic energy averages when changing from the normal to the superconducting state. [9–12] The basic thermodynamic energy to be studied is the thermal-averaged Hamiltonian, defined as the internal energy U. When one compound becomes superconducting, its internal energy should decrease, as this new state minimizes U.

Furthermore, the total Hamiltonian is a sum of different types of energies, with the easiest way to describe it being a sum of the kinetic energy of all the particles plus the Coulomb interaction energy of all of them. It would be also very informative to know how each of these thermal averaged energy contributions evolve from the normal to the superconducting state, so to more precisely pinpoint the energy contribution saved in the transition from the normal to the superconducting state. In fact, if we were able to know where in this sum is exactly the energy saved by the superconductivity, we could be able to discard any microscopic theories that do not lead to energy savings in the right contributions, so we can focus instead on new theories taking this important information into account.

For HTS, this approach is not entirely unheard, and at least one partially related new precedent is the discussion by different groups of some theory models [10–15] that explored the interlayer interactions as possible dominant drivers of the HTS superconducting transition. In particular, P.W. Anderson and coworkers [13–15] famously proposed the so-called interlayer-tunneling (ILT) model in which condensation reduces the out-of-plane kinetic energy of carriers. This lead to several experiments and theory comparisons [16–18] that mainly obtained that the interlayer kinetic energy saving in the conduction electrons is not strong enough to explain the condensation energy of these materials, indicating then that the ILT mechanism is not likely to be the dominant one for the superconducting condensation.

In related efforts, various groups have focused in the measurement of the energy savings from the normal to the superconducting state in HTS. [16, 19–22] For example, there were attempts to measure the total kinetic energy saving for the conduction electrons of the cuprates using the "single band" sum rule, in connection with tight binding models. [22, 23] These measurements showed varied behavior in the phase diagram of cuprates: for the very overdoped part superconductivity increased such kinetic energy; in the other part of the phase diagram, condensation was accompanied by savings in the kinetic energy of the conduction electrons strong enough to explain the condensation energy. [22]

A particularly relevant previous reference for our own efforts in this thesis is the MIR scenario introduced by A.J. Leggett [10–12] build over a first-principle Hamiltonian to which some general properties thought to be probably common to all the HTS are applied. [10–12] Among these assumptions, Leggett introduces the possibility of Coulomb energy saving in the region of the mid-infrared frequencies for HTS. In spite of relevant experimental efforts, [19–21] the scenario still remains experimentally untested. Still ongoing efforts could possibly be discriminative enough as to finally probe the relevance of the MIR scenario.

However, the Hamiltonian introduced by A.J. Leggett although being comparatively quite general, is still not an exact Hamiltonian. As an example, it does not take into account the kinetic energy of the nucleus in the system, that gives information about the role of the phonons in the superconducting mechanism. It has become quite frequent to discard this term in the Hamiltonian of HTS because of the general idea that the phonons play a residual role in the mechanism of superconductivity. This would be coherent with the common conjecture that the reason why the isotope effect seems to be negligible for the highest-T_c cuprate composition close to optimal doping, but appreciable elsewhere, is simply that a BCS (*i.e.*, phonon-induced) interaction contributes a doping-independent amount to the condensation energy. Then the BCS mechanism, and the isotope effect, would become negligible when other more relevant mechanisms produce high-T_c. However, beyond these rough qualitative arguments, a quantitative probe of the consistency of the phonon mechanism is still somewhat lacking.

In this thesis, we are going to study an even more general method to obtain information for cuprate superconductors, using the total Hamiltonian of the system. Our analysis is based on the method first introduced by G.V. Chester in 1956, before the appearance of the BCS theory to study the general evolution of the thermal averages of the kinetic energy of all the electrons of the system (conduction and non-conduction electrons), the kinetic energy of the nucleus in the system, and the total Coulomb energy (which includes the three interactions that play a role in the material, *i.e.*, the interaction between electrons, the repulsion between nucleus, and the attraction between nucleus and electrons). As common in 1956, Chester assumed in his work a monoatomic and type-I superconductor. [9]

In our study, we will adapt the Chester equations for the energy differences so to extend their validity to generic type-II polyatomic superconductors. Consequently, we employ a Hamiltonian for polyatomic materials that is a general sum of the three terms, *i.e.*, the kinetic energy of all the electrons of the system, the kinetic energy of the nucleus in the system, and the total Coulomb energy. Then we extend for this polyatomic case the three theorems employed in the original Chester formalism. Moreover, we express these equations in terms of the condensation energy of the system, so that the so-extended Chester-like equations are then valid also for type-II superconductors.

These analytical calculations are presented in Chapter 2, while in Chapter 3 we express them in terms of quantities for which measurements exist in some HTS. This leads to singularize, for instance, the kinetic energy of the oxygen nucleus, or to identify terms that seem to be negligible for HTS.

Also in Chapter 3, we quantify the energetic balances using experimental data available for three typical cuprate superconductors. [24–28] Our results indicate that the phononic contribution is not doping-independent, but rather evidence three different regions in the phase diagram: In the underdoped side, we find that the kinetic energy savings of the oxygen nucleus favors the superconductivity. In contrast, in the slightly overdoped side the movement of the oxygen nucleus opposes to the superconductivity and, finally, in the highly overdoped side the nucleus contribution is almost negligible.

- **Part IIA: Some applied researches on micro- and nano-structured superconductors**

As commented before, this doctoral work also comprises studies (mainly computational and/or experimental) devoted to the optimization of functional materials as used on devices or other applications. The first half of those studies focus again on HTS, while the second half will address different materials. Concerning our applied studies on HTS systems (part IIA of this thesis), they have addressed the optimization of HTS bolometric radiation sensing devices (what led us to the application of the Spain Patent No. P201930020). We also performed two additional complementary studies on 2D dot-patterned HTS and piezoelectric+HTS hybrid devices. We briefly introduce now these three contributions:

IIA.1- Design optimization of high-temperature superconducting bolometers using doping nanostructuration and 1D patterning

Bolometers are electromagnetic-radiation sensors that detect incident energy via the increase of the temperature T caused by the absorption of incoming photons. Sensors formed by an array of microsized bolometers (microbolometers) are often used, *e.g.*, for infrared cameras, detectors in quantum cryptography, astrophysics, satellites, aviation, etc, manily when high-sensitivity requirements are more important than raw cost. [29–34] Superconductors operating slightly above their transition temperature T_c are among the best candidate materials for bolometers, for their extreme sensitivity to T in an easy-to-measure observables such as the electrical resistance R (resistive transition-edge sensors, TES), and also for their wide spectral range, speed of response, and other competitive operational features.

A key figure influencing the efficiency is the so-called “temperature coefficient of resistance” or TCR, given by: [29–34]

$$\mathrm{TCR} = \left| \frac{1}{R}\frac{\mathrm{d}R}{\mathrm{d}T} \right|. \tag{1.1}$$

High bolometric sensitivity requires a large value of TCR. Resistive TES fabricated with low-T_c superconductors (the so-called low-T_c TES) achieve huge TCR$\sim 1000\,\mathrm{K}^{-1}$ or even more [29, 35] (for comparison, TCR of $\mathrm{V}_x\mathrm{O}_y$, the most common, and non superconducting material used for inexpensive bolometers, achieve TCR $\sim 0.025\,\mathrm{K}^{-1}$ [34]). This makes low-T_c TES a technology of choice for detecting the most faint radiations, as the cosmic microwave background. [29–31] However, the need of liquid-helium cryogenics evidently limits widespread adoption of low-T_c TES.

After the discovery of HTS, various authors have explored their use for bolometer sensors (the so-called HTS TES) with simpler liquid-nitrogen-based cryogenics. [36–41] $YBa_2Cu_3O_\delta$ (YBCO) is the HTS compound usually considered for this application, usually with maximum-T_c doping, *i.e.*, stoichiometry $\delta \sim 6.9$. As shown in References [36–41], YBCO thin films provide a viable competition to V_xO_y. Not only they provide much larger TCR $\sim 1.5\,\mathrm{K}^{-1}$ and low noise at an operational temperature $\sim 90\,\mathrm{K}$, but also they have a faster thermal response than V_xO_y. Moreover, the rest of parameters contributing to a large sensitivity (thermal conductivity, infrared absorbance, etc.) are also favorable or at least competitive with semiconducting bolometers. [36–41]

However, the HTS TES until now proposed still share some of the significant shortcomings of low-T_c TES: First, thermal stability of the cryogenic bath is still challenging (liquid-nitrogen systems are simpler but tend to thermally oscillate more than those based on liquid helium). Secondly, both types of TES have useful TCR only at the superconducting transition, corresponding to operational temperature intervals ΔT of just $\sim 0.1\,\mathrm{K}$ or less for low-T_c TES, and $\sim 1\,\mathrm{K}$ for the HTS TES proposed until now. [36–41] This makes them easy to saturate (low dynamic range).

The HTS TES systems proposed until today are homogeneous in nominal composition and critical temperature. [36–40] However, in the recent years different novel techniques have been developed to impose regular patterns to HTS thin films, creating custom designs, down to the micro- and the nano-scales. [42–47] This type of micro and nanostructuration of HTS has even become the main subject of two successive European COST actions (NanoSC and NANOCOHYBRI, [46]).

However, to our knowledge no author has up to now considered the possibility of designing a nanostructure pattern that could improve the performance as bolometer of a YBCO film.

In chapter 4 we address that task, using mainly computational methods. For that, we propose improvements of HTS TES ohmic-resistive microbolometers by considering the use of nanostructuring and patterning of the local doping level p (the number of carriers per unit cell). In particular, in our calculations we will consider the prototypical HTS compound YBCO, in which p may be easily varied by just changing the oxygen stoichiometry δ (*e.g.*, via local deoxygenation, ion bombardment with different masks, etc.) and we focus on 1D patternings (*i.e.*, p, or δ, varying along one direction). We concentrate in obtaining an increase of the operational temperature interval, ΔT, in which *i)* the TCR is large and *ii)* R is linear with T (*i.e.*, $\mathrm{d}R/\mathrm{d}T$ constant with T, that is another desirable feature that simplifies both the electronic control of the microbolometer and the required stability of the cryogenic setup). We propose several pattern designs that successively improve such ΔT and TCR (and also other bolometric parameters). Our most optimized design achieves a very competitive TCR$\sim$ 5K^{-1} and $\Delta T \sim 13\,\mathrm{K}$ (and led to our Spain patent application code P201930020).

IIA.2- Modification of the resistive transition width of high-temperature superconducting films using 2D T_c-dot pattterns

The above applied studies on 1D-patterned HTS film devices are supplemented in this thesis with two complementary studies. The first is devoted to show that the shape of the resistive transition of a HTS film may be also custom-tailored by using a 2D-pattern design (instead of the simpler, though effective, 1D-pattern used in the previous sections). We again use mainly computational approaches, and in this case we focus on achieving the opposite effect over the transition than the one achieved by our previous 1D-pattern: Now we seek the possibility of sharpening the transition (lowering ΔT) instead of broadening it. This may be of interest for some applied devices, like super-thermometers (sensitive inside a constrained window of temperatures T) [48] or resistive fault current limiters (as ΔT it may influence both the occurrence and speed of thermal avalanches and thus their ability to respond to ultrafast current strikes and their recovery time once the fault is cleared). [49, 50]

Our results in this study indicate that the resistive-transition sharpening may be achieved with certain 2D-dot patterns of T_c variation. Our most optimized designs lower ΔT by about 75% versus the non-structured YBCO films (and presumably would shorten in a similar amount the response time of a resistive fault current limiter).

IIA.3 Hybrid piezoelectric + high temperature superconducting devices

Our second complementary study of HTS viewed as functional materials is an experimental work. We have performed various measurements and characterizations of hybrid piezoelectric+HTS devices. These systems, fabricated in our research group in Santiago de Compostela, consist on a YBCO layer of about 100 nm thickness grown on top of a piezoelectric monocrystal ($\mathrm{Pb(Mg_{1/3}Nb_{2/3})_{0.72}Ti_{0.28}}$-$\mathrm{O_3}$). We have deposited electrical contacts on both sides of such hybrids, enabling us to exert custom externally-imposed voltage over the piezoelectric, that produces then custom mechanical strain over the HTS. Because strain induces a change of T_c in these superconductors, this opens a way to study (and/or functionally use) the variation of T_c with the mere application of an external voltage.

We have focused on the characterization of the strain that can be induced by applying a transversal (piezo)voltage, on the so-induced shift of the critical temperature, and on the thermal fluctuation effects (paraconductivity) in such devices.

• Part IIB: Some applied studies of functional nanofluid filters based on electrostatic nanostructured media

Part IIB of this thesis shifts the focus away from superconducting materials and devices, and addresses instead a different applied subject in the field of functional micro- and nano-structured materials. Such multifaceted thematics is a requirement of the agencies funding this work. Specifically, we study electropositive-nanostructured microporous materials, of the type recently introduced by academic researchers [51–57] and already commercialized by industry [58–60] as a media suitable for efficient filtration of nanofluids (*i.e.*, removal of nanoimpurities carried in suspension in a fluid that passes through a microporous electrostatic-nanostructured media). Our specific objective in this study will be to find micro-geometries that optimize the nanofiltration performance and energy efficiency (two aims not necessarily equivalent to each other). For that, we shall employ the theoretical model developed in 2013 in our group in Santiago de Compostela [61] and that provided a quantitative explanation for the enhanced nanofiltration performance observed [51–60] in this type of media. Specifically, we numerically compute, using such governing equations, (for which we conveniently discretized them also in this work), the filtration characteristic for different microgeometries, seeking the ones that provide either better nanoimpurity filtration percentage or better energy efficiency per filtered impurity. The first parameter is of obvious interest for some of the applications in which these media are being commercialized (virus removal and sampling, drinking water filtration, etc.) while for other applications it is the second parameter the one of more interest (energy efficiency is of key importance, *e.g.*, for large-scale industry effluents [4]).

Our results indicate, for instance, that decreasing-conical and sinusoidal-corrugated microconduits have better initial nanoimpurity removal rate (and longer operational lifetime, for most standard requirement criteria) than the one achieved by simple cylindrical microconduits. These geometries also improve the energy efficiency of the filtration (watts per spent removed nanoimpurity), with the decreasing-cone geometry particularly standing out in this respect.

---

[4] a typical application is the use of Ahlstrom-Argonide Nanoceram media to filter Toyota's car factories effluents in the USA since 2007. [62]

I: A FIRST-PRINCIPLES STUDY OF THE INTERPLAYS BETWEEN STRUCTURAL AND SUPERCONDUCTING ENERGIES IN CUPRATE SUPERCONDUCTORS

The work presented in this part of the manuscript corresponds to research mostly performed during two stays at Institute of Condensed Matter Theory (ICMT) of the University of Illinois at Urbana-Champaign, USA, under the direct supervision of Professor A.J. Leggett, and completed at Santiago de Compostela. This work is under preparation for publication.

Chapter 2

Calculations of a set of extended Chester equations for polyatomic type I or type II superconductors

Summary of the chapter:

We obtain new equations that generalize to polyatomic and type I or II superconductors the first principles formalism originally proposed by G.V. Chester (for monoatomic type I superconductors) for the kinetic and potential energy savings produced by a superconducting transition.

2.1 Introduction

Gaining insight the microscopic mechanisms behind the superconducting condensation of high-temperature cuprate superconductors (HTS) is still a fully open research topic. [4] In spite of the many efforts and models tried for these materials, nobody has obtained a theory that is able to explain successfully all the properties of this compounds. This situation is in no small part linked to the fact that these unconventional superconductors are strongly correlated electron systems, what means that it is hard to simplify their Hamiltonian to an effective one taking into account the long range part of the Coulomb interaction (that is believed to play an important role in HTS). [2] This even raises the issue of whether pursuing such effective-models is the perfect way to study this problem or if we should use other methodology.

There are many theoretical ways to try to explain the phenomena of superconductivity. Due to the appearance and success of the BCS theory, a great part of the community have focused their attempts to explain non-conventional superconductivity trying to use a similar approach, *i.e.*, introducing an effective Hamiltonian that is able to explain the wide variety of phenomenology measured for this type of superconductivity. [5–8]

However, there are other theoretical approaches that are useful to obtain information about what is the mechanism of superconductivity in these kind of compounds. In this context, an opposite approach to the problem is starting from a first-principles Hamiltonian and try to obtain the properties of the system from it. One way to obtain information from the general Hamiltonian of the system is focusing on the study of the evolution of the general thermodynamical energy averages from the normal to the superconducting state. [9–12] The basic thermodynamic energy to study is the thermal averaged Hamiltonian, defined as the internal energy U. When one compound becomes superconducting, this means that its internal energy should decrease, because this new state minimizes it. The study of the evolution of the change of the internal energy of the system between the normal and superconducting state have been deeply studied in HTS through the calculation of the condensation energy E_{cond} using specif heat measurements. [24–26, 64, 65]

However, the total Hamiltonian of a system is a sum of different types of energies. The easiest way to describe it is as a sum of the kinetic energy of all the particles of the system plus the Coulomb interaction energy of all the particles. It is also very informative to know how this thermal averaged partial energies evolve from the normal to the superconducting state, to know more precisely where is exactly the energy saved in the transition from the normal to the superconducting state.

Moreover, A.J. Leggett developed the MIR scenario, in which he introduces, starting from a first principles Hamiltonian, the possibility of a Coulomb energy saving in the region of the mid-infrared frequencies for HTS, that should be closely related with the superconducting mechanism. [10–12, 19] The partial Coulomb energy restricted to the region where the exchanged wave length verifies $\mathbf{q} \to 0$ has been recently measured using ellipsometry experiments. [19] They have found that in this region there is an energy saving only in the overdoped part of the cuprate phase diagram that is not strong enough to explain the condensation energy. Conversely, the underdoped side of the phase diagram shows an increase in the Coulomb energy. Very recent Electron Loss Espectroscopy experiments (EELS) have been performed to obtain the partial Coulomb energy saving at higher $\mathbf{q}$, showing a similar tendency in comparison to the ellipsometry measurements. [20, 21] To find where is the region where the Coulomb energy is saved, further EELS experiments at even higher $\mathbf{q}$ or at different frequencies should be performed.[1]

There where other attempts to measure the total kinetic energy saving within the tight binding model for the conduction electrons of the cuprates using a well known sum rule. [22] These measurements showed opposite behavior in some parts of the phase diagram of cuprates. For the very overdoped part of the phase diagram, there is a waste in kinetic energy. In the other part of the phase diagram, there is a saving in the kinetic energy of the conduction electrons that is strong enough to explain the condensation energy. [22]

In this chapter we are going to focus on a method that Chester developed before the appearance of the BCS theory to study the general evolution of the thermal averages of the Kinetic energy of all the electrons of the system (conduction and non-conduction electrons), the kinetic energy of the nucleus in the system, and the total Coulomb energy (which includes the three interactions that play a role in the material, *i.e.*, the interaction between electrons, the repulsion between nucleus, and the attraction between nucleus and electrons). [9] He developed these equations for a type I monoatomic material, and our aim is to extend the formalism for type I and type II polyatomic superconductors.

In this chapter, in Section 2.2, we introduce the Chester equations for the energy balances of a general monoatomic type I superconductor. In Subsection 2.2.1 we introduce the Chester Hamiltonian for a monoatomic superconductor, then in subsection 2.2.2 we write the three theorems used in the formalism. After that we introduce in subsection 2.2.3 the Chester equations for a monoatomic superconductor, that will be complemented in subsection 2.2.4 with the introduction of the thermodynamic equation for the Gibbs free energy variation from the nor-

---

[1] There are also some theories based in effective Hamiltonians that try to predict where is the energy saved in cuprate superconductors. The Interlayer Tunneling model (ILT) for HTS, developed by Anderson and coworkers, [13–15] introduces the hypothesis where there is a kinetic energy saving in the conduction electrons kinetic energy due to a Josephson coupling of the electrons between the superconducting CuO_2 planes. Subsequent measurements showed that this kinetic energy saving is not strong enough to explain the condensation energy of these materials. [17]

mal to the superconducting state for a generic type I superconductor. Then, in Section 2.3 we obtain the extend Chester equations for a general polyatomic superconductor at $T = 0\,\mathrm{K}$. To implement this we first introduce in subsection 2.3.1 a new thermodynamic quantity that is valid also for type II superconductors. Then we follow the same procedure, introducing the new Hamiltonian for polyatomic materials in subsection 2.3.2, introducing the theorems for the extended method in subsection 2.3.3, and obtaining the extended Chester equations in subsection 2.3.4. Finally we summarize our conclusions in section 2.4

2.2 A summary of the Chester equations for type I monoatomic superconductors

G.V. Chester proposed a general approach based on the study of the energy balances at temperatures below the superconducting transition. [9] He obtained within his calculations exact equations for the differences between the normal and superconducting states of the thermal averaged total Coulomb energy, the total thermal averaged kinetic energy of the electrons, and the total thermal averaged kinetic energy of all the nucleus of the material.

In this section we briefly summarize these original calculations, so to put ourselves in position to generalize them later in Section 2.3. As a general rule, and to make our presentation easier to follow, here we will state the main steps of such Chester equations. A full demonstration of such steps, we refer to either Chester original's work [9] or to our Section 2.3, in which we demonstrate the formalism in a generalized scenario.

2.2.1 Hamiltonian

G.V. Chester develops all the equations starting from a first-principles Hamiltonian $\mathscr{H}$ for a monoatomic superconductor, given by:

$$\mathscr{H} = K_{\mathrm{M}} + K_{\mathrm{m}} + \Phi, \tag{2.1}$$

where

$$K_{\mathrm{M}} = \sum_{i=1}^{N} \frac{\mathbf{P}_i^2}{2M}, \tag{2.2}$$

$$K_{\mathrm{m}} = \sum_{i=1}^{ZN} \frac{\mathbf{p}_i^2}{2m}, \tag{2.3}$$

$$\Phi = \sum_{i<j}^{N}\sum_{j}^{N} \frac{Z^2e^2}{|\mathbf{R}_i - \mathbf{R}_j|} - \sum_{i=1}^{N}\sum_{j=1}^{ZN} \frac{Ze^2}{|\mathbf{R}_i - \mathbf{r}_j|} + \sum_{i<j}^{ZN}\sum_{j}^{ZN} \frac{e^2}{|\mathbf{r}_i - \mathbf{r}_j|}. \tag{2.4}$$

In these equations, K_M is the total kinetic energy of the nucleus of the monoatomic material with mass M and atomic number Z, K_m is the total kinetic energy of the electrons with mass m and charge e, and Φ is the total Coulomb energy represented by the sum of the interaction energy between the electrons, the interaction energy between the nucleus and the interaction energy between the nucleus and the electrons of the material. Note that capital letters $\mathbf{P}$ and $\mathbf{R}$ are used to refer to the momentum and positions of the nucleus, respectively. Conversely, $\mathbf{p}$ and $\mathbf{r}$ are used to describe the momentum and the positions of the electrons, respectively. It is important to remark that this Hamiltonian should describe the phenomena of the superconductivity, because it take into account all the basic interactions that take place in the material at low energies.

2.2.2 Three intermediate theorems

Chester begins by demonstrating that this Hamiltonian verifies three generic theorems in quantum mechanics.

- **Contributions to $\overline{\mathscr{H}}$**

The first one comes just from the contributions to the Hamiltonian and is directly derived from Equation 2.1.

$$\overline{\mathscr{H}} = U = \overline{K}_{\mathrm{M}} + \overline{K}_{\mathrm{m}} + \overline{\Phi}, \quad (\overline{\mathscr{H}} \text{ contributions}) \tag{2.5}$$

where the bar stands for the thermal average calculated quantity.

- **Virial Theorem for $\overline{\mathscr{H}}$**

The second basic theorem is the virial theorem, that in this form is valid when the interparticle interaction is Coulomb-type (*i.e.*, each term of the sum is proportional to the inverse of the distance between articles), and for hydrostatic pressure.

$$PV = \frac{2}{3}(\overline{K}_{\mathrm{M}} + \overline{K}_{\mathrm{m}}) + \frac{1}{3}\overline{\Phi}, \quad (\text{virial theorem}) \tag{2.6}$$

where P is the pressure, and V is again the volume of the material.

- **Equation derived from Hellman Feynman theorem applied to $\overline{\mathscr{H}}$**

Finally, he uses a general result from statistical mechanics that comes almost directly from the application of the Hellman Feynman (HM) theorem to this

Hamiltonian. It introduces a relationship between the Gibbs free energy G and the total kinetic energy of the nucleus of the system, and is given by:

$$-M\left[\frac{\partial G}{\partial M}\right]_{T,P} = \overline{K}_{\mathrm{M}}. \quad \text{(derivation from HM theorem)} \tag{2.7}$$

2.2.3 Chester equations

Therefore, making the difference of all these quantities between the normal and superconducting state (represented by Δ), and expressing the internal energy and the volume in terms of the Gibbs Free energy, we obtain the Chester equations:

First Chester equation (electronic kinetic energy saving)

$$\Delta\overline{K}_{\mathrm{m}} = M\left[\frac{\partial \Delta G}{\partial M}\right]_{T,P} + T^2\left[\frac{\partial \Delta G/T}{\partial T}\right]_{P,M} + 4P\left[\frac{\partial \Delta G}{\partial P}\right]_{T,M} \quad (\mathrm{Chester} - 1) \tag{2.8}$$

Second Chester equation (nucleus kinetic energy saving)

$$\Delta\overline{K}_{\mathrm{M}} = -M\left[\frac{\partial \Delta G}{\partial M}\right]_{T,P} \quad (\mathrm{Chester} - 2) \tag{2.9}$$

Third Chester equation (Coulomb energy saving)

$$\Delta\overline{\Phi} = -2T^2\left[\frac{\partial \Delta G/T}{\partial T}\right]_{P,M} - 5P\left[\frac{\partial \Delta G}{\partial P}\right]_{T,M} \quad (\mathrm{Chester} - 2) \tag{2.10}$$

2.2.4 Thermodynamic equation

The three Chester equations are expressed in function of the difference between the normal and superconducting value of the Gibbs free energy ΔG. Therefore we need a way to measure this quantity for monoatomic superconductors. There is a well known thermodynamic equation for type I superconductors, that links this quantity with the critical magnetic field required to destroy the superconducting state H_c:

$$\Delta G = V\frac{H_c^2}{2}, \tag{2.11}$$

where V is the volume of the sample. Due to the fact that H_c is relatively easy to measure in type-I conventional low-Tc superconductors, it is convenient to calculate the energy balances with available experimental data of H_c, V, and some derivatives of them. Taking into account that all these magnitudes are measurable, we can obtain all these energy differences for a generic monoatomic type I superconductor and their dependence with Temperature. In fact, the results found within this approach are far more generic than the results of the BCS theory, because they are obtained from the real Hamiltonian of the system, instead of an effective one.

Chester achieves that the energy balance can be summarized in a Coulomb energy saving, an increase in the kinetic energy of the electrons, and also a saving in the kinetic energy of the nucleus. In fact, at 0K, the Coulomb energy saving perfectly balance the increase of the kinetic energy of the electrons. The final energy saving that leads to the condensation energy is explained by the kinetic energy saving in the movement of the nucleus, which is half of the value of the Coulomb saving at that temperature. This result remarks the importance of the phonons in the BCS superconducting mechanism.

2.3 Extended Chester equations for polyatomic type I or II superconductors

The question that is raised in this chapter is the possibility to adapt these equations to extract generic results for other types of superconductors, whose superconducting mechanisms are still unknown. There have been many attempts to obtain the energy balances in non conventional superconductors, [19,22] but these method has never been applied for these type of materials.

2.3.1 Thermodynamic equation for type I or II superconductors

The first step is to realize where are the assumptions in the Chester formalism that limit the equations for a type I monoatomic superconductor. First of all, it is hard to use the equation 2.11 for a type II superconductor, because the critical field H_c that destroys the superconductivity is not well defined due to the appearance of the vortex, that implies the definition of two critical fields H_{c1} and H_{c2}, that are not directly related with the Gibbs free energy saving without using any established theory or model. Therefore, is more natural to rewrite the equations in terms of a quantity that can be measured avoiding the problems related with the definition of H_c within a given theory. The most natural way is to choose the condensation energy as reference, because it can be obtained in an unambiguous way through specific heat measurements, [24–26, 64, 65] and is given by: [63]

$$E_{\text{cond}} = \overline{U}_n(T = 0K) - \overline{U}(T = 0K) =$$

$$-\int_0^\infty [C_n(T) - C(T)]\, dT = \int_0^\infty [S_n(T) - S(T)]\, dT, \tag{2.12}$$

where C is the measured electronic specific heat of the sample, S is the entropy, and n stands for the value in the normal state. However, the first conclusion that is raised from our thermodynamic equation is that to express our equations in terms of the condensation energy, we are going to fix all our energy balances at $T = 0\,\mathrm{K}$, limiting the scope of our extended formalism.

2.3.2 Hamiltonian for polyatomic superconductors

Another problem to use the Chester arguments is that the Chester Hamiltonian described by equation 2.1 is only valid for a monoatomic materials, and unconventional superconductivity is usually manifested in polyatomic materials. Therefore, we will rewrite the Hamiltonian like in equation 2.1 as a sum of three different energies, as:

$$\mathscr{H} = K_{\mathrm{M}} + K_{\mathrm{m}} + \Phi, \tag{2.13}$$

but these energies are now given by:

$$K_{\mathrm{M}} = \sum_{k=1}^{N_z} \sum_{i=1}^{N_k} \frac{\mathbf{P}_{ik}^2}{2M_{\mathrm{k}}}, \tag{2.14}$$

$$K_{\mathrm{m}} = \sum_{i=1}^{N_e} \frac{\mathbf{p}_i^2}{2m}, \tag{2.15}$$

$$\begin{aligned} \Phi \quad = \quad & \sum_{k=1}^{N_z} \sum_{k' \leq k}^{N_z} \sum_{i=1}^{N_k} \sum_{j=1}^{N_{k'}} \frac{Z_k Z_{k'} e^2}{|\mathbf{R}_{ik} - \mathbf{R}_{jk'}|} - \sum_{k=1}^{N_z} \sum_{i=1}^{N_k} \sum_{j=1}^{N_e} \frac{Z_k e^2}{|\mathbf{R}_{ik} - \mathbf{r}_j|} + \\ & \sum_{i=1}^{N_e} \sum_{i<j}^{N_e} \frac{e^2}{|\mathbf{r}_i - \mathbf{r}_j|}, \end{aligned} \tag{2.16}$$

where when $k = k'$ it is verified that $i < j$, N_z is the number of nucleus of different atomic number Z, and N_k is the number of nucleus of each type k. M_{k} is the mass of the nucleus of type k, N_e is the total number of electrons in the system, and Z_k is the atomic number of the nucleus of type k. In the last equation, the first summand is the nucleus-nucleus Coulomb energy, the second is the electron-nucleus Coulomb energy, and the third is the electron-electron Coulomb energy, in analogy with Equation 2.4.

2.3.3 Three intermediate theorems

- **Contributions to $\overline{\mathscr{H}}$**

From now, this is going to be the Hamiltonian that we are going to use in our calculations. First of all, it is direct to establish that the Equation 2.5 for the internal energy is still valid with this Hamiltonian because our new Hamiltonian can be represented also as a sum of three terms.

$$\overline{\mathscr{H}} = U = \overline{K}_{\mathrm{M}} + \overline{K}_{\mathrm{m}} + \overline{\Phi}, \quad (\overline{\mathscr{H}} \text{ contributions}) \tag{2.17}$$

- **Virial Theorem for $\overline{\mathscr{H}}$**

The generic expression for the virial theorem is given by:

$$-\frac{1}{2}\sum_{k=1}^{N_{\mathrm{tot}}} < \mathbf{F_k} \cdot \mathbf{r_k} >= \overline{K}_{\mathrm{M}} + \overline{K}_{\mathrm{m}}, \tag{2.18}$$

where $N_{tot} = \sum_k^{N_z} N_k + N_e$ is the sum of the total number of nucleus and electrons in the material, $\mathbf{F}_k$ is the total force over the particle k, the notation $<>$ stands also for the thermal averaged quantities and $\mathbf{r}_k$ is the position of the particle k. If we divide the external and internal forces (due to Coulomb repulsion or attraction), we obtain that:

$$-\frac{1}{2}\sum_{k=1}^{N_{tot}} < \mathbf{F}_{\mathbf{k}}^{\mathrm{ext}} \cdot \mathbf{r_k} >= \overline{K}_{\mathrm{M}} + \overline{K}_{\mathrm{m}} + \Xi, \tag{2.19}$$

where F_k^{ext} is the external force applied to the particle k and Ξ is the virial of interparticle forces for this Hamiltonian, given by:

$$\begin{aligned}
\Xi \;=\; & \sum_{k=1}^{N_z}\sum_{k'\leq k}^{N_z}\sum_{i=1}^{N_k}\sum_{j=1}^{N_{k'}} < (\mathbf{R}_{ik} - \mathbf{R}_{jk'}) \cdot \nabla_{\mathbf{R}_{ik}-\mathbf{R}_{jk'}} \frac{Z_k Z_{k'} e^2}{|\mathbf{R}_{ik} - \mathbf{R}_{jk'}|} > \\
& -\sum_{k=1}^{N_z}\sum_{i=1}^{N_k}\sum_{j=1}^{N_e} < (\mathbf{R}_{ik} - \mathbf{r}_j) \cdot \nabla_{\mathbf{R}_{ik}-\mathbf{r}_j} \frac{Z_k e^2}{|\mathbf{R}_{ik} - \mathbf{r}_j|} > + \\
& \sum_{i=1}^{N_e}\sum_{i<j}^{N_e} < (\mathbf{r}_i - \mathbf{r}_j) \cdot \nabla_{\mathbf{r}_i-\mathbf{r}_j} \frac{e^2}{|\mathbf{r}_i - \mathbf{r}_j|} >,
\end{aligned} \tag{2.20}$$

where when $k = k'$ it is verified that $i < j$. Due to the fact that the internal interaction forces are still of Coulomb type, it is easy to demonstrate that $\Xi = \Phi$, so this theorem is not affected by the fact that $\mathscr{H}$ is polyatomic, and we can write that:

$$-\frac{1}{2}\sum_{k=1}^{N_{tot}} < \mathbf{F}_{\mathbf{k}}^{\text{ext}} \cdot \mathbf{r}_{\mathbf{k}} >= \overline{K}_{\text{M}} + \overline{K}_{\text{m}} + \overline{\Phi}. \tag{2.21}$$

Here we have to deal with the type of external force that is being applied to the system. We are going to restrict by now to the hydrostatic pressure. Note that this virial theorem depends highly on the type of pressure, and here the anisotropy of the system plays an important role. Non hydrostatic are interesting cases to explore in further works. De differential external forces dF_i on the i-direction can be interpreted in terms of the stress tensor σ_{ik} as follows:

$$dF_i = -\sigma_{ik} dS_k, \tag{2.22}$$

where dS_k is the differential surface vector in the k-direction, and in the hydrostatic case the stress tensor is given by:

$$\sigma_{ik} = \begin{bmatrix} P & 0 & 0 \\ 0 & P & 0 \\ 0 & 0 & P \end{bmatrix}, \tag{2.23}$$

where P is the pressure in each of the faces of the material. So we can write the sum of equation 2.21:

$$-\frac{1}{2}\sum_{k=1}^{N_{tot}} < \mathbf{F}_{\mathbf{k}}^{\text{ext}} \cdot \mathbf{r}_{\mathbf{k}} >= \oint \sum_{i,k=1}^{3} r_i \sigma_{ik} dS_k, \tag{2.24}$$

where the integral goes through all the surface of the material. Taking into account the Gauss theorem:

$$\oint \sum_{i,k=1}^{3} r_i \sigma_{ik} dS_k = \sigma \int \nabla \cdot \mathbf{r} dV = 3PV. \tag{2.25}$$

Therefore we can conclude that we can use the same expression 2.6 for the virial theorem that Chester is using in his article for our more generic Hamiltonian:

$$PV = \frac{2}{3}(\overline{K}_{\text{M}} + \overline{K}_{\text{m}}) + \frac{1}{3}\overline{\Phi}, \quad \text{(virial theorem)} \tag{2.26}$$

- **Equation derived from Hellman Feynman theorem applied to $\overline{\mathscr{H}}$**

Finally we have to check that the equation for the third theorem is valid or if it has changed. The derivation is exactly the same, but now we have to take into account that we have different masses M_{k} for our different types of nucleus. We thus start from the partition function for the Gibbs Free energy:

$$Q = \sum_{V} \sum_{l} exp[-\beta(E_l(V) + PV)], \tag{2.27}$$

where E_l is the lth energy level of the system for a volume V, $\beta = 1/kT$. The equation that correlates it with the Gibbs Free energy:

$$G(T, P) = -kT \ln Q, \tag{2.28}$$

where k is the Boltzman's constant. The energy levels, $E_l(V)$, are the eigenvalues of our Hamiltonian. If ϕ_l are the eigenfunctions of this Hamiltonian, then:

$$\mathscr{H}\phi_l = E_l\phi_l. \tag{2.29}$$

If we apply the Hellmann-Feynman theorem [66] to the derivative of this energy eigenvalues respect to the nucleus mass M_{k} of an ion of type k, we get:

$$\frac{\partial E_l}{\partial M_{\mathrm{k}}} = \int_V \phi_l * \left(\frac{\partial \mathscr{H}}{\partial M_{\mathrm{k}}}\right) \phi_l dV. \tag{2.30}$$

Consequently we can write that:

$$-M_{\mathrm{k}} \frac{\partial E_l}{\partial M_{\mathrm{k}}} = (K_{M_{\mathrm{k}}})_{ll}, \tag{2.31}$$

where $K_{M_{\mathrm{k}}}$ is the partial kinetic energy of the nucleus of type k. Combining this relationship with equations 2.27, 2.28 and 2.31, we obtain that:

$$-M_{\mathrm{k}} \left(\frac{\partial G}{\partial M_{\mathrm{k}}}\right)_{T,P} = \sum_{V} \sum_{l} (K_{\mathrm{M_k}})_{ll} \exp[-\beta(E_l(V) + PV)]/Q = \overline{K}_{\mathrm{M_k}}, \tag{2.32}$$

and we can obtain the total kinetic energy of the nucleus.

$$-\sum_{k}^{N_z} M_{\mathrm{k}} \left(\frac{\partial G}{\partial M_{\mathrm{k}}}\right)_{T,P} = \sum_{k}^{N_z} \overline{K}_{\mathrm{M_k}} = \overline{K}_{\mathrm{M}}. \text{ (derivation from HM theorem)} \tag{2.33}$$

Thus we have re-derived the third theorem for our Hamiltonian needed to apply the Chester formalism.

2.3.4 Extended Chester equations

The Final step is to extend these equations to 0K, introduce the difference between the normal and superconducting state, and express the Gibbs free energy in terms of the condensation energy. Gibbs free energy is related with internal energy as given at $T = 0\,\mathrm{K}$:

$$G = U - PV. \tag{2.34}$$

Fixing the temperature to 0K, differentiating between the normal and superconducting state, and substituting definition 2.34 this into the equation 2.33 we have:

$$E_{\mathrm{cond}} = \Delta U = \Delta\overline{K}_{\mathrm{M}} + \Delta\overline{K}_{\mathrm{m}} + \Delta\overline{\Phi}, \tag{2.35}$$

$$3P\Delta V = 2(\Delta\overline{K}_{\mathrm{M}} + \Delta\overline{K}_{\mathrm{m}}) + \Delta\overline{\Phi}, \tag{2.36}$$

$$\sum_{k}^{N_z}\left[M_{\mathrm{k}}P\left(\frac{\partial\Delta V}{\partial M_{\mathrm{k}}}\right)_{T,P} - M_{\mathrm{k}}\left(\frac{\partial E_{\mathrm{cond}}}{\partial M_{\mathrm{k}}}\right)_{T,P}\right] = \Delta\overline{K}_{M}. \tag{2.37}$$

Therefore, to know the energy balances for each doping, we need to know the value of the condensation energy E_{cond}, the variation of the volume ΔV between the normal and superconducting state at $T = 0\,\mathrm{K}$, the variation of the condensation energy with the isotopic mass of each type of nucleus k, and the variation with the isotopic mass of the difference of the volume ΔV between the normal and superconducting state at $T = 0\,\mathrm{K}$. Solving these equations we obtain the extended Chester equations for any type of superconductor:

First extended Chester equation (electronic kinetic energy saving)

$$\Delta\overline{K}_{\mathrm{m}} = 3P\Delta V - E_{\mathrm{cond}} - \sum_{k}^{N_z}\left[M_{\mathrm{k}}P\left(\frac{\partial\Delta V}{\partial M_{\mathrm{k}}}\right)_{T,P} - M_{\mathrm{k}}\left(\frac{\partial E_{\mathrm{cond}}}{\partial M_{\mathrm{k}}}\right)_{T,P}\right], \quad (\mathrm{Chester} - 1) \tag{2.38}$$

Second extended Chester equation (nucleus kinetic energy saving)

$$\Delta\overline{K}_{\mathrm{M}} = \sum_{k}^{N_z}\left[M_{\mathrm{k}}P\left(\frac{\partial\Delta V}{\partial M_{\mathrm{k}}}\right)_{T,P} - M_{\mathrm{k}}\left(\frac{\partial E_{\mathrm{cond}}}{\partial M_{\mathrm{k}}}\right)_{T,P}\right], \quad (\mathrm{Chester} - 2) \tag{2.39}$$

Third extended Chester equation (Coulomb energy saving)

$$\Delta\overline{\Phi} = 2E_{\mathrm{cond}} - 3P\Delta V. \quad (\mathrm{Chester} - 3) \tag{2.40}$$

Note that these are exact equations to get the energy balance for any polyatomic superconducting material.

2.4 Conclusions

In this chapter, first we have reviewed a method developed by G.V. Chester that based in a first-principles Hamiltonian, three generic theorems that are verified by this Hamiltonian and in a thermodynamic relationship, to obtain the energy differences between the normal and superconducting state for a monoatomic type I superconductor.

After that, we have extended this method to obtain exact equations to calculate the energy differences between the normal and superconducting state at 0 K of the total averaged Coulomb energy, the total averaged kinetic energy of each type of nucleus within the system, and the total averaged kinetic energy of the electrons for any type of superconductor.

As we will exploit in the next chapter, these energy balances can be obtained through some measurements of the condensation energy, the change of the volume from the normal to the superconducting state, and some derivatives of them. It is important to remark that with this experimental data it is possible to calculate the energy balances for any type of superconductor, thanks to the generality of the formalism.

Chapter 3

Application of the extended Chester equations to cuprate superconductors

Summary of the chapter:

We apply the extended-Chester equations obtained in the previous chapter to the of high-temperature cuprate superconductors (HTS). For that, we first identify termns in such equations that become negligible in the HTS case, and the we introduce in the remaining terms available experimental information for three prototypical HTS components and doping ranges: $La_{2-\delta}Sr_{\delta}CuO_4$, $Bi_2Sr_2CaCu_2O_{8+\delta}$ and $Y_{0.8}Ca_{0.2}Ba_2Cu_3O_{7-\delta}$ (LSCO, Bi2212 and YCBCO, respectively). Our results suggest, for instance, that the kinetic energy of the oxygen nucleous significantly favours superconductivity in the underdoped HTS, and that the phononic contributions to pairing are doping-dependent.

3.1 Overview

We have remarked in the last subsection the importance of the formalisms based on first-principles in the understanding of the mechanism of non conventional superconductors. In this context we obtained the extended Chester equations to obtain the kinetic and Coulomb energy differences between the normal and superconductor state for any type of superconductor. This result has a broad application because it can be applied to any type of non conventional superconductor, to provide information about where is the energy saved in these compounds when the superconducting transition is reached.

One of the most important types of non conventional superconductors are the cuprate HTS. Despite the huge amount of experimental data collected for these compounds, and the important theoretical efforts to understand the nature of the microscopic mechanism, the microscopic theory that explains successfully all the properties of these complex compounds is still unknown.

In this chapter we have taken advantage of the experimental data obtained through these decades for these compounds to apply the extended Chester equations for these materials. With the experimental data available we are able to estimate the kinetic energy change of the oxygen nucleus between the normal and superconducting state for three typical cuprate superconductors for a wide part of their phase diagram. This is an important amount to measure the influence of the phonons in the superconducting mechanism. In this context, it is commonly believed that the reason why the isotope effect seems to be negligible for the highest-T_c cuprate composition close to optimal doping, but appreciable elsewhere, is simply that a BCS (*i.e.*, phonon-induced) interaction contributes a doping-independent amount to the condensation energy. Then the BCS mechanism, and the isotope effect, would become negligible when other more relevant mechanisms produce high-T_c. With our calculations we are able to discard this scenario, showing that the oxygen nucleus kinetic energy contributes a doping-dependent amount to the condensation energy in the phase diagram of cuprates. Moreover, we also calculate other energy balances and compare them with the BCS case within the possible.

For that, in Section 3 we adapt this equations for the HTS. We first calculate in Section 3.2 the order of magnitude of the terms of the extended Chester equations to discard the ones that are negligible in comparison to the condensation energy. After this, in Section 3.3 we analyze qualitatively the properties of the difference of kinetic energy of the oxygen nucleus through the phase diagram of HTS. Then, in Section 3.4 we calculate this value for three general HTS expressed as a fraction of the condensation energy. After that, in Section 3.5 we plot all the energy balances for these three cuprates obtained with the extended Chester equations and the available experimental data. Finally, we summarize our conclusions in Section 3.6.

3.2 Terms that may be estimated as quantitatively negligible for cuprates in the energy balance equations

In this section we are going to estimate first the order of magnitude, for cuprate HTS, of each term appearing in the extended Chester equations (Equations 2.38 to 2.40) with the aim to try to identify if any of them is small enough as to consider it negligible. Therefore, we are going to compare each term to the typical order of magnitude for the condensation energy ($\sim 1\,\mathrm{J/mol}$ for LSCO and $\sim 15\,\mathrm{J/mol}$ for Bi2212 and YBCO, see below). [24–26, 63–65]

To obtain the experimental values of each term, it should be measured the condensation energy of the material, the variation of the condensation energy with the isotope mass of each different nucleus in the superconductor, the variation of the volume from the normal to the superconducting state ΔV, and the variation of the volume of the sample with the isotopic mass. As we have explained before, it is possible to measure accurately the condensation energy with specific heat measurements. [24–26,63–65] Also, there is the possibility to measure it for different isotopes, to reach the first derivative of the condensation energy with the isotopic masses. Nevertheless, to the best of our knowledge, nobody has performed these experiments until now in cuprates (there exists measurements in other superconductors like MgB_2). [87]

Moreover, in relation to the other quantities, we are going to demonstrate that they are orders of magnitude smaller than the condensation energy, as it happened for derivatives $M_k P(\partial \Delta V/\partial M_k)_{T,P}$ in the first and second extended-Chester equations in the case of monoatomic type-I superconductors studied by G.V. Chester. [9]

First of all we are going to demonstrate that we can discard the terms that ate related to the derivative of the volume with the isotopic masses. To the best of our knowledge there is no data for this derivative for cuprate superconductors. However, it is reasonable to assume that the order of magnitude of this derivative is going to be the same for other material. The change in volume with the isotope mass have been measured for Iron. We are going to estimate the amount $M_{\mathrm{Fe}} P \partial V_{\mathrm{Fe}}/\partial M_{\mathrm{Fe}}$ taking into account that $(V_{\mathrm{Fe}_{208}} - V_{\mathrm{Fe}_{207}})/V_{\mathrm{Fe}_{207}} \sim 3\cdot 10^{-4}$, [78] where $M_{\mathrm{Fe_i}}$ is the mass of the isotope of lead with mass number i, V_{Fe} is the volume of the unit cell ($\sim (5\,\mathrm{Å})^3$). Taking these into account, for atmospheric pressure $P = 10^5$ Pa we have:

$$M_{\mathrm{Fe}} P \left(\frac{\partial V_{\mathrm{Fe}}}{\partial M_{\mathrm{Fe}}}\right)_{T,P} \sim \frac{V_{\mathrm{Fe}_{208}} - V_{\mathrm{Fe}_{207}}}{V_{\mathrm{Fe}_{207}}} \frac{V_{\mathrm{Fe}_{207}} M_{\mathrm{Fe}_{207}}}{M_{\mathrm{Fe}_{208}} - M_{\mathrm{Fe}_{207}}} P \sim 2\cdot 10^{-5}\,\mathrm{J/mol} \tag{3.1}$$

We assume that the order of magnitude of this derivative is going to be the same

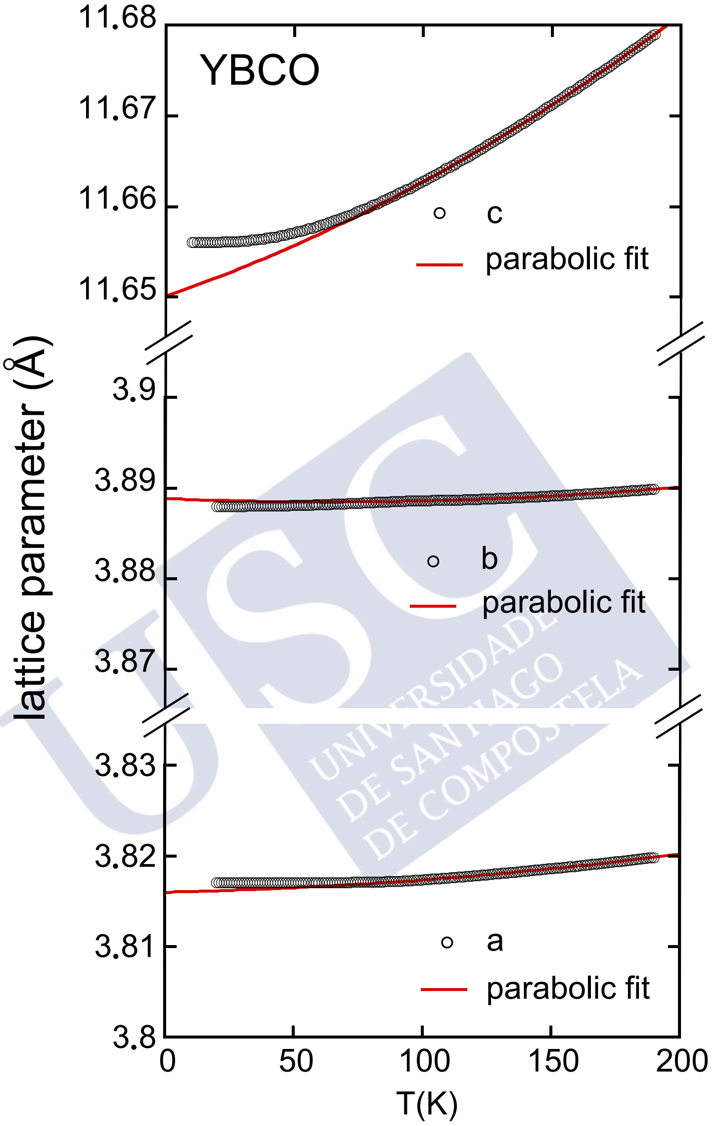

Figure 3.1: Evolution of the 3 lattice parameters of the optimally doped HTS YBCO with temperature obtained integrating the data from Reference [79]. The red lines are the parabolic fits to the data corresponding to the normal state $T > 94\,\mathrm{K}$. We use these data and the parabolic fits to estimate the amount ΔV. Note that all data are plotted within the same scale.

for each element in cuprates. Moreover, if we take into account the difference between the normal and superconducting states of these quantities Δ, the difference should be even lower than the number estimated in the Equation 3.1. If we compare this with the typical order of magnitude of the condensation energy, we realize that we can discard the terms $M_k P(\partial\Delta V/\partial M_k)_{T,P}$ in the first and second extended-Chester equations.

The next term that we are going to estimate is $P\Delta V$, the one that corresponds to the term $P\partial G/\partial P$ of the original Chester equations. Chester himself in his pioneering work [9] remarks that this term is of the order of 10^{-6} cal/mol in BCS superconductors while the condensation energy is of the order of 10^{-3} cal/mol, so it can be discarded. Our strategy here is to obtain an upper limit for this value in cuprates. For that purpose, we are going to use the data of Pasler et al. [79], where they measure the thermal expansion coefficients $\alpha_i = (1/L_i)dL_i/dT$ for each lattice parameter L_i in the YBCO HTS. We are going to obtain the $L_i = a$, b and c lattice parameters of YBCO depending on temperature T by integrating the thermal expansion coefficients as follows:

$$L_i(T) = L_{\mathrm{ref}} \exp\left(\int_{T_{\mathrm{ref}}}^{T} \alpha_i(T)dT\right), \tag{3.2}$$

where L_{ref} and T_{ref} are the reference lattice parameter and the reference temperature. In this case we have chosen for our approximation the temperature $T_{\mathrm{ref}} = 190\,\mathrm{K}$ and the lattice parameters for that temperature $a = 3.82\,\text{Å}$, $b = 3.89\,\text{Å}$, and $c = 11.68\,\text{Å}$, that are the approximated values at room temperature. Note that we are going to calculate differences of products of these parameters, so to obtain the order of magnitude that we are trying to achieve it does not matter if we choose as a starting point an approximate value of the exact lattice parameter at that temperature.

With this approximation we have plotted in Figure 3.1 the evolution of the three lattice parameters of optimally doped YBCO with temperature, in the same scale, extracted from the data of Reference [79].

Reviewing the literature, one can find that the evolution of lattice parameters of both superconductors [79, 82] and non superconducting [80, 81] materials has the same shape, and can be described fitting the data to a second-order polynomial. In first approximation we have fitted the normal state of the lattice parameters to this kind of function to obtain a possible value of the lattice parameters in the normal state at 0 K (named as a_n, b_n and c_n). Due to the fact that the higher α_i value is the one related to the c lattice parameter, this is the one that have a bigger change with temperature, as we can see in the upper part of the Figure 3.1. We have calculated the volume difference $a_n b_n c_n - abc$, to get a possible order of magnitude of the amount ΔV. With those values, we have obtained:

$$P\Delta V \approx -0.0055\,\mathrm{J/mol}, \tag{3.3}$$

where $P = 10^5\,\mathrm{Pa}$ is the atmospheric pressure. This is a value 3 orders of magnitude lower than the typical value obtained for the condensation energy in cuprates. [24–26, 64, 65]

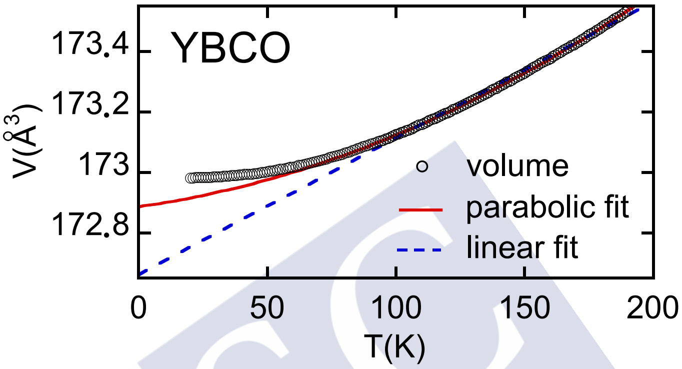

Figure 3.2: Product of the lattice parameters obtained integrating the data from Reference [79] are plotted versus the temperature. The red line represents the parabolic fit to normal state volume $T > 94\,\mathrm{K}$ and the blue dashed line represents the linear fit to the normal state volume. We obtain an estimation of the value of ΔV with this extrapolations to $0\,\mathrm{K}$.

We have used another approach to get the maximum order of magnitude of the volume change that is possible to extract from this data. In this case, we have obtained firstly the volume as a function of the temperature, as is pictured in Figure 3.2, and then we have done another fit to a parabolic polynomial to extract the value of the volume in the normal V_n state at $0\,\mathrm{K}$. With this approach the difference $P\Delta V \approx -0.0057\,\mathrm{J/mol}$, very near from the last estimate. However, we would like also to estimate the highest possible change in volume from the normal to the superconducting state from these data. To do that we have plotted the extreme case in which the normal state fits a linear behavior, being the quantity ΔV the highest. In this case we have obtained a value $P\Delta V \approx -0.0193\,\mathrm{J/mol}$, which is still at least two orders of magnitude lower than the typical value for the condensation energy in cuprates.

Note that we have studied the extreme cases to get the maximum order of magnitude to demonstrate that we can discard this term from our equations. A realistic analysis should discard the volume change from normal to superconducting state in the c direction, because there is no evidence of change in the behavior of this lattice parameter with temperature. On the other hand, it is possible to see directly some jumps of opposite sign in the behavior of lattice parameters a and b in the critical temperature, that leads to a change of volume at least one order of magnitude lower than the one that we have obtained in our lasts approaches.[1] [79]

• Extended-Chester equations without terms estimated negligible in cuprates

Now that we have discarded the term associated to the derivative of the volume respect to the isotopic mass, and the term related to the external forces in the virial theorem we can rewrite the extended Chester Equations for HTS like:

$$\Delta\overline{K}_{\mathrm{M}} = -\sum_{k}^{N_z} M_{\mathrm{k}} \left(\frac{\partial E_{\mathrm{cond}}}{\partial M_{\mathrm{k}}}\right)_{T,P}, \tag{3.4}$$

$$\Delta\overline{K}_{\mathrm{M}} = -E_{\mathrm{cond}} + \sum_{k}^{N_z} M_{\mathrm{k}} \left(\frac{\partial E_{\mathrm{cond}}}{\partial M_{\mathrm{k}}}\right)_{T,P}, \tag{3.5}$$

$$\Delta\overline{\Phi} = 2E_{\mathrm{cond}}. \tag{3.6}$$

There is some direct information that we can infer from these equations. First of all, there is a Coulomb energy saving through all the phase diagram that is always twice the condensation energy E_{cond}. This is a well known result that is in agreement with more specific scenarios, like the MIR proposed by A.J. Leggett. [10–12]

It is also important to remark that, although the Hamiltonian introduced by A.J. Leggett is quite general, it is not the exact Hamiltonian that should be used to describe the exact HTS. For instance, it does not take into account the kinetic energy of the nucleus in the system, that give us information about the role of the phonons in the superconducting mechanism of these materials. The Hamiltonian that we are using is more general, and it let us to obtain information about the role of the phonons in the superconducting mechanism of non conventional superconductors.

---

[1] We also want to remark that if the quantity ΔV does not change very much with pressure, all the energy balances can change with the right order of magnitude in hydrostatic pressure, introducing new phenomenology that may be of interest for HTS such as H_2S.

3.3 Singularizing the oxygen-nucleus contributions $\Delta\overline{K}_{\mathrm{M_O}}$

For continuing our evaluation of the extended-Chester equations in cuprates, the ideal situation would be to count on the experimental measurements of the quantities $M_{\mathrm{k}}(\partial E_{\mathrm{cond}}/\partial M_{\mathrm{k}})_{T,P}$ (see Equations 3.4 to 3.6). However, to the best of our knowledge, there are no measurements of the specific heat with temperature for cuprates with different isotopes. This fact lead us to make some assumptions to try to obtain this derivative. We are going to suppose that the condensation energy depends on the isotopic mass of the element k through different intermediate variables, $U(M_{\mathrm{k}}) = U(A(M_{\mathrm{k}}), B(M_{\mathrm{k}}), ...)$, where A, B, etc., are intermediate properties that depend on the isotopic mass. In this context, we can write that:

$$\left(\frac{\partial E_{\mathrm{cond}}}{\partial M_{\mathrm{k}}}\right)_{T,P} = \left(\frac{\partial E_{\mathrm{cond}}}{\partial A}\right)_{T,P}\left(\frac{\partial A}{\partial M_{\mathrm{k}}}\right)_{T,P} + \left(\frac{\partial E_{\mathrm{cond}}}{\partial B}\right)_{T,P}\left(\frac{\partial B}{\partial M_{\mathrm{k}}}\right)_{T,P} + ... \tag{3.7}$$

The problem now is identifying what those intermediate variables could be. For instance, in the BCS analysis, Chester [9] used the critical magnetic field as an intermediate variable to obtain all the derivatives, taking into account that $H_c = H_0 h(t)$, where $t = T/T_c$ is the reduced temperature, and h is an unknown function. Knowing the derivatives $\partial H_0/\partial M$ and $\partial T_c/\partial M$ it was possible to obtain the energy balances with temperature.

Our problem is more complicated, because we do not know the general equation for the condensation energy through all the phase diagram of the cuprates. Here, we could assume that the two major candidates for these intermediate variables are the critical temperature T_c and the pseudogap energy E_g. There are several experimental data that correlates the evolution of E_{cond}, T_c, and E_g through the phase diagram of some cuprates. [24, 25, 64, 65]

However, as we have mentioned before, to obtain the condensation energy we have to know what is the value of the entropy or the specific heat of the sample in the normal state at temperatures below the critical temperature. To obtain these quantities, in principle three options would be: calculating it through some theory or model, using a high magnetic field to kill the superconducting state, or extrapolating it by taking into account the behavior at higher temperatures. The first option is only useful if we already know the microscopic mechanism that takes place in HTS. The second option is impossible to reach because the upper critical magnetic fields are too high for today's experimental resources. Nevertheless, there have been attempts to introduce magnetic dopants like Zn to suppress the superconductivity and get the value in the normal state. [64] This method could be rather informative, but nowadays it is believed that the normal state of HTS is a competing phase between different states, and even a small amount of dopants can influence this competition, changing the normal state entropy. [63]

Last option is the most used, but it has the problem of whether it is necessary to take into account the pseudogap region as a normal state region, or take only the region above it. D. van der Marel et al. have proposed some generic constraints for the functional behavior of the normal state entropy based only in general thermodynamic principles. [63] For example, one of them is that the normal state entropy at 0 K should be equal to the measured one at that temperature. J.W. Loram et al. [64] have tried to extrapolate the normal state entropy above the pseudogap temperature in underdoped cuprates and they found that this extrapolation does not accomplish some of these constraints. Conversely, extrapolating the entropy associated to the pseudogap regime, it is possible to fulfill all the constraints, and thus obtain an unambiguous value of the condensation energy. Moreover, this extrapolation fits also with the magnetic dopant method. [64] Therefore, we can assume that the pseudogap is a normal state property, and thus it does not take part directly in the calculation of E_{cond}, because above the superconducting fluctuation regime, in the pseudogap region, $S_n(T) = S(T)$.

Conversely, it is clear that E_{cond} depends highly on the T_c value, as we can see directly from the specific heat measurements. [24, 25, 64, 65] In fact, BCS compounds verify that $E_{\mathrm{cond}} \propto T_c^2$.

Therefore, to estimate the energy balances, we are going to assume that the highest dependence of the condensation energy on the isotope masses is through the critical temperature T_c. Note that this approximation have been assumed in the past by A.J. Leggett for a similar estimation. [2]

Within this scenario, it is reasonable to make the following approximation:

$$\Delta\overline{K}_{\mathrm{M_k}} = -M_{\mathrm{k}} \left(\frac{\partial E_{\mathrm{cond}}}{\partial M_{\mathrm{k}}} \right)_{T,P} \approx -M_{\mathrm{k}} \frac{\delta E_{\mathrm{cond}}}{\delta T_c} \frac{\delta Tc}{\delta M_{\mathrm{k}}} = \frac{\delta E_{\mathrm{cond}}}{\delta T_c} \alpha_{\mathrm{k}} T_c, \tag{3.8}$$

where $\alpha_{\mathrm{k}} = -(d \ln T_c / d \ln M_{\mathrm{k}})$ is the isotope coefficient that corresponds to the element k, and δ means the difference of the value between two dopings. Within this approximation, knowing the phenomenology of the phase diagram of cuprates in relation to the critical temperature, the isotope coefficient, and the condensation energy, we can extract some qualitative results for the value of $\Delta\overline{K}_{\mathrm{M_k}}$.

The most measured isotope coefficient in all the phase diagram of cuprates is the isotope exponent for the oxygen α_{O}. [27, 28, 67, 68, 70–75]Therefore, we can calculate the value of $\Delta\overline{K}_{\mathrm{M_O}}$ for the whole phase diagram.

On the other hand, there are some experiments where they study the effect of the copper isotope mass, [69, 75–77] and some measurements for the isotope coefficient for Ba in $\mathrm{YBa_2Cu_3O_{7-\delta}}$ (YBCO) at optimal doping (with an almost negligible effect). [69] For the copper coefficient of LSCO, there are measurements in two points of the phase diagram ($p = 0.15$ and $p = 0.125$), so there is not enough data use them for our calculations. [68, 71, 75] However, these data reflect the same trend for Cu than for oxygen (positive coefficient, and enhanced values for the underdoped region, concretely in the region where $p = 1/8$). For the copper coefficient of YBCO, there are data measured by J.P. Frank et al. [77] for a wide part of the phase diagram. But these data contrast with those obtained by other authors [69, 75] where the copper isotope coefficient shows the opposite sign, with a behavior similar to the case of LSCO (making these data more reliable). Therefore, while there is not enough amount of data to obtain accurately the $\Delta\overline{K}_{M_{\mathrm{Cu}}}$ through all the phase diagram with precision, with the data available we can induce that the trend is similar than for the case of oxygen. The measurement of the other isotope effects for the other elements would rise the opportunity to estimate the behavior of $\Delta\overline{K}_{\mathrm{M_k}}$.

Due to the fact that we are only able to reliably obtain the kinetic energy difference of the oxygen nucleus, we can rewrite the extended Chester equations 3.4 to 3.6 taking into account this fact and the new approximations, as follows:

$$\Delta\overline{K}_{\mathrm{M_O}} \approx \frac{\delta E_{\mathrm{cond}}}{\delta T_c}\alpha_{\mathrm{O}} T_c, \tag{3.9}$$

$$\Delta\overline{K}_{\mathrm{mix}} = \Delta\overline{K}_{\mathrm{M}} + \Delta\overline{K}_{\mathrm{rest}} = -E_{\mathrm{cond}} - \Delta\overline{K}_{\mathrm{M_O}} \tag{3.10}$$

$$\Delta\overline{\Phi} = 2E_{\mathrm{cond}}, \tag{3.11}$$

where $\Delta\overline{K}_{\mathrm{rest}}$ is the sum of the kinetic energy differences between the normal and superconducting state of the nucleus of the cuprate except the oxygen and $\Delta\overline{K}_{\mathrm{mix}}$ is defined as the sum of $\Delta\overline{K}_{\mathrm{M}}$ and $\Delta\overline{K}_{\mathrm{rest}}$. With these equations we will be able to estimate the value of the three energy differences for the cuprates LSCO, Bi2212, and YCBCO through the phase diagram with the available experimental data.

3.3.1 Three regions in the E_{cond} vs doping, $E_{\mathrm{cond}}(p)$, and O-isotope coefficient vs doping, $\alpha_{\mathrm{O}}(p)$, phase diagrams of cuprate HTS

First of all, it is remarkable that the isotope coefficient for oxygen has a similar behavior in the phase diagram for most cuprates. [27] The only remarkable difference in this trend is in the point $p \sim 1/8$ in LSCO, where there is a large jump in the isotope coefficient. [28, 71, 72, 75] The rest of the cuprates verify that the isotope coefficient is always positive, ~ 0 at optimal doping and it increases at both sides of the phase diagram, achieving values up to 0.8 in the underdoped side, and up to ~ 0.1 in the overdoped side. [27, 28, 67, 69, 70, 73, 74, 76]

The phenomenology of the condensation energy and the critical temperature phase diagrams are described in Figure 3.3. The condensation energy general trend is that it increases continuously from small dopings until some point $p \sim 0.19$, where it peaks, and then it starts to fall until maximum doping. [24–26,63–65] Conversely, the T_c phase diagram show for all the cuprates a superconducting dome that follows an approximate inverse parabol that peaks at $p \sim 0.16$. [24–26,63–65]

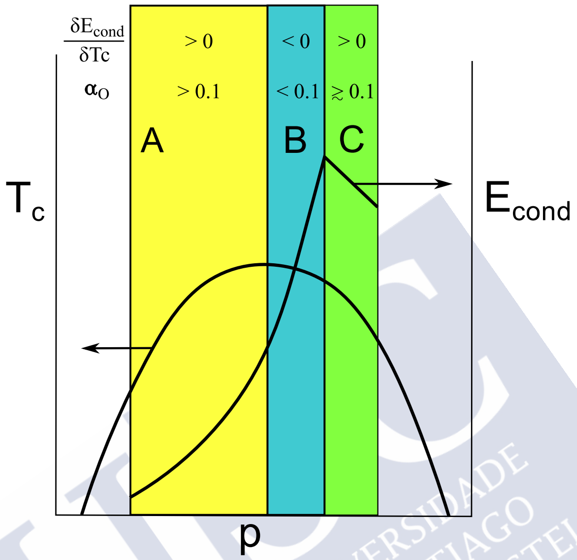

Figure 3.3: Scheme of the qualitative behavior of the critical temperature T_c and the condensation energy E_{cond} through the phase diagram in cuprate superconductors. Within the scenario where most part of the dependence of E_{cond} with the isotope masses of the material is through the critical temperature, we distinguish three regimes A, B and C. These regimes are characterized by a specific sign of the derivative of E_{cond} respect to the T_c, and for different values of the isotope coefficient α.

Due to the fact that the condensation energy and the oxygen isotope coefficient have the same qualitative behavior through the phase diagram of all the cuprates, we can infer some qualitative information about the sign of the kinetic energy variation of the oxygen nucleus through the phase diagram of these materials. Due to the fact that α_{O} and T_c are always positive in cuprates, the sign of $\Delta\overline{K}_{\text{M}_{\text{O}}}$ is going to be given by the quantity $\delta E_{\text{cond}}/\delta T_c$. In this context we distinguish in Figure 3.3 three regimes.

In regime A, both δE_{cond} and δT_c have the same sign, so we expect that in this region $\Delta\overline{K}_{\text{M}_{\text{O}}} > 0$. Then, when we reach the maximum of the dome, we achieve a point in which $\delta T_c \to 0$. This would lead us to a divergence of the quantity

$\Delta\overline{K}_{\mathrm{M_O}}$. However, we have to remark that at this point, $\alpha_{\mathrm{O}} \sim 0$ for all HTS, so we have an indetermination that is going to make hard to get what are exactly the value of $\Delta\overline{K}_{\mathrm{M_O}}$ at this point. However, in region B we have that δE_{cond} and δT_c have opposite sign, so $\Delta\overline{K}_{\mathrm{M_O}} < 0$ here. Therefore, we have uncertainties to know what happens exactly in the maximum of the superconducting dome, but we can ensure that $\Delta\overline{K}_{\mathrm{M_O}}$ changes its sign. Finally, in the boundary between regions B and C the condensation energy peaks, and thus at some point $\delta E_{\mathrm{cond}} \to 0$. This means that $\Delta\overline{K}_{\mathrm{M_O}} = 0$ in that boundary. Finally, in the C region, we reach again the same behavior where $\Delta\overline{K}_{\mathrm{M_O}} > 0$ because δE_{cond} and δT_c have again the same sign.

Note that with this qualitative analysis we can infer the evolution of the sign of $\Delta\overline{K}_{\mathrm{M_O}}$ through the phase diagram, but not its relative value respect to the condensation energy, an important information to know to what extent the movement of the oxygen nucleus play a role in the superconducting mechanism of HTS. This feature will be obtained by our calculations from experimental data that we have collected from the bibliography to plot the energy balances through all the phase diagram of some generic HTS.

3.4 Quantitative analysis of $\Delta\overline{K}_{\mathrm{M_O}}$ in each of the regions of the phase diagram of cuprates

In this subsection we will obtain our most important result from our estimates of the energy balances in cuprate HTS, that reveal three different regions in the phase diagram versus doping level in these compounds (roughly corresponding to regions A-C in Figure 3.3) in which $\Delta\overline{K}_{\mathrm{M_O}}$ favours, opposes or is negligible for superconductivity (roughly $\Delta\overline{K}_{\mathrm{M_O}} > 0$ in A, $\Delta\overline{K}_{\mathrm{M_O}} < 0$ in B, and $\Delta\overline{K}_{\mathrm{M_O}} \sim 0$ in C).

First of all, there are measurements of the condensation energy phase diagram and critical temperature phase diagram for the superconductors LSCO, [26] Bi2212, [25, 64] and YCBCO. [24, 65] We have also found data for the isotopic coefficient of LSCO [28,68,71,72,75] and Bi2212 [27,28,67,73]. We also found one point in the phase diagram for the YCBCO isotope coefficient, [27] so we decided to use the isotope coefficients of generic YBCO, [27, 28, 67, 69–71, 74, 76] taking into account that the trend of the function of the isotope exponent through all the phase diagram is similar for all the cuprates. [27]

With all these data, we have approximated the value of $\Delta\overline{K}_{\mathrm{M_O}}$ evaluated in the mean point $(p_1+p_2)/2$ of each pair of the E_{cond} data obtained experimentally by:

$$\Delta\overline{K}_{\mathrm{M_O}}\left(p{=}\tfrac{p_2+p_1}{2}\right) \approx \frac{E_{\mathrm{cond}}(p{=}p_2) - E_{\mathrm{cond}}(p{=}p_1)}{T_c(p{=}p_2) - T_c(p{=}p_1)}\alpha_{\mathrm{O}}\left(p{=}\tfrac{p_2+p_1}{2}\right) T_c\left(p{=}\tfrac{p_2+p_1}{2}\right), \quad (3.12)$$

where p_2 and p_1 are the dopings where the E_{cond} have been measured. The values of E_{cond}, the isotope coefficient and the critical temperature at these dopings have been interpolated from the data of the references [24–28]. We have plotted in Figure 3.4 the adimensional fraction of $\Delta\overline{K}_{\mathrm{M_O}}/E_{\mathrm{cond}}$ for the phase diagram of the three cuprates.

This is an important amount, that tells us to what extent the phonons play a role in the mechanism of HTS in different parts of the phase diagram.

3.4.1 Region A of the phase diagram: $\Delta\overline{K}_{\mathrm{M_O}}$ favors superconductivity

The Figure 3.4 shows clearly the three regimes described in Section 3.3. In the region A, there is a kinetic energy saving in the oxygen kinetic energy, that near optimal doping is not negligible, *i.e.*, the quantity $\Delta\overline{K}_{\mathrm{M_O}}/E_{\mathrm{cond}}$ is in the order of the unity. This means that in this region of the phase diagram, the movement of the oxygen nucleus favors superconductivity, with a non negligible contribution to the condensation energy.

This is due in part to the fact that in this region of the phase diagram, the isotope coefficient α_{O} reaches very high values, and the value of the condensation energy derivative respect to the critical temperature is also high. It is also remarkable that in this region, the behavior of $\Delta\overline{K}_{\mathrm{M_O}}/E_{\mathrm{cond}}$ in LSCO is quite different, because the kinetic energy difference increases at low dopings. This is due to the fact that in this region this compound has a very different isotope coefficient, extremely high ($\alpha_{\mathrm{O}} \approx 0.8$). Moreover, LSCO has a quite different phase diagram in the region around $p \approx 1/8$, which also contributes to enhance this value. The other two compounds show a different behavior, showing a lower value for lower dopings and the highest values near the optimal doping.

3.4.2 Indeterminate crossover between regions A and B

As we discussed in Section 3.4, between the region A and B we have an indeterminate region due to the fact that there the value of $\delta T_c \approx 0$ and the value of the isotope coefficient is also negligible. This leads to an indetermination, that can only be solved measuring directly the isotope effect in the condensation energy at optimal doping. However, due to the universal shape of the phase diagram of the cuprates, we can ensure that the sign of the kinetic energy change of the oxygen nucleus is different at both sides of the optimal doping.

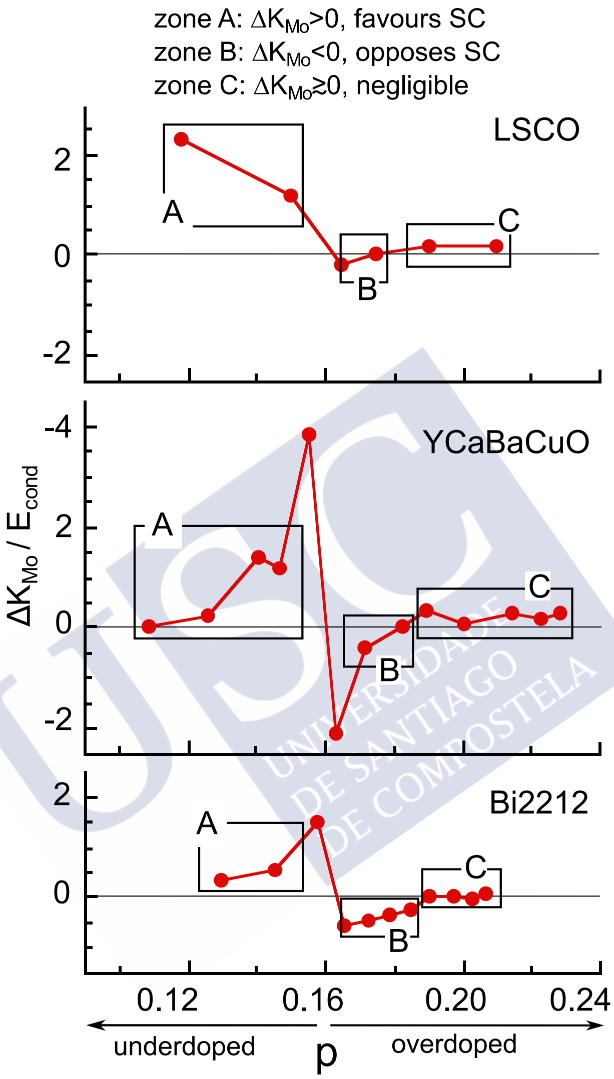

Figure 3.4: Fraction of the kinetic energy variation of the oxygen nucleus in relation to the condensation energy in the phase diagram for three different cuprates obtained by Equation 3.12. In the upper part of the Figure is represented the calculations for LSCO, in the lower part the calculations for YCBCO are plotted, and in the lower part the calculations for Bi2212 are presented. We distinguish three different regions (A,B and C) common to all the cuprates.

3.4.3 Region B of the phase diagram: $\Delta\overline{K}_{\mathrm{M_O}}$ opposes superconductivity

This lead us to define the region B, where the amount $\Delta\overline{K}_{\mathrm{M_O}}/E_{\mathrm{cond}}$ is negative and non negligible, showing us that in this region of the phase diagram, the movement of the oxygen nucleus opposes superconductivity. This non-negligible value comes from the fact that in this region of slight overdoping, the value of δT_c is lower in comparison to the value of δU leading to a high negative value of this derivative.

3.4.4 Region C of the phase diagram: $\Delta\overline{K}_{\mathrm{M_O}}$ almost negligible

Finally, in the region C we find that the kinetic energy change is also positive, like in region A, but with a negligible value, which means that in this part of the phase diagram the change in the movement of the oxygen nucleus does not affect remarkably to the superconducting state.

3.5 Quantitative analysis of the rest of energy terms in the extended Chester equations for cuprates

Once we have obtained $\Delta\overline{K}_{\mathrm{M_O}}$, it is possible to apply the full set of extended-Chester equations to obtain the rest of energy balance terms. We jointly plot E_{cond}, $\Delta\overline{\Phi}$, $\Delta\overline{K}_{\mathrm{mix}}$ and $\Delta\overline{K}_{\mathrm{M_O}}$ values, as a function of the doping level, for the three prototypical HTS considered in this work (LSCO in Figure 3.5, Bi2212 in Figure 3.5, and YCBCO in Figure 3.7).

In these Figures we can verify, first of all, two conclusions already mentioned in Sections 3.3 and 3.4: *i)* that there is a Coulomb energy saving in the whole phase diagram that is exactly twice the condensation energy for all dopings and *ii)* the evolution of the Kinetic energy difference of the oxygen nucleus through the phase diagram. These three figures also let us to observe the evolution of the quantity $\Delta\overline{K}_{\mathrm{mix}}$ (the sum of kinetic energies of the rest of the ions and the electrons of the system).

An additional noteworthy feature that can be discussed in view of the results in these Figures is whether the region $p \gtrsim 0.19$ (corresponding to region C in the previous Section and its Figure 3.3) presents, or not, BCS-like behavior for its energy balances. note that many authors claim that this region is characterized by BCS-like behavior due to the fact that fthere $E_{\mathrm{cond}} \propto T_c^2$. However, according to our extended-Chester results the total kinetic energy saving in the nucleus of the system should be equal to the value of the condensation energy. Here, what we find in our calculations is, at least, that the contribution of the movement of the oxygen nucleus to the condensation energy is almost negligible in this region. This fact should be balanced with the contributions of the other ions to reach a BCS behavior. However, the trend of the experimental data available indicates that the contribution of the copper nucleus is within the same order of magnitude that for the case of oxygen (because the condensation energy derivatives respect to T_c are the same, and the isotope coefficient that has been measured shows the same trend), and that the contribution of the other nucleus is almost negligible.

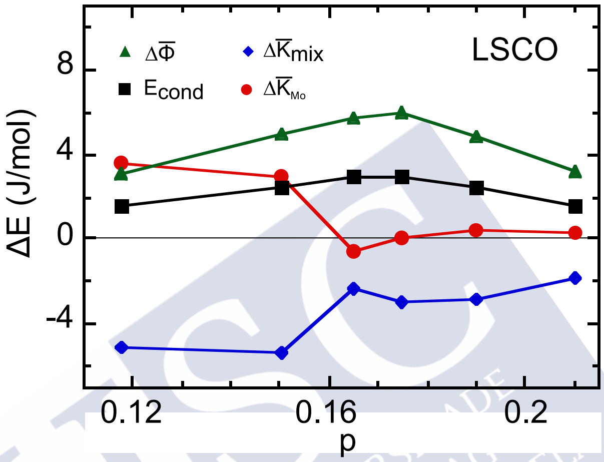

Figure 3.5: Energy balances of the cuprate superconductor LSCO through the phase diagram. The data of the condensation energy $E_{\rm cond}$ represented by the black squares is taken from Reference [26]. The Coulomb energy saving $\Delta\overline{\Phi}$ represented by the green triangles is obtained using Equation 3.6. The energy balance of the kinetic energy of the Oxygen nucleus represented by the red circles is obtained by Equation 3.12. The sum of the energy balance of the kinetic energy of the electrons and the kinetic energy of the rest of the ions $\Delta\overline{K}_{\rm mix}$, represented by the blue diamonds, is obtained from Equation 3.5.

Therefore, our present results signal that region C of the phase diagram ($p \gtrsim 0.19$) has significant deviations from the BCS energetics in spite of the $E_{\rm cond} \propto T_c^2$ relation.

Finally, for this section, it may be interesting to ask ourselves about the kinetic energy savings for electrons, $\Delta\overline{K}_e$, even if we will need to introduce surely less established assumptions in the discussion (so that, therefore, our conclusions will be more tentative ones). First of all, we note that the kinetic energy differences $\Delta\overline{K}$ may be considered essentially null for all the nucleus except for Cu and O (as the corresponding isotope effects are essentially negligible). Secondly, for the kinetic term associated to the Cu nucleus we may, somewhat naïvely perhaps, try

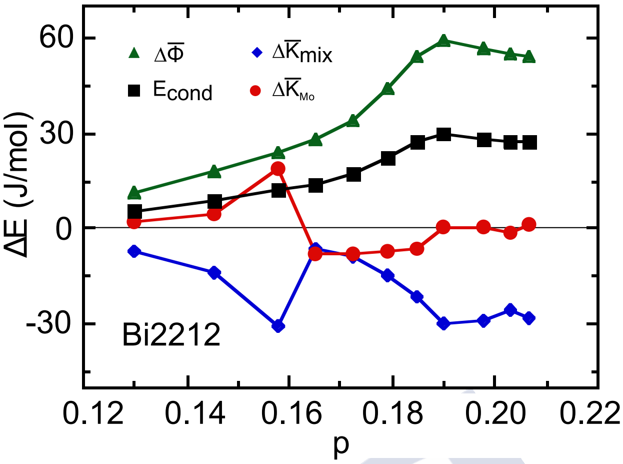

Figure 3.6: Energy balances of the cuprate superconductor Bi2212 through the phase diagram. The data of the condensation energy E_{cond} represented by the black squares is taken from Reference [25]. The Coulomb energy saving $\Delta\Phi$ represented by the green triangles is obtained using Equation 3.6. The energy balance of the kinetic energy of the oxygen nucleus represented by the red circles is obtained by Equation 3.12. The sum of the energy balance of the kinetic energy of the electrons and the kinetic energy of the rest of the nucleus $\Delta\overline{K}_{\mathrm{mix}}$, represented by the blue diamonds, is obtained from Equation 3.5.

$\Delta\overline{K}_{\mathrm{M_{Cu}}} \approx \Delta\overline{K}_{\mathrm{M_O}}$ (as the isotope effects α_{Cu} and α_{O} are similar to each other).

Therefore, we could estimate with these ansatzs that:

$$\Delta\overline{K}_e \approx -E_{\mathrm{cond}} - 2\Delta\overline{K}_{\mathrm{M_O}}. \tag{3.13}$$

This equation would indicate, then, that the electrons increase their kinetic energy in the superconducting transition, and this increase is lowered in the region B, where the kinetic energy of the ions is also negative.

These reasonings and data comparisons suggest, therefore, a change in both the amplitude and the sign of $\Delta\overline{K}_e$ as we more across the different regions, A, B, C of doping in Figure 3.3.

3.6 Conclusions

With the help of the available data and an approach based in the fact that the condensation energy depends on the isotopic mass through the critical temperature, we have estimated what are the value of $\Delta\overline{K}_{\mathrm{M_O}}$, $\Delta\overline{\Phi}$ and $\Delta\overline{K}_{\mathrm{mix}}$ using the experimental data available in cuprate HTS.

Our main result is the existence of three different regimes for the evolution of $\Delta\overline{K}_{\mathrm{M_O}}$ in the cuprates. We have demonstrated that the role of the phonons in the superconducting mechanism of the cuprates is doping dependent. This is an important consequence that is neglected in the MIR scenario, that is also based on first principles. [10–12]

In the region A, defined as the underdoped side of the phase diagram, we have found that there is a saving in the kinetic energy of the oxygen nucleus, which is of the order of the condensation energy specially near the optimal doping. At small dopings we have found a decrease of this energy difference except in LSCO, which presents a different behavior for the $\alpha_{\mathrm{O}}(p)$ coefficient, and a different trend in the $T_c(p)$ phase diagram in the surroundings of $p \sim 1/8$.

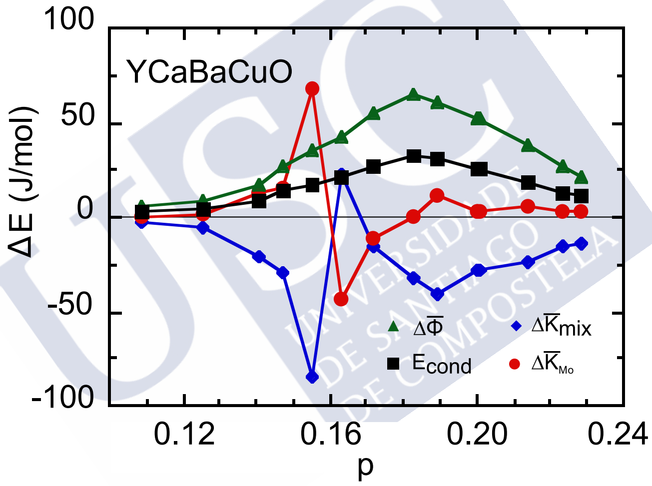

Figure 3.7: Energy balances of the cuprate superconductor YCBCO through the phase diagram. The data of the condensation energy E_{cond} represented by the black squares is taken from Reference [24]. The Coulomb energy saving $\Delta\overline{\Phi}$ represented by the green triangles is obtained using Equation 3.6. The energy balance of the kinetic energy of the Oxygen nucleus represented by the red circles is obtained by Equation 3.12. The sum of the energy balance of the kinetic energy of the electrons and the kinetic energy of the rest of the nucleus $\Delta\overline{K}_{\mathrm{mix}}$, represented by the blue diamonds, is obtained from Equation 3.5.

In the region B, that corresponds to the slightly overdoped region, $\Delta\overline{K}_{\mathrm{M_O}}$ becomes negative and comparable to the amount of E_{cond}, a feature that contrasts with the BCS behavior, where the kinetic energy of the ions is reduced through the superconducting transition

There is an indetermination to obtain both $\Delta\overline{K}_{\mathrm{M_O}}$ and $\Delta\overline{K}_{\mathrm{mix}}$ around the optimal doping, due to the fact that $\delta T_c \approx 0$ and $\alpha_{\mathrm{O}} \approx 0$. However, due to the functional behavior of $T_c(p)$ and $\alpha(p)$, we can ensure that there is a change of sign in that region that remarks a change of tendency in the energy balances, defining an indeterminate crossover region. We also point out that in the surroundings of the optimal doping, the value of $\Delta\overline{K}_{\mathrm{M_O}}$ has the same order of magnitude than the value of E_{cond}. One could argue that those values are not precise due to the indetermination at optimal doping, but in some compounds that behavior is extended to a wide region, indicating that is the right trend.

In the region C, that corresponds to the high overdoped side of the phase diagram, this amount is almost negligible, and we can infer that here the movement of the oxygen nucleus does not play an important role in the superconductivity.

The above conclusions overall suggest that the movement of the oxygen nucleus play a non negligible role in superconductivity in some regions of the phase diagram of cuprates. In fact, in one region (B) they increase their kinetic energy when they reach the superconducting state, and in other regions (A,C) they decrease their energy, as it happens in the BCS compounds. The experimental data available indicates that the kinetic energy of copper nucleus could play a similar role in the energy balances.

Moreover, it is important to remark that until now, small isotope coefficients near the optimal doping seemed to remark that the role of the phonons in superconductivity was not important. Our results suggest that the change in the movement of the nucleus change from the normal to the superconducting state is different at both sides of the superconducting dome. They also suggest that the change in the movement of the nucleus at the edges of the superconducting dome is almost negligible, in contrast to the fact that in that regime the isotope coefficients are higher.

II: Some applied researches of micro- and nano-structured superconductors and other materials


USC
UNIVERSIDADE
DE SANTIAGO
DE COMPOSTELA

IIA: SUPERCONDUCTING DEVICES

The contentsin this part are based on our Spain's patent application coded P201930020 and an article by J.C. Verde et al. submitted for publication in Nanomaterials (Chapter 4), and in articles [47,88] and book [89] by J.C. Verde et al. (Chapter 5).


USC
UNIVERSIDADE
DE SANTIAGO
DE COMPOSTELA

Chapter 4

Design optimization of high-temperature superconducting bolometers HTS TES using doping nanostructuration and 1D patterning

Summary of the chapter:

We consider the possibility of improving by means of micro and nanostructuration of the doping level the operational characteristics of cuprate superconductors (HTS) when used as thin film active elements in bolometric radiation-sensor devices (HTS TES). We develop for that task both numerical computations and effective-medium theoretical formulas. The results of both of these two independent methods suggest that doping structuration may significantly improve the operational characteristics of these devices. For instance, the most optimized structuration design found by our analysis (a 1D discrete 4-step patterning of the doping level) with respect to conventional, non-structured HTS TES doubles the sensitivity and improves by more than one order of magnitude the saturation power and operating temperature range.

4.1 Introduction

Bolometers are radiation sensors that detect incident energy via the temperature increase caused by the absorption of incoming photons. Sensors formed by an array of microsized bolometers (microbolometers) are often used, *e.g.*, for infrared cameras, detectors in quantum cryptography, astrophysics, satellites, aviation, etc. [29–34]

A key figure influencing the efficiency of resistive bolometers (that measure variations of temperature T through the corresponding changes of the electrical resistance R) is the so-called "temperature coefficient of resistance" or TCR, given by: [29–34]

$$\mathrm{TCR} = \left| \frac{1}{R} \frac{\mathrm{d}R}{\mathrm{d}T} \right| . \tag{4.1}$$

Highly sensitive bolometers require a large value of TCR. For instance, structures of vanadium oxides $\mathrm{V}_x\mathrm{O}_y$, commonly used in commercial microbolometers, present $\mathrm{TCR} \sim 0.025\,\mathrm{K}^{-1}$. [34]

Much larger TCR may be achieved with superconductors kept at base temperatures coincident with their normal-superconducting transition, T_c. This is the case mainly when using conventional low-temperature superconductors with $T_c \leq 1\mathrm{K}$ (the so-called low-T_c transition edge sensors, or low-T_c TES), that achieve $\mathrm{TCR} \sim 1000\,\mathrm{K}^{-1}$ or even more. [29, 35] Such high values are possible because low-T_c superconductors have a particularly narrow transition, due both to the achievable high purity and to the fact that their critical effects near T_c are negligible and produce almost unobservable rounding of the normal-superconductor transition (also when operated in a voltage-biased configuration). The very high TCR values of low-T_c TES make them a technology of choice for detecting the most faint radiation incidences, as for cosmic microwave background measurements or for other new applications where single-photon detection is important, as in quantum entanglement and cryptography. [29–31] Note that for these applications the very low temperature required to operate the low-T_c TES is often not seen as a major problem, because cryogenizing the sensor below a few Kelvin is required anyway in order to minimize the thermal noise coming from the bolometer itself (that would otherwise mask the faint radiation to be measured).

However, the requirement of a highly-stabilized liquid-helium-based cryogenic setup is a serious difficulty for adoption of low-T_c TES in other applications. For these scenarios, thermal self-noise problems may be avoided already at much higher temperatures, feasible using less problematic coolers (the general rule is to operate the bolometer below the radiant temperature of the source to be measured) [39, 40].

After the discovery of high-T_c cuprate superconductors (HTS), various authors have explored their use for bolometer sensors (the so-called HTS TES) with simpler liquid-nitrogen-based cryogenics. [36–41] The compound $\mathrm{YBa_2Cu_3O_\delta}$ (YBCO) is the HTS usually considered for this application, usually with optimal nominal doping. As shown in [36–41], $YBa_2Cu_3O_{7-\delta}$ thin films provide in some aspects a viable competition to V_xO_y. These $YBa_2Cu_3O_{7-\delta}$ films not only provide TCR $\sim 1.5\,K^{-1}$ and low noise at an operational temperature $\sim 90\,K$, but also a faster thermal response than V_xO_y. Moreover, the rest of parameters contributing to a large sensitivity (thermal conductivity, infrared absorbance, etc.) are also favorable or at least competitive with semiconducting bolometers. [36–41]

However, the HTS TES until now proposed still share some of the significant shortcomings of low-T_c TES: First, thermal stability of the cryogenic bath is still challenging (liquid-nitrogen systems are simpler but tend to thermally oscillate more than those based on liquid helium). Secondly, both types of TES have useful TCR only at the superconducting transition, corresponding to operational temperature intervals ΔT of just $\sim 0.1\,K$ or less for low-T_c TES, and $\sim 1\,K$ for the HTS TES proposed until now. [36–41] In contrast, $\Delta T \sim 25\,K$ is common for V_xO_y. [34] Importantly, this also means that small quantities of incoming radiation suffice to saturate existing HTS TES, making them appropriate only for "very poorly lit" imaging (low dynamic range).

The HTS TES systems proposed until today use superconductors homogeneous in nominal composition and critical temperature. [36–40] However, in the recent years different novel techniques have been developed to impose regular patterns to HTS thin films, creating custom designs, down to the micro- and the nano-scales. [42–46] This allows custom-engineering regular variations of the critical temperature over the film surface. Realization of these regular and controlled patterning has been experimentally achieved using, *e.g.*, local ferroelectric field-effect, [42] nanodeposition, [43] focused ion beam, [44] etc. In fact, nanostructuring of HTS has become the specific subject of recent conferences [45] and networks [46] funded by the European Union. Most growers of structured HTS films have focused up to now on increasing their critical current and achieving collective vortex pinning at certain matching magnetic fields. [42–45] Also, in a recent work [47] some of us preliminary showed that some simple ad hoc patterns may also moderately modify the shape of the $R(T)$ curves near the transition (*e.g.*, sharpening it).

However, the use of nanostructured films for optimizing HTS TES has been considered only very marginally up to now, the only precedent to our knowledge being Reference [90] by Boktem et al., who consider films with random distributions of nonsuperconducting incrustations producing limited increases of ΔT up to only $\sim 2\,K$ (and also small, and not always favorable, TCR variations).

Our aim in the present work is to propose improvements of HTS TES microbolometers by considering the use of $YBa_2Cu_3O_{7-\delta}$ thin films including doping nanostructuring and doping patterns. In particular, our main objective will be to obtain an increase of the operational temperature interval, ΔT, in which *i)* the TCR is large and *ii)* R is linear with T (*i.e.*, $\mathrm{d}R/\mathrm{d}T$ constant with T, that is another desirable feature that simplifies both the electronic control of the microbolometer and the required stability of the cryogenic setup). Accompanying this ΔT increase we will also obtain notable improvements of other bolometric characteristics, as the saturation energy and power, and in some cases the TCR itself.

To fulfill that objective, we will study the operational characteristics of doping-nanostructured HTS TES . We will consider two major types of structuration: First, the random spatial disorder intrinsically associated to non-optimal doping levels. Secondly, we consider the imposition of regular arrangements of zones with different nominal doping levels each (patterning).

For the first type of structuration (structured non-patterned HTS TES, presented in Sections 4.2 and 8.5), we implement as methods finite-element parallel-superconducting calculations and also, as a way to confirm the results, analytical estimates using an effective-medium approximation (based on Reference [91]). These results are also verified against existing measurements in equivalent YBCO films by other authors [92] (who never implemented them in a HTS TES but measured the $R(T)$ curve in the relevant temperature interval). Our results indicate that simple type of structuration already improves some of the bolometric parameters with respect to this conventional non-structured HTS TES proposed until now (see, *e.g.*, Table 4.1 for a rapid summary).

Concerning the HTS TES structured by means of ad-hoc pattern designs of different zones, with different nominal doping levels (Sections 4.4 to 4.7) we have adapted our methodology to include the possibility of such zones (also extending the corresponding analytical formulae of Reference [92] both to the general case and to each example pattern considered). We will explicitly discuss three specific patterns that we found of special interest, each successively presenting better bolometer performance (see Table 4.1). Our more optimized design is a 4-step discretized exponential-like dependence of nominal doping with the longitudinal position. This pattern design should be the one easier to fabricate among those considered by us, and also the one presenting the most improved bolometric characteristics: with respect to conventional non-structured HTS TES, it improves by more than one order of magnitude ΔT and the saturation measurable power, and it also almost doubles the TCR sensitivity.

4.2 Methods for structured non-patterned HTS TES

A prerequisite for our study is to have a valid description method for superconductors comprised by a single zone of uniform doping. Such single-doping domains will be later the building blocks which associations as a mesh circuit will form the doping-structured HTS film. In this section, we first briefly review the basic equations for the main operational bolometric characteristics of HTS TES sensors, and next we collect, from the existing bibliography, phenomenological formulae describing for non-patterned HTS films the electrical resistance vs temperature curves, $R(T)$, crucial to determine most of such bolometric characteristics.

4.2.1 Main operational parameters for HTS TES sensors

Operation of HTS TES is based on the increase of the electrical resistance R with temperature T as radiation heats the sensor: Therefore, a fundamental feature is the range of temperatures over which the increase of R is large. In particular, we define the operational temperature interval ΔT as the difference

$$\Delta T = T^{+} - T^{-}, \tag{4.2}$$

where T^{-} is the base thermal bath temperature (*i.e.*, the one that occurs in absence of radiation) and T^{+} is the maximum temperature up to which R maintains the strong and constant slope with T. With these definitions, the TCR may be obtained as:

$$\mathrm{TCR} = \frac{R(T^{+}) - R(T^{-})}{\Delta T\ R(T^{-})}. \tag{4.3}$$

Another important operational parameter that follows from the $R(T)$ transition is the saturation energy $E^{\max}$, defined as the maximum energy that the bolometer is able to measure:

$$E^{\max} = C\Delta T, \tag{4.4}$$

where C is the heat capacity of the ensemble formed by the superconducting film and its substrate. Note that the mass of the later is always much larger than the one of the superconducting layer (typical thicknesses are 100 nm for the HTS and 1 mm for the substrate). Thus, C is dominated by the substrate and is essentially independent of the doping of the superconductor. However, the C of the substrate is temperature-dependent. Therefore, the operational temperature T^{-} corresponding to each doping must be taken into account in the calculation of C. The most commonly used substrate for YBCO superconductors is single-crystalline $SrTiO_3$ (STO) and henceforth we will evaluate C using the experimental data of Reference [93] for the heat capacity of STO at cryogenic temperatures.

More important than $E^{\max}$ is often $P^{\max}$, the maximum power that can be measured without saturation:

$$P^{\max} = G\Delta T, \tag{4.5}$$

where G is the thermal conductance between the sensor and the thermal bath. For concreteness, we will consider a microbolometer in which the substrate is directly in contact with the heat sink. Therefore, to evaluate G we use the experimental data of Reference [94] for the thermal conductivity of single-crystalline STO, interpolating them at the operation temperature of each considered superconductor.

We emphasize here that the C and G dependence on T is moderate, with variations below $\sim 20\%$ between 75 K and 90 K. Therefore, for optimizing E^{max} and P^{max} via doping structuring, the main factor to consider will be the corresponding increase of ΔT in Equations (4.4) and (4.5).

Another important parameter to describe the bolometer operation is the time constant τ given by:

$$\tau = C/G. \tag{4.6}$$

This parameter estimates the time necessary for the bolometer to return to the temperature of the sink when the radiation is turned off [95]. Note that this quantity does not depend on the width ΔT, and it is not going to change deeply with doping structuring.

4.2.2 $R(T)$ in the normal state of non-structured HTS

The temperature versus doping, T-vs-p, phase diagram of HTS displays various regions with markedly distinct $R(T)$ behavior. This phase diagram has been, in fact, extensively studied by different authors, and today its account is fairly complete at the quantitative phenomenological level, as recently reviewed in detail, *e.g.*, in Reference [96] (independently of the fact that many of the fundamental microscopic reasons for the occurrence of such phase diagram are still open to considerable controversy at the highest-profile academic forums [97, 98]).

This HTS phase diagram is convenient summarized in the Figure 4 of Reference [96]. Here, for the sake of brevity and clarity, let us just recall that the superconducting critical temperature is maximum at $p \sim 0.155$ (optimal doping, separating the underdoped $p < 0.155$ and overdoped $p > 0.155$ compositions). Above $T_c(p)$, the material presents a normal-state background electrical resistivity, $\rho_{\mathrm{b}}(T, p)$, that is linear on T above a certain so-called pseudogap temperature T^*, and is pseudoparabolic semiconducting-like [96] for $T_c < T < T^*$. In YBCO, it is $T^*(K) \approx 270 - 3000(p - 0.1)$, [96] so that for $p \gtrsim 0.16$, it is $T^* < T_c$ and the semiconducting-like region disappears. Instead of these rapid crude approximations, we will use in our analysis, all through the present work, the detailed quantitative results for $T_c(p)$, $T^*(p)$ and $\rho_{\mathrm{b}}(T, p)$ given in Reference [96] for YBCO.

Near $T_c(p)$, obviously $R(T)$ undergoes the superconducting transition towards $R(T) = 0$. This transition is not fully sharp: instead, a sizable rounding of $R(T)$ occurs in the vicinity of $T_c(p)$. This rounding is known to have two contributions: critical fluctuations and doping inhomogeneities, that we describe in the following subsections.

4.2.3 Rounding of $R(T)$ near the superconducting transition due to critical phenomena

The critical fluctuations around the transition play an important role in HTS and have been studied in detail, *e.g.*, in References [92, 99–103]. The effects of critical fluctuations in the resistance curves are commonly summarized via the so-called paraconductivity, $\Delta\sigma$, defined as the additional contribution to the electrical conductivity due to fluctuations: In particular, the total conductivity $\sigma(T)$ near the transition becomes

$$\sigma = \Delta\sigma + \frac{1}{\rho_{\mathrm{b}}}, \tag{4.7}$$

where ρ_b is the normal-state background resistivity (see the previous subsection). Because $\Delta\sigma$ follows critical-divergence laws near the transition, its effect far from T_c (for $T \gtrsim 1.7\,T_c$) is totally negligible. Closer to T_c, however, $\Delta\sigma$ becomes progressively important and two T ranges may be distinguished. For $1.01T_c \lesssim T \lesssim 1.7T_c$, *i.e.*, the so-called Gaussian fluctuations region, $\Delta\sigma$ is well described by the Lawrence-Doniach paraconductivity equation for layered superconductors: [99, 100, 104]

$$\Delta\sigma = \frac{e^2}{16\hbar d}\left\{\frac{1}{t}\left(1+\frac{B_{\mathrm{LD}}}{t}\right)^{-1/2} - \frac{2}{c} + \frac{t + B_{\mathrm{LD}}/2}{c^2}\right\}, \tag{4.8}$$

where e is the electron charge, $\hbar$ is the reduced Planck constant, $t = \ln(T/T_c)$ is the reduced temperature, $B_{\mathrm{LD}} = (2\xi_c(0)/d)^2$ is the Lawrence-Doniach [104] layering parameter, $\xi_c(0)$ is the Ginzburg-Landau coherence length amplitude in the out-of-plane direction ($\simeq 1.1$ Å in YBCO [99, 100]), d is the superconducting layer periodicity length ($\simeq 5.85$ Å in YBCO [99, 100]) and c is a high-temperature cutoff constant $\simeq 0.7$ in YBCO [99].

Closer to T_c, for $T_{BKT} \lesssim T \lesssim 1.01T_c$ we find the strong phase fluctuation regime, dominated by the Berezinskii-Kosterkitz-Thouless (BKT) transition temperature T_{BKT} ($\sim T_c - 2\,\mathrm{K}$ in YBCO [105]). In this regime the paraconductivity can be obtained using the equation: [102, 106, 107]

$$\Delta\sigma = A_{\mathrm{BKT}}\,\exp\left[4\sqrt{\frac{T_c - T_{BKT}}{T - T_{BKT}}}\,\right], \tag{4.9}$$

where A_{BKT} is a constant, obtainable by requiring continuity of Equations (4.8) and (4.9) at the intersection of the Gaussian and BKT regimes, *i.e.*, at $T = 1.01T_c$.

4.2.4 $R(T)$ transition rounding due to intrinsic structuration of the doping level; Nominal vs. local doping

As it has been explicitly demonstrated in various relatively recent experimental and theoretical works, [101–103,108,109] an additional (and crucial for some doping levels) ingredient to understand the phenomenology of the resistive transition in HTS is to take into account the random T_c-inhomogeneities associated with the intrinsic disorder of the doping level. This intrinsic structuration is due to the fact that HTS compounds are non-stoichiometric, and therefore each dopant ion has at its disposal various lattice positions to occupy. Experimental measurement indicate that a typical size of each local inhomogeneity is about (30 nm)^2 for HTS. [103, 108, 109] This produces, therefore, a certain randomness in the doping at the local scale, unavoidably present in even the more carefully grown HTS samples. A relatively easy geometrical calculation [103,108,109] reveals that this intrinsic structuration shall produce a Gaussian distribution of local dopant levels, as

$$\omega(p,\overline{p}) = \frac{2\sqrt{\ln 2}}{\sqrt{\pi}\Delta\overline{p}} \exp\left[-\left(\frac{p-\overline{p}}{\Delta p/(2\sqrt{\ln 2})}\right)^2\right], \tag{4.10}$$

where $\omega(p,\overline{p})$ is the fraction distribution of local doping levels, p, for a film with average doping level $\overline{p}$ (henceforth called nominal doping), and Δp is the FWHM of the Gaussian distribution. This Δp may be obtained, in turn, on the grounds of coarse-graining averages (see, *e.g.*, Equation (6) of References [103] and [108]) and for YBCO it is $\Delta p \sim 0.006$ (with a small dependence on $\overline{p}$ that may be considered in excellent approximation linear $\Delta p = 0.0032 + 0.0189\overline{p}$). [103, 108]

Due to the $T_c(p)$ dependence in HTS, the above distribution of local p values leads, in turn, to a corresponding distribution of local critical temperatures around the nominal value $\overline{T}_c = T_c(\overline{p})$. The corresponding FWHM for such intrinsic T_c structuration has been also considered, *e.g.*, in [103,108]. Not surprisingly, it becomes quite negligible ($\sim$ 1K in YBCO) for nominal dopings $\overline{p} = 0.155$ (at which $T_c(p)$ is saturated at its maximum value and dT_c/dp is almost zero). However, for non-optimal dopings the situation may become very different and the T_c distribution can reach FWHM values as large as, *e.g.*, $\sim 5\,\mathrm{K}$ for $\overline{p} = 0.13$, significantly influencing the $R(T)$ roundings for non-optimally doped HTS.

4.2.5 Obtainment of the $R(T)$ curve of non-patterned HTS TES using finite-element computations

To calculate the resistance transition curves, $R(T)$, of each microbolometer, we have used software (TOSERIS, available by request to authors) that numerically solves the electrical mesh-current matrix equations of a film modeled as a 200×200

square lattice of monodomains, where each domain i may have its own doping p_i, and thus its own T_{ci} and resistivity curve. We have used Equations (4.7)–(4.9) for the $\rho_i(T,p)$ functionality of each monodomain i. The model also includes a power source and a voltmeter connected with zero-resistance contacts to opposite edges of the sample (see, *e.g.*, scheme in Fig. 4.1) and the $R(T)$ of the film will be obtained as the external V/I. Calculating the circuit requires to numerically invert, for each temperature, the sparse matrix with dimensions 40001×40001 that defines the mesh-current equations. This is a parallelizable computation for which we employed a 31 Tflops supercomputer (LBTS-εpsilon, that comprises about 12000 floating-point units and is described in Reference [89]). It was 100% allocated to run our software during several weeks.

We have performed our calculations with the following numerical values, representative of the HTS compound YBCO: For the area of a finite-element monodomain i we used $(30\,\mathrm{nm})^2$, that is expected to correspond to the size of a doping T_c inhomogeneity. [103, 108, 109] Therefore, the surface of the simulated microbolometer is going to be $(6\,\mu\mathrm{m})^2$ (and a 1-megapixel sensor formed by such microbolometer pixels would occupy $(6\,\mathrm{mm})^2$, a value well within current technological expectations). For the film thickness we use 100 nm, and for the physical parameters entering the critical fluctuation expressions we use the ones described in Subsection 4.2.3.

In the case of non-patterned HTS considered in this section, the only spatial variation of doping and T_c is the unavoidable intrinsic dopant ion structuration and, thus, we assign the local p_i and T_{ci} value to each of our 200×200 monodomains i as follows: We first build a set of 40000 values of dopings following the Gaussian distribution given by Equation (4.10). We then assign each of those p-values to each node i randomly. Finally, those p_i are transformed to T_{ci} values (and corresponding $\rho_i(T)$ functions) following the quantitative results of Reference [96]. An scheme of an example of the resulting spatial distribution is provided in Figure 4.1.

We have tested whether the above procedure could be computationally simplified by using a lighter 10x10 finite-element mesh, as done by us in Reference [102] for other purposes. For non-patterned HTS TES, the results are comparable with those of the 200×200 simulations. However, as commented in Sections 4.4 to 4.7 such small meshes would not be enough to simulate patterned HTS TES. Therefore, for coherence we used 200×200 simulation meshes for all our computations in this work.

4.2.6 Analytical estimates using an effective-medium approximation

To additionally probe the consistency of our computations, we will use, as a useful test, semi-analytical results that we will calculate using the so-called effective-medium equations (EM approximation). The EM approximation was first introduced by Bruggeman [110] for general random inhomogeneous materials, and then adapted, *e.g.*, by Maza and coworkers [91] for HTS with Gaussian random T_c distributions. As shown in those early works, the EM approximation is a coarse-averaging model that may be considered accurate for temperatures not too close to the $R \to 0$ point (at which percolation effects may be expected to fully invalidate the approximation). In the case of our 2D media, the EM equations may be summarized as the following implicit condition for the conductivity σ of each region with random doping inhomogeneities: [91]

$$\int_0^\infty \frac{\sigma_p - \sigma}{\sigma_p + \sigma}\, \omega(p, \overline{p}) \mathrm{d}p = 0. \tag{4.11}$$

Here, p, $\overline{p}$ and $\omega(p, \overline{p})$ retain the same meaning as in Equation (4.10), and σ_p is the electrical conductivity corresponding to doping level p. The above equation has to be numerically solved to obtain σ; however, the computational weight is much lower than the finite-element computation method (seconds versus hours or even days in our parallel computer [89]).

In our case the HTS bolometer is bigger than the size of a monodomain with a doping p so this lead us to a two-dimensional problem of resistances in series and in parallel. The problem is not going to be tridimensional because of the anisotropy of the cuprates, i.e., the resistivity in the c-direction is approximately 80 times higher than in the ab direction, [111] so the charge transport is mainly in the in-plane direction.

The effects of these critical temperature inhomogeneities over the paraconductivity $\Delta\sigma$ in a domain may be easily taken into account in a more approximately way by means of the effective-medium approximation for superconductors with a random normal distribution of critical temperatures uniformly distributed in space:

$$\int_0^\infty \frac{\rho - \rho_p}{\rho + \rho_p}\, \omega(p, \overline{p}) \mathrm{d}p = 0. \tag{4.12}$$

Here σ is the global conductivity of the sample (the inverse of the total resistivity ρ), σ_p is a conductivity of a single domain with a value p of the concentration of dopants, $\alpha = D - 1$ is a parameter which depends on the shape and dimension D of the network [112] (so $\alpha = 1$ in our case) and ω is the Gaussian distribution of doping of a whole domain, defined in 4.10.

Solving the Equation (4.12) taking into account the Equations (4.7)–(4.10), we get the analytical approach to the conductivity of an HTS with the same nominal doping $\overline{p}$ that we are going to use in this article to verify the finite element calculations.

It is important to remark that this estimation has some drawbacks to describe the the $R(T)$ transition in a precise way. This approximation loose its validity when there are enough domains in superconducting state to create percolation paths for the current. Therefore, in this region of temperatures it is going to overestimate the resistance of the HTS. However, this feature is well described by the Finite Element computations.

4.3 Results for structured non-patterned HTS TES

The aim of the section is twofold. First we present the results obtained, using the methodology explained in Section 4.2, for non-patterned HTS TES sensors, *i.e.*, films in which the doping structuring is solely produced by the unavoidable doping inhomogeneity always present in real HTS films. While these effects (as already briefly commented in our introduction) are quite negligible in the optimally-doped compositions, this section will show that for underdoped HTS this intrinsic doping structuring may already significantly improve the bolometric characteristics of HTS TES.

A second purpose of this section will be to compare these results with available (measured, *e.g.*, in [92] but never used for bolometers for non-optimal dopings) experimental data for $R(T)$ in non-patterned HTS TES films with different nominal dopings. [92] The good agreement with these data will confirm the validity of the basic methodology used in our computations (confirmed as well by the EM approximations). Therefore, these validations reinforce our conclusion that HTS TES composed by a non-patterned but underdoped superconductor may significantly improve the main bolometric operational parameters with respect to the optimally-doped HTS TES proposed up to now, because of their intrinsic T_c-structuring associated to the underdoped compositions.

4.3.1 Results for the $R(T)$ profile and bolometric operational parameters

We have performed, firstly, $R(T)$ finite-element computations for bolometers with uniform nominal doping $\overline{p}$. In Figure 4.1 we show the results for the case of YBCO films with nominal dopings $\overline{p} = 0.135, 0.140, 0.147$ and 0.155, represented as circles, squares, diamonds and triangles, respectively. As previously mentioned, to these nominal dopings it has to be added a random intrinsic structuration (following a Gaussian distribution as per Equation (4.10)), in order to obtain the local $p(x, y)$ values; this is illustrated by the zoom in the scheme drawn in Figure 4.1.

As clearly visible in that figure, the reduction of $\overline{p}$ induces not only a shift of the transitions towards somewhat lower temperatures (as expected from the T_c-vs-$\overline{p}$ phase diagram of HTS), but also a widening of the T-width of the transition region. The gray areas in Figure 4.1 are the T-range, ΔT, in which the $R(T)$

bolometer	**ΔT** (K)	**TCR** (K^{-1})	$\mathbf{P}^{\max}$ (10^{-3} W)	$\mathbf{E}^{\max}$ (10^{-8} J)	τ (10^{-6} s)
semiconductor: V_2O_5	25 [34]	0.026 [34]	95	240	25
optimally-doped YBCO:					
$\overline{p} = 0.155$	0.9	3.05	5.3	3.4	6.4
structured non-patterned YBCO					
$\overline{p} = 0.147$	1.8	2.67	10	6.6	6.2
$\overline{p} = 0.140$	2.3	2.15	13	7.8	5.9
$\overline{p} = 0.135$	4.7	2.16	25	14	5.5
structured patterned YBCO:					
linear $\overline{p}(x)$	1.4	0.25	8.4	5.4	6.4
exponential-like $\overline{p}(x)$	8.3	0.18	48	30	6.1
4-step exponential-like $\overline{p}(x)$	12.7	5.13	72	42	5.8

Table 4.1: Operational parameters for different types of microbolometer sensors, including first existing sensors using semiconductors (V_2O_5) or non-structured optimally-doped HTS TES (YBCO with $\overline{p} = 0.155$), and then the novel options explored in this work: structured non-patterned HTS TES (YBCO with $\overline{p} \leq 0.155$, see our Section 8.5) and patterned HTS TES (with the three example pattern designs discussed in our sections 4.5 to 4.7). We consider, for all the options, the same film dimensions ($(6\,\mu\mathrm{m})^2$ section, 100 nm thickness), the same type of thermal link (substrate directly in contact with the heat sink), and in general the same values for the rest of parameters affecting the bolometric performance (as per Subsection 4.2.1). Note, for instance, the significant advantages that a discretized exponential-like pattern achieves versus non-structured YBCO, even approaching V_2O_5 in areas where previous HTS TES were not competitive against it. See main text for details

transition occurs and R-vs-T is linear, *i.e.*, the operational interval ΔT of Equation (4.2). This ΔT increases as $\overline{p}$ decreases, as be noticed both in Figure 4.1 and in Table 4.1. This Table summarizes the numerical values that can be obtained from these $R(T)$ curves, and also the rest of bolometric parameters calculated as per subsection 4.2.1 for each of those films.

It is important to remark that the increase of ΔT (about 5 times higher between the maximum and minimum nominal dopings analyzed) when decreasing the nominal doping of the film is translated in an enhancement of the parameters $E^{\max}$ and $P^{\max}$ of the bolometer. This means that this kind of bolometers are able to receive a higher amount of radiation without saturating. Note that a larger ΔT also implies a less demanding cryogenic setup in terms of stability. It also leads to a larger incident power saturation threshold.

Finally, the time parameter τ does not vary much between all the HTS microbolometers considered in this Section because it mainly depends on the operational temperature T^{-} via the heat capacity and the thermal conductance and, in this region, the ratio between these parameters is almost constant with temperature. [93, 94]

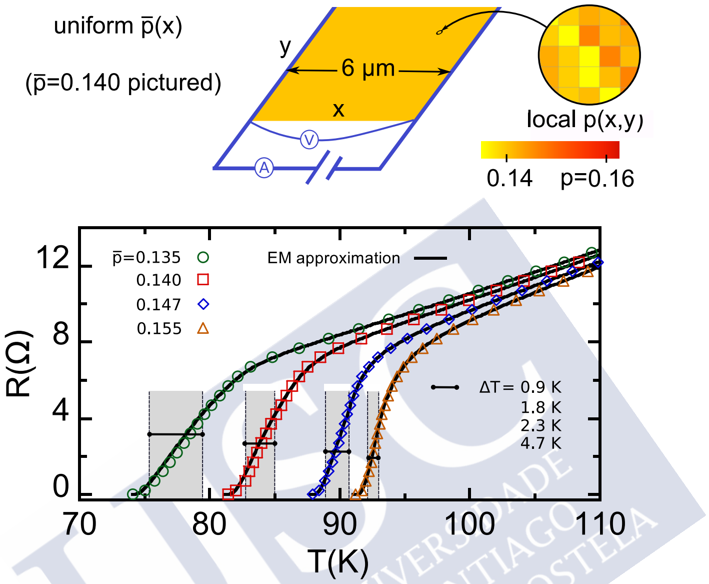

Figure 4.1: Resistance R versus temperature T obtained for YBCO thin films with a single, uniform value for the nominal doping level $\overline{p}$, including the case with negligible T_c nanostructuration (or optimal doping $\overline{p} = 0.155$ in which T_c saturates near its maximum value and T_c disorder is negligible) and various cases in which the $\overline{p}$ value corresponds to significant T_c nanostructuration (see Sections 4.2 and 8.5 for details). The data points correspond to the finite-element computations, and the continuous lines to the analytical EM approximation (see Equation (4.12)). The shaded gray region signals the operational temperature range ΔT (in which R is strongly dependent and linear in T). In the upper drawing we image the simulated sample and setup, including also a zoom at smaller length scales illustrating the spatial variation of the local doping level $p(x, y)$ (each $p(x, y)$ monodomain has typical size $(30\text{ nm})^2$ and the distribution is Gaussian around the average $\overline{p}$(x), see main text for details).

On the other hand, with the help of Table 4.1 it is also possible to compare these bolometric parameters with the typical values of classical Vanadium oxide bolometers. It is remarkable that the TCR values of the HTS TES considered in this Section are 2 orders of magnitude higher than the value for the V_2O_5 bolometer. This means that this HTS TES have higher sensitivity to measure the radiation. It is also interesting that the time constant is lower in HTS TES, which means that they have a faster thermal response. However, the ΔT in V_2O_5 bolometers is one order of magnitude higher than the value of the type of HTS TES considered in this section. Therefore, this type of HTS TES saturates much before than V_2O_5 bolometers (as also shown, in fact, by the $E^{\max}$ and $P^{\max}$ values in Table 4.1). Thus, our next goal in this work will be to increase ΔT to improve the amount of radiation that the HTS TES are able to receive without achieving the saturation point. This will be done by considering doping structurations beyond the intrinsic random disorder of the doping level.

4.3.2 Verification using the analytical EM approximation

Figure 4.1 also shows, as continuous lines, the results obtained by applying the EM approach, *i.e.*, Equation (4.12), to the same parameter values and doping levels as used in the previous subsection. It can be seen in that figure that the coincidence between the finite-element computation and the EM approximation is excellent, even in the $R \to 0$ tails (a log-log zoom of such tails evidences moderate deviations in relative values, negligible in the absolute scale of Figure 4.1, as coherent with the expectation that the EM approximation is less accurate when percolative current paths appear, [91, 110] what happens when $R \sim 0^+$(see also Figures 4.2 and 4.3 that better evidence these $R \sim 0^+$ deviations). [102] This comparison gives, therefore, a first argument supporting the validity, at least concerning the main features, of our calculation methods for the doping structuring effects in HTS TES.

4.3.3 Verification against existent measurements

To test the accuracy of our finite-element calculations (and also those using the EM approximation) we have plotted in Figures 4.2 and 4.3 the data measured in Reference [92] in high quality YBCO ($YBa_2Cu_3O_\delta$) films comprised by a single zone of nominal oxygen stoichiometries $O_{6.78}$ and $O_{6.85}$ (*i.e.*, $\overline{p} \simeq 0.140$ and $\overline{p} \simeq 0.156$ respectively; to get the relations between oxygen ratio and doping we have interpolated the experimental data described in Reference [113]).

We can see in these figures the good accuracy of the theoretical (EM approach) and computational (finite-element) methods used in this article to reproduce the experimental resistance curves of non-patterned YBCO films in the studied doping range.

Note that these existing non-optimal YBCO fils have never been used to implement HTS TES. Our present considerations obviously indicate that such implementation would be of interest.

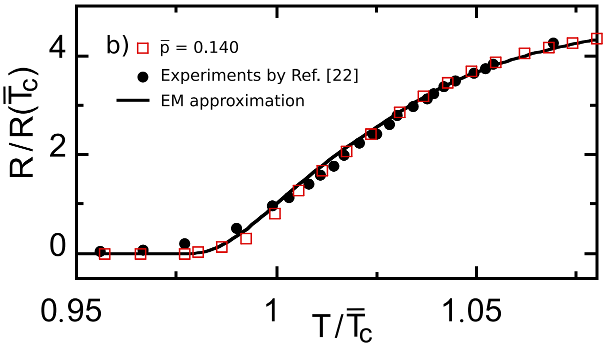

Figure 4.3: Comparison between the resistance vs temperature resulting from our methodology (open symbols for the finite-element computations and solid line for the EM analytical approximation) and the measurements of Reference [92] (solid symbols), for YBCO films with uniform nominal oxygen stoichiometry $O_{6.78}$ (corresponding to $\overline{p} = 0.140$, *i.e.*,a T_c-structured non-patterned HTS).

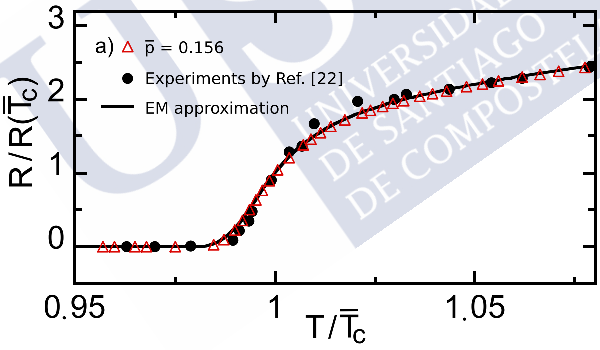

Figure 4.2: Comparison between the resistance vs temperature resulting from our methodology (open symbols for the finite-element computations and solid line for the EM analytical approximation) and the measurements of Reference [92] (solid symbols), for YBCO films with uniform nominal oxygen stoichiometry corresponding to $\overline{p} = 0.156$, *i.e.*, very near from the optimal doping level. Note that the normalization of the axes significantly zoom the transition region with respect to the Figure 4.1.

4.4 Methods for patterned HTS TES

Let us now study the $R(T)$ curve of HTS films in which a regular pattern of nominal doping levels is imposed, with the aim to obtain pattern designs that optimize the bolometric functionality. In these films, a regular spatial variation of the nominal doping level $\overline{p}$ is created by the samples' grower by using any of the different methods developed in the recent years by experimentalists in HTS films (see, *e.g.*, References [42, 43, 47]). In what follows, all the specific example patterns considered in this work will be expressible as functions $\overline{p}(x)$, where x is the coordinate in the direction perpendicular to the experimental current (see scheme in Figure 4.1). It will be also useful for our subsequent descriptions to introduce the corresponding function $\lambda(\overline{p})$, or relative length weight of each nominal $\overline{p}$ value in the film, defined as

$$\lambda(\overline{p}) = \frac{1}{L}\frac{dx}{d\overline{p}}; \tag{4.13}$$

where L is the length of the film in the x-direction.

Crucial for our studies, one has still to add to these nominal $\overline{p}(x)$ variations the unavoidable microscopic-scale randomness of the doping level (considered in the previous sections), *i.e.*,

$$p(x,y) = \overline{p}(x) + p_{\text{random}}(x,y), \tag{4.14}$$

with $p_{\text{random}}(x,y)$ consistent with Equation (4.10) evaluated using the local $\overline{p}(x)$.

Naturally this double, two-scale spatial variation considerably difficult the task of calculating the resistive transition of these films, for what we have implemented the methodology that we describe next.

4.4.1 Obtainment of the $R(T)$ curve of patterned HTS TES using finite-element computations

To obtain the $R(T)$ curves of patterned HTS TES, we use the finite-element software TOSERIS already described in Subsection 4.2.5. We again use a 200 × 200 simulation mesh and now we assign to each of those finite elements a local doping as follows: First, we associate to each element i a nominal doping $\overline{p}_i$ corresponding to the pattern to be simulated. Then we randomly calculate the local doping p_i following the Gaussian distribution given by Equation (4.10), evaluated with the nominal doping $\overline{p}_i$ of each node. Finally, to each node we assign the T_{ci} and $\rho_i(T)$ corresponding to their local p_i as per the quantitative results of Reference [96] for the HTS material YBCO (see Subsections 4.2.2 and 4.2.3).

We also tested that the sets of nodes sharing the same $\overline{p}_i$ value to follow the Gaussian distribution, and each $R(T)$ simulation was repeated for several so-generated samples to verify their reproducibility. These tests indicate that our choice of a 200×200 node mesh provides enough statistical size. If we attribute to each node the size of $(30\,\mathrm{nm})^2$ corresponding to each T_c-monodomain in YBCO (see Section 4.2.4 and References [103,108]), the whole 200×200 sample corresponds to $(6\,\mu\mathrm{m})^2$, that is realistic for a bolometer pixel.

Unless stated otherwise, we will use in our contributions the numerical values in Sections 4.2.2 to 4.2.5 for the common material characteristics, such as, *e.g.*, a film thickness of 100 nm or the different critical fluctuation parameters as per Section 4.2.3.

4.4.2 Analytical estimates using an extended-EM approximation

Besides performing finite-element computations, we are going to test our results against estimates based on the EM approach, for which purpose we must first suitably extend this approximation to account for the 1D gradient of nominal dopings corresponding to each example pattern to be considered in this work. For that, we consider the film as an association in series of domains, each one with its own resistance and nominal doping $\overline{p}$. Thus the total resistance is then the sum of the resistance of each domain, *i.e.*:

$$R(T) = \int_{x=0}^{x=L} \frac{\mathrm{dx}}{\sigma(\overline{p}(x), T)S} \tag{4.15}$$

where L is again the total length of the bolometer, S is the transversal surface, and $\sigma(\overline{p}(x), T)$ is the conductivity obtained using the monodomain EM approach, *i.e.*, using Equation (4.12) for each doping $\overline{p}(\mathrm{x})$. Equation (4.15) can be also written as the following over nominal doping, with the help of the $\lambda(\overline{p})$ function defined in Equation (4.13):

$$R(T) = L \int_{\overline{p}_0}^{\overline{p}_L} \lambda(\overline{p}) \frac{\mathrm{dx}}{\sigma(\overline{p}(x), T)S}. \tag{4.16}$$

For a discrete distribution (stepwise function $\overline{p}(x)$), the above equations become discrete summations: Where $\overline{p}_i$ is the nominal doping of the bolometer in at the beginning of the bolometer ($x = 0$), $\overline{p}_f$ is the nominal doping in the end of the bolometer ($x = L$) and $\lambda(\overline{p}) = (1/L)dx/d\overline{p}$ is the relative weight of each domain of doping $\overline{p}$ in the sample. The value of $\lambda(\overline{p})$is given by equation 4.19 for this pattern.

$$R(T) = \sum_{i=1}^{N} \frac{L_i}{\sigma(\overline{p}_i, T)S}, \tag{4.17}$$

where N is the number of discrete domains, each with its own nominal doping $\overline{p}_i$ and length L_i.

Note that Equations (4.15) to (4.17) do not explicitly take into account the transverse currents when associating the different domains $\overline{p}_i$ and L_i. Non-longitudinal transport inside each domain is built-in by using the EM approach for each $\sigma(\overline{p}_i, T)$. However, this approximation may be expected to fail when it has to describe percolations (because both the sum in series between domains and the EM approximation do not take this into account). This can make this approximation overestimate the value of $R(T)$ in the very close proximity to the superconducting state, where percolations are expected to be important.

4.5 Results for HTS TES structured with a linear $\overline{p}(x)$ variation

In the remainder of this article, we shall apply our methodology to different instances of doping-patterned HTS TES, seeking to progressively identify pattern design optimizing the bolometric sensor performances. In this section, in particular, we consider a simple linear variation of $\overline{p}$ along the longitudinal direction (the direction of the overall externally-applied electrical current, see scheme in Figure 4.4):

$$\overline{p}(x) = \overline{p}_0 + \left(\frac{\overline{p}_L - \overline{p}_0}{L}\right) x, \tag{4.18}$$

where $\overline{p}_0$ and $\overline{p}_L$ are the $\overline{p}$-values at the opposite ends of the film $x = 0$ and $x = L$. In terms of the $\lambda(\overline{p})$ function of Equation (4.13), this linear-in-x $\overline{p}$-pattern simply becomes the constant value

$$\lambda(\overline{p}) = \frac{1}{\overline{p}_L - \overline{p}_0}. \tag{4.19}$$

More specifically, we have chosen for our computations the rather typical values $\overline{p}_0 = 0.135$ and $\overline{p}_L = 0.161$.

4.5.1 Results for the R(T) profile and bolometric operational parameters

The results of our numerical finite-element evaluation for this $\overline{p}$-pattern are displayed in Figure 4.4 (see also Table 4.1 for a comparative summary). The spatial pattern imposed to the HTS TES bolometer is drawn in the upper row of the Figure 4.4.

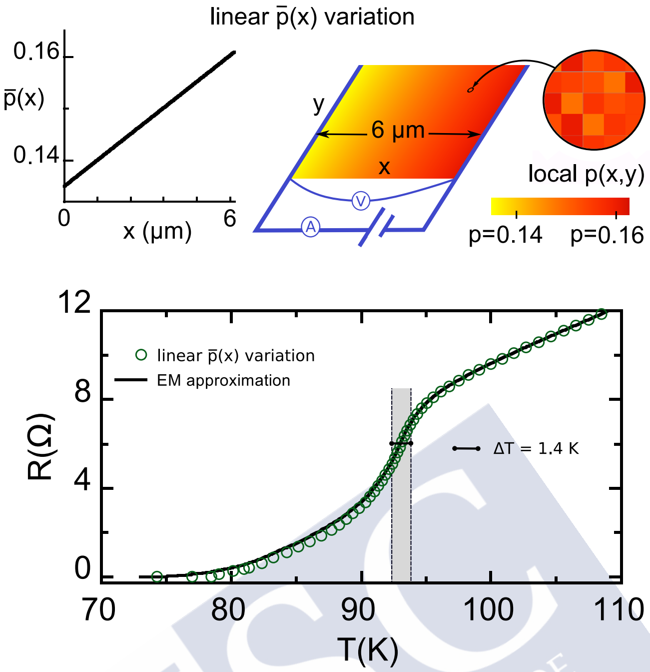

Figure 4.4: In the upper row, we illustrate a YBCO film patterned following the linear variation of the nominal doping $\overline{p}(x)$ studied in Section 4.5 (see Equations (4.18) and (4.19)). We also illustrates doping over the film as a 2D color map, taking into account that the local doping level $p(x, y)$ (zoom in the picture) results from accumulating the lineal $\overline{p}(x)$ and the random Gaussian disorder at smaller length scales of about $(30\,\mathrm{nm})^2$ (see main text for details). In the lower row, we plot the resistance vs temperature $R(T)$ that we obtain for such film (data points for finite-element computations, continuous line for the analytical EM approximation, adapted in this work to this $\overline{p}(x)$ case, see Equation (4.20)). Note that the transition widens considerably with respect to Figure 4.1, but the operational ΔT range (shaded gray region) is small due to the nonlinearity of R with T in most of the transition.

As evidenced in that Figure 4.4, this type of structuring of the HTS film significantly broadens the $R(T)$ transition (compare, *e.g.*, with Figure 4.1 that represents, in the same T-scale, the results for HTS TES with comparable but uniform $\overline{p}$-values). However, this structuring does not lead to a linear dependence of R vs T in that transition region. This may pose a difficulty in TES applications, that ideally require a $R(T)$ variation both large (*i.e.*, large TCR) and linear (*i.e.*, constant dR/dT). The range ΔT in which both conditions are met is merely about 1.4 K for this type of $\overline{p}$-pattern, already suggesting that further design optimizations would be desirable (see next Section). In Table 4.1 we summarize the operational parameters obtained for the linear $\overline{p}(x)$ bolometer. We can conclude that they are of the same order or worse than the parameters obtained for an HTS TES bolometer at optimal doping without $\overline{p}$-patterning. This even includes the TCR, that is lower due to the increase of the operational temperature T^- and then of $R(T)$. The maximum energy and power are somewhat higher due to the small increase of the width of the linear regime (but they are below the values for non-patterned but underdoped YBCO). On the other hand, the time constant remains basically the same, because the ratio between heat capacity and thermal conductance remains almost unchanged.

We can conclude that this patterning does not effectively optimize the operational parameters of the HTS TES, mainly because it broadens the $R(T)$ transition but does not achieve $R(T)$ linearity in it. Better tuned $\overline{p}(x)$ variations need to be found (See Sections 4.6 and 4.7) to neatly surpass the bolometric characteristics of underdoped non-patterned HTS-TES.

4.5.2 Verification using the extended-EM analytical approximation

To check the validity of our results dor the linear $\overline{p}(x)$ variation, we also have used the formulae described in Subsection 4.4.2. For that, our first step has been to combine Equation (4.16) with the $\lambda(\overline{p})$ formula for this type of pattern (Equation (4.19)). This leads us to the new equation:

$$R(T) = \frac{L}{S(\overline{p}_L - \overline{p}_0)} \int_{\overline{p}_0}^{\overline{p}_L} \frac{d\overline{p}}{\sigma(\overline{p}, T)} \quad \text{(linear } \overline{p}(x) \text{ pattern)}, \tag{4.20}$$

where $\sigma(\overline{p}, T)$ results from Equation (4.12).

The result of this analytical estimate is displayed in Figure 4.4 as a continuous line. As in the case described for constant nominal doping, this estimate achieves good agreement with the finite-element computation, confirming the basic accuracy of our results. Note that this agreement is somewhat worsened (but still very good at the qualitative level) for the lower tail of the $R(T)$ transition. As already commented in Subsection 4.2.6 and 4.4.2 this slight overestimation of $R(T)$ as $R \to 0^+$ is expected in any EM-type approach and is due to the progressive occurrence of percolation effects as more regions of the film become fully superconductor.

4.6 Results for HTS TES with a continuous exponential-like doping patterning

Seeking to find a $\overline{p}(x)$ profile producing a $R(T)$ transition leading to improved bolometric operational characteristics, we have explored numerous $\overline{p}(x)$ options beyond the simple linear function discussed above. In the present section we present the results that we obtained with the continuous $\overline{p}(x)$ functionality that led us to better bolometric performance (and a step-like, non continuous variation will be later discussed, in Section 4.7). This continuous $\overline{p}(x)$ profile is more intuitively described by means of the auxiliary length-weight function $\lambda(\overline{p})$. In particular, we consider $\overline{p}$-profiles leading to the following exponential $\lambda(\overline{p})$ function:

$$\lambda(\overline{p}) = A\exp\left(\frac{\overline{p}_0 - \overline{p}}{\delta\overline{p}}\right), \tag{4.21}$$

where $\delta\overline{p}$ and A are constants, the latter being easy to obtain by normalization considerations as

$$A = \frac{1}{\delta\overline{p}}\frac{1}{1-\exp\left(\frac{\overline{p}_0-\overline{p}_L}{\delta\overline{p}}\right)}. \tag{4.22}$$

In these equations $\overline{p}_0$ and $\overline{p}_L$ are, as in the previous sections, the nominal doping at $x = 0$ and $x = L$ respectively, being L the size of the film. Note that, by applying Equation (4.13), this corresponds to the following $\overline{p}(x)$ profile:

$$p(x) = \overline{p}_0 - \delta\overline{p}\ln\left\{1-\frac{x}{L}\left[1-exp\left(\frac{\overline{p}_0-\overline{p}_L}{\delta\overline{p}}\right)\right]\right\} \tag{4.23}$$

For the case of YBCO films considered in this article, and for $\overline{p}_0 = 0.135$ and $\overline{p}_L = 0.161$ as already used in the previous section, we found that the $\delta\overline{p}$ value that best optimizes the bolometric characteristics (most notably ΔT) is $\delta p = 0.007$. Besides these $\overline{p}_0$ and $\overline{p}_L$ values, we employed in our evaluations the same common parameter values as described in our Sections 4.2.3 to 4.2.5 about methodology.

In the upper row of Figure 4.5 the corresponding doping profile is drawn, both as a $\overline{p}(x)$ representation and as a 2D color density plot. It may be noticed that at the qualitative level the $\overline{p}(x)$ function itself is not too dissimilar to an exponential (however a purely exponential dependence of $\overline{p}$ with x would produce however less optimized bolometric performance).

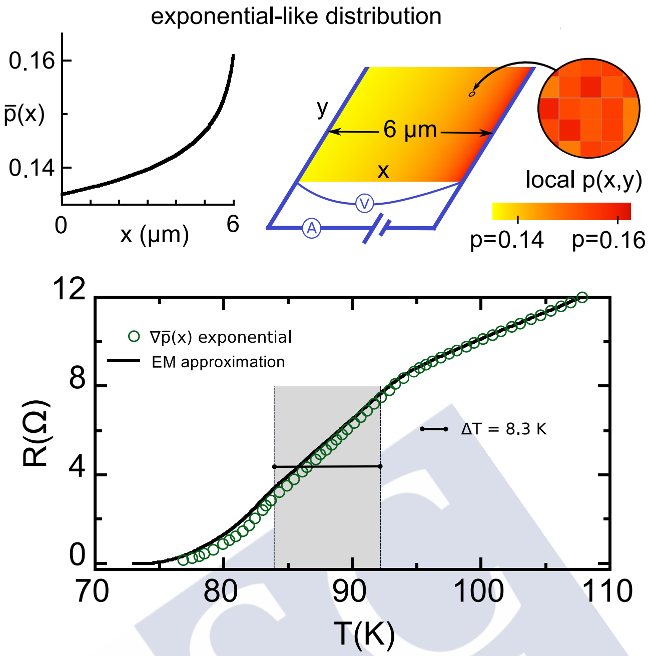

Figure 4.5: In the upper row, we illustrate a YBCO film patterned following the exponential-like variation of nominal doping $\overline{p}(x)$ studied in Section 4.6 (see Equations (4.21) to (4.23)). We also illustrates doping over the film as a 2D color map, taking into account that the local doping level $p(x, y)$ (zoom in the picture) results from accumulating the exponential-like $\overline{p}(x)$ and the random Gaussian disorder at smaller length scales of about $(30\,\mathrm{nm})^2$ (see main text for details). In the lower row, we plot the resistance vs temperature $R(T)$ that we obtain for such film (data points for finite-element computations, continuous line for the analytical EM approximation, adapted in this work to this $\overline{p}(x)$ case, see Equation (4.26)).

4.6.1 Results for the R(T) profile and bolometric operational parameters

The results of our numerical finite-element evaluation for this $\overline{p}$-pattern are displayed in the second raw of Figure 4.5 (see also Table 4.1 for a comparative summary). As evidenced in that Figure 4.5, not only the transition is significantly broadened with respect to the one of non-patterned HTS TES but also (unlike what happened in the case of a linear $\overline{p}(x)$ variation) the region ΔT of the transition with linear $R(T)$ dependence is highly increased. In particular, the ΔT region is increased up to 8.3 K, almost 10 times more than in the case of non-structured, optimally-doped

The operational parameters derived from this broadened linear region of the transition are displayed in Table 4.1. First of all, it is important to remark that the increase in ΔT directly improves the parameters $E^{\max}$ and $P^{\max}$ of the bolometer, increasing the maximum radiation power that it can receive without achieving the saturation point. In fact, we achieve $P^{\max} = 4.8 \times 10^{-2}$ W with this structuring, *i.e.*, one order of magnitude larger than for the optimal doping used up to now to fabricate HTS TES bolometers. The improved $P^{\max}$ is only one half the value for equivalently sized V_2O_5 bolometers, making a HTS TES design, for the first time, competitive in this feature against semiconducting bolometers. However, we must also note that other operational parameters of the bolometer have worsened somewhat with this structuring. This is the case of, mainly, the TCR, that is one order of magnitude lower than in the case of conventional HST TES, although it is still higher than for V_2O_5 (this shortcoming and other improvements will be addressed in Section 4.7 with an evolved $\overline{p}$-pattern design). Finally, the time constant τ maintains its value due to the almost constant ratio between heat capacity and thermal conductance.

4.6.2 Verification using the extended-EM analytical approximation

We have checked our results also using an analytical estimate, by adapting to this pattern the effective-medium approach described in Section 4.4.2. For that, we have combined Equation (4.16) with the $\lambda(\overline{p})$ expression defining this $\overline{p}$-pattern (Equation (4.23)), to obtain the new equation:

$$R(T) = \frac{AL}{S}\int_{\overline{p}_0}^{\overline{p}_L} \exp\left(\frac{\overline{p}_0-\overline{p}}{\delta\overline{p}}\right)\frac{d\overline{p}}{\sigma(\overline{p},T)} \quad \text{(exp-like pattern)}, \tag{4.24}$$

where $\sigma(\overline{p},T)$ results from the Equation (4.12). The result of this analytical estimate of the structured YBCO film is displayed in Figure 4.5 as a continuous line. Again the EM-type estimate slightly overestimates $R(T)$ in the tail of the transition, but basically confirms the finite-element results. As already mentioned above the overestimation is expected to be linked to precursor percolation effects.

4.7 Results for HTS TES with a 4-step exponential-like doping patterning

While the $\overline{p}(x)$-pattern design considered in the previous section produced notable improvements of the bolometric features, at least two concerns may be expressed about it: First, current structuration techniques such as local ferroelectric field-effect [42], nanodeposition [43] or focused ion beam [44] may have difficulties producing such a smooth exponential-like variation of $\overline{p}$ with x (see Equations (4.21) to (4.23)). Instead, it would be preferable a simpler and, mainly, *discrete*-pattern, *i.e.*, one comprised of a few zones, each with a single $\overline{p}$. Secondly, the continuous-pattern of the previous section presents somewhat worsened TCR value with respect to some of the non-patterned HTS TES.

To address both issues, we consider now the discrete $\overline{p}(x)$ pattern described in the upper row of Figure 4.6. This pattern defines 4 zones, each with a single uniform $\overline{p}$ chosen to optimize the linear region of the transition. These values of $\overline{p}$ also follow a discretized version of the exponential pattern:

$$L_i = B \exp\left(\frac{\overline{p}_0 - \overline{p}_\mathrm{i}}{\delta p}\right), \tag{4.25}$$

where L_i is the length of the zone of nominal doping $\overline{p}_\mathrm{i}$, and B is a normalization constant such as $\sum_i L_i = L$. The resulting 4-step variation of $\overline{p}(x)$ should be certainly easier to obtain with current structuration experimental techniques, for instance by three successive stages of doping reduction, each with a part of the film protected by a mask of different length for each stage. Naturally, as in the previous cases, we must add to this nominal-$\overline{p}$ pattern the random Gaussian variation of the local $p(x, y)$ values as already described in Section 4.2.4.

We tested the bolometric performance for various doping levels $\overline{p}$ of the four zones. We obtained the best results with the set $\overline{p}$ = 0.136, 0.141, 0.145 and 0.160, that we describe in what follows.

4.7.1 Results for the R(T) profile and bolometric operational parameters

The results for our numerical finite-element evaluation for this $\overline{p}$-pattern are displayed in Figure 4.6 (see also Table 4.1). As evidenced there, the $R(T)$ transition becomes significantly broad and linear, with such linear region conveniently starting at $T^- = 76.6\,\mathrm{K}$ (so that the bolometer could be operated with the simplest liquid-nitrogen bath, at 77 K). The corresponding ΔT is now almost 13 K, the largest obtained in this paper (and even competitive with the typical value 25 K for sensors of similar size). Also the TCR value $> 5\,\mathrm{K}^{-1}$ is the largest obtained in this paper, being almost double than for conventional non-structured optimally-doped YBCO (and about 200 times the value typical for a V_2O_5 semiconductor). The E^max and P^max values (see Table 4.1) also reflect these improvements, being again the best among the HTS options considered in this work and more than one order of magnitude larger than for the nonstructured optimally-doped HTS TES proposed until the present work (and even similar to the value of V_2O_5).

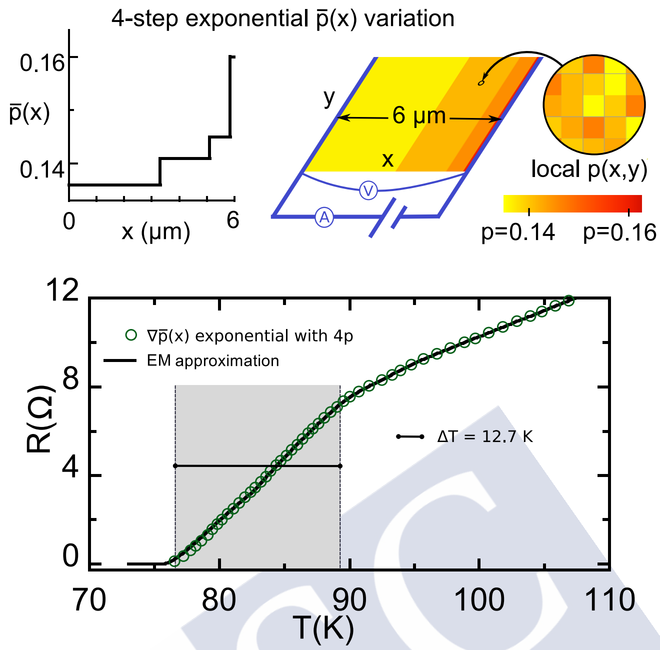

Figure 4.6: In the upper row, we illustrate a YBCO film patterned following the discretized 4-step exponential-like variation of the nominal doping $\overline{p}(x)$ studied in Section 4.7. we also illustrates doping over the film as a 2D color map, taking into account that the local doping level $p(x, y)$ (zoom in the picture) results from accumulating the 4-step exponential $\overline{p}(x)$ and the random Gaussian disorder at smaller length scales of about $(30\,\mathrm{nm})^2$ (see main text for details). In the lower row, we plot the resistance vs temperature $R(T)$ that we obtain for such film (data points for finite-element computations, continuous line for the analytical EM approximation, adapted in this work to this $\overline{p}(x)$ case, see Equation (4.26)). This is the most optimized design found in this work for the purpose of bolometric operation (see also Table 4.1).

To sum up, these finite-element computations reveal that this relatively simple $\overline{p}$-pattern produces order-of-magnitude improvements over non-structured HTS TES in ΔT, $P^{\max}$ and $E^{\max}$, and also 66% improvement in TCR sensibility. The proposed design makes HTS TES fully competitive with V_2O_5 in all the studied parameters, while retaining the typical two-orders-of-magnitude advantage in TCR sensibility with respect to such V_2O_5 sensors.

4.7.2 Verification using the extended-EM analytical approximation

We have checked our results for this 4-step $\overline{p}$(x) pattern also using an analytical estimate, by adapting to this pattern the effective-medium approach described in Section 4.4.2. In this case we used the discretized version of those approaches, given by Equation (4.17) and (4.25). By combining these Equations with the $\overline{p}(x)$-pattern considered in this section we now obtain:

$$R = \frac{B}{S}\sum_{i=1}^{N}\frac{1}{\sigma(\overline{p}_i, T)}\exp\left(\frac{\overline{p}_0 - \overline{p}_i}{\delta\overline{p}}\right), \tag{4.26}$$

where $\overline{p}_i$ corresponds to the nominal doping of each of the i = 1,... 4 zones and $\sigma(\overline{p}_i, T)$ are obtained from Equation (4.12).

The result of this analytical estimate is displayed in Figure 4.6 as a continuous line. This figure shows that the estimate fully confirms the main features obtained by finite-element computations. Similarly to the case of the other $\overline{p}$-patterns considered in our work, the estimate is expected to be less reliable in the lower part of the transition, at which percolation effects begin to appear.

4.8 Conclusions

To sum up, we considered the advantages of structuring and patterning of the doping level (and hence of the critical temperature) in high-temperature superconductors with respect to their operational characteristics as bolometric sensors (HTS TES) of electromagnetic radiation.

As a way to summarize the results of our studies, we graph in Figure 4.7 (see also Table 4.1) our findings for some of the main bolometric functional parameters found in this work. For the sake of comparison, the Figure 4.7 also indicates the typical values for semiconducting V_2O_5 bolometers of similar size and for a high-temperature superconductor of uniform nominal composition $\mathrm{YBa_2Cu_3O_{6.93}}$ (*i.e.*, to the non-structured HTS TES case considered up to now in the literature [36–40]). Our main results are:

i) The HTS TES with a uniform but non-optimal nominal doping level (that leads to intrinsic random Gaussian nanostructuration) may already provide some benefit as bolometers with respect to optimal-doping HTSTES. In particular, they present a widened transition leading to a larger operational temperature interval ΔT and also larger $P^{\max}$ (corresponding to larger maximum detectable radiation power before sensor saturation). However, these improvements come at the cost of a certain reduction of the sensibility of the sensor as measured by the TCR value.

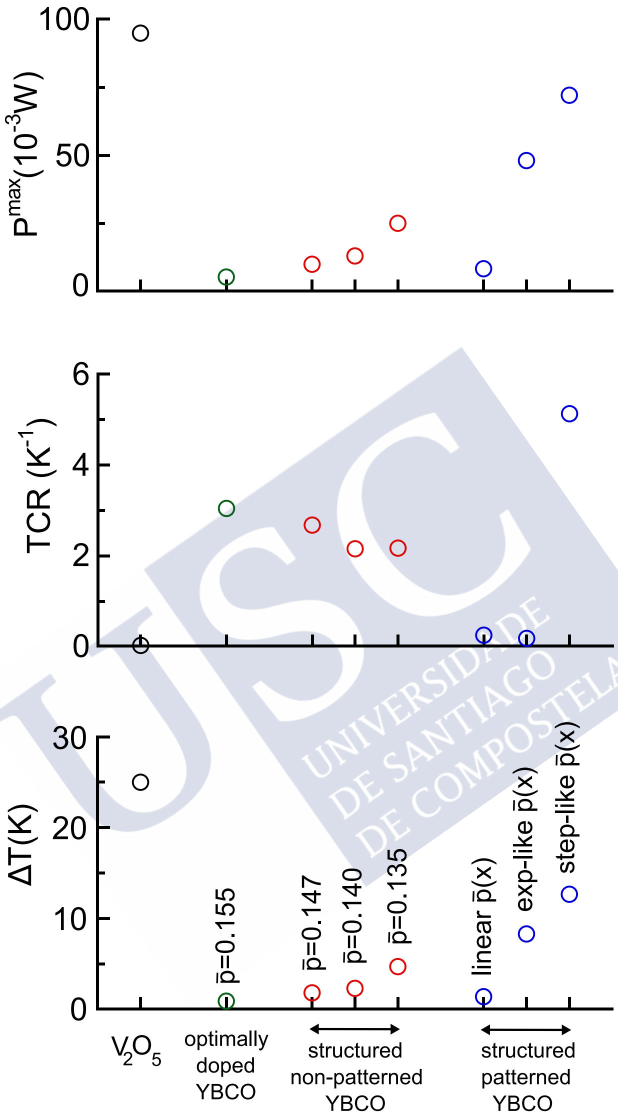

Figure 4.7: Graphical summary comparison of the operational parameters for different types of microbolometer sensors, including existing sensors using semiconductors (V_2O_5) and non-structured HTS TES (YBCO with $\overline{p} = 0.155$), and the novel options explored in this work (structured non-patterned YBCO and structured patterned HTS TES). See also Table 4.1, and main text for details.

ii) The bolometric performance may be significantly more optimized with the use of HTS TES including a regular dependence on position of the nominal doping level $\overline{p}(x)$ (doping level patterning). In that case, ad-hoc pattern designs may be found by progressively seeking widened and linear $R(T)$ transitions. Our more optimized design is shown in Figure 4.6 and consists of just four zones of different sizes and doping levels (related by the exponential-like Equation (4.25) evaluated at $\overline{p}_i = 0.136$, 0.141, 0.145 and 0.160). With this design the operational temperature is conveniently located at $T^- = 76.6\,\mathrm{K}$, the operational temperature interval ΔT is almost 13 K (more than one order of magnitude larger than for the conventional optimally-doped $\mathrm{YBa_2Cu_3O_{6.93}}$, and even competitive with the typical value 25 K for semiconducting V_2O_5 sensors of the same size); the TCR value is $> 5\,\mathrm{K}^{-1}$ (almost double that for the optimally-doped case and about 200 times larger than for V_2O_5), and the $P^{\max}$ and $E^{\max}$ values are also optimized, corresponding to maximum measurable radiation power more than one order of magnitude larger than the optimally-doped case and similar as for V_2O_5.

In consequence, our studies indicate that doping structuration and patterning may provide a way to design optimized high-temperature superconducting bolometric sensors for detection of electromagnetic radiation.


USC
UNIVERSIDADE
DE SANTIAGO
DE COMPOSTELA

Chapter 5

Modification of the resistive transition width of high-temperature superconducting films using 2D T_c-dot patterns

Summary of the chapter:

We extend our studies of HTS TES films with custom micro and nanostructuration of the doping level. In particular, now we consider also 2D microstructure patterns. We show that with custom 2D designs the resistive transition may be not only widened (as achieved in the previous chapter with 1D designs) but also it may be sharpened (as interesting, *e.g.*, to improve the speed of HTS resistive fault-current limiter devices).

5.1 Introduction

Among the applications of superconductors, an example is device components that change their resistance R by orders of magnitude in a delimited temperature range, the vicinity of the critical temperature T_c. [114,115] These may be part of, *e.g.*, bolometers, [116] of super-thermometers sensitive inside a constrained window of temperatures T, [48] etc. The sharpness versus T of the $R(T)$ transition is also of interest in resistive fault current limiters, as it may influence both the occurrence and speed of thermal avalanches and thus their ability to respond to ultrafast current strikes and their recovery time once the fault is cleared. [49, 50]

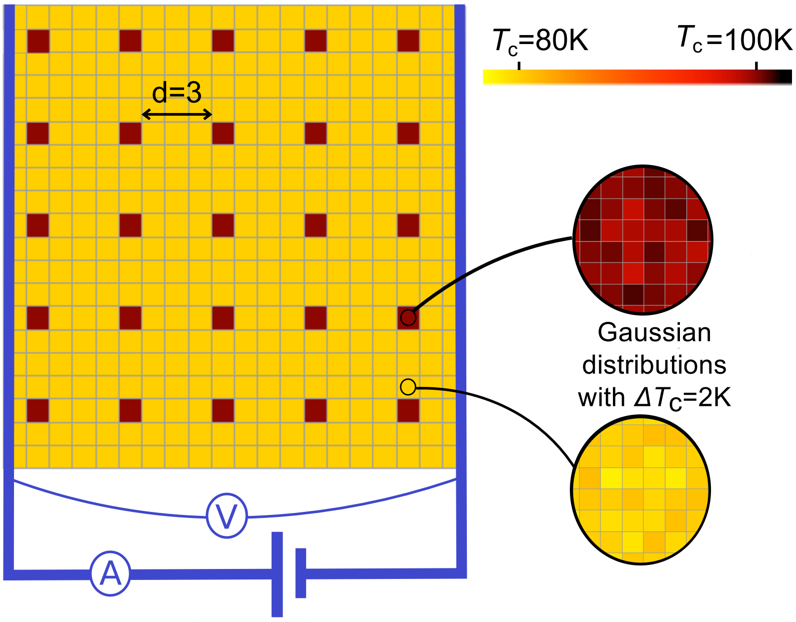

Figure 5.1: Our finite-element representation of a superconducting film with a regular array of T_c-domains, that also considers a Gaussian T_c-distribution inside each domain of the regular pattern as shown in the zooming insets. The example pattern used for this illustration corresponds to the simulation in Fig. 2 with interdomain separation $d = 3$. In typical cuprates, each subcell in the insets is of approximate area $(30\,\mathrm{nm})^2$, so that each cell in the main figure is $(0.3\,\mu\mathrm{m})^2$ and the whole film $(6\,\mu\mathrm{m})^2$. See main text for details.

In these and other superconducting components, the range of temperature over which the change of resistance occurs is not easily custom-engineered, as it is constrained by the T_c value of the superconductor itself and by the T-width of its $R(T)$ transition. This width is well below 1 K in most low-T_c superconductors. [107, 117] In contrast, in the the high-T_c cuprates the width of the $R(T)$ transition rounding is of about 10K or larger, even in the best samples due to the unavoidable existence of critical phenomena around T_c. [117–119] The latter follow specific power laws with respect to $T - T_\mathrm{c}$ and, thus, custom-engineering the detailed shape of the rounding is also challenging.

In this paper, by means of computer simulations we explore the possibility of custom-broadening and custom-sharpening the resistive transition of high-T_c superconducting films by means of micro- or nano-structuration causing a regular pattern of domains with different T_c values over the film. Realization of this type of regular and controlled patterning has become experimentally possible in the recent years, thanks to advances in different techniques such as, *e.g.*, local ferroelectric field-effect, [42] nanodeposition, [43] focused ion bean, [44] etc. In fact, it has become the specific subject of recent conferences [45] and networks funded by the European Union. [46] While most growers of those structured superconductors have focused up to now on increasing their critical current and achieving collective vortex pinning at certain matching fields, [42–45] our present work proposes that these techniques may also open a way to produce superconducting films designed to have tailored shapes and widths of their $R(T)$ curves.

In section 5.2 we briefly describe our computational methods and parameter values. In section 5.3 we show that broadening the $R(T)$ transition is possible with square array patterns of enhanced-T_c dots. In section 5.4 we show that the opposite effect, *i.e.*, sharpening the $R(T)$ transition, is possible with certain regular patterns of depressed-T_c domains. In section 5.5 we summarize our conclusions.

5.2 Methods

5.2.1 Critical fluctuations

To achieve a realistic simulation of actual patterned high-T_c superconductors, a first necessary ingredient is a precise knowledge of the resistivity $\rho(T)$ near the transition of a single-T_c domain in a cuprate. In that respect, in this paper we shall restrict ourselves to a manageable case, the ohmic regime with no external applied magnetic field. For that case, it was experimentally shown in cuprates of various dopings and with particularly well characterized inhomogeneity levels that the intrinsic $\rho(T)$ agrees with remarkable accuracy with a single set of equations comprising the different regimes of critical phenomena around T_c; [106, 119–121] a convenient and explicit summary of such equation set may be found in. [106] This achievement reflects, in fact, notable advances in the understanding of the critical phenomena in cuprates (including the so-called Gaussian, uncertainty-principle, and strong phase-fluctuation regimes in layered type-II superconductors

[106, 120, 121]), although for all practical purposes in the present paper they simply provide us a valid empirical approximation to the $\rho(T)$ transition of a single-$T_{\rm c}$ domain in a cuprate.

5.2.2 The role of random inhomogeneities

As explicitly demonstrated in various recent experimental and theoretical works, [101–103, 108, 109] a second crucial ingredient to understand the rounding of the transition in cuprates is to correctly account for the random $T_{\rm c}$-inhomogeneities associated with doping. This disorder exist even in the best cuprate samples and is due to the nonstoichiometry of the dopant ions, that leads to randomness in their placement in the crystal lattice. As shown in [103, 108, 109], the $T_{\rm c}$-domains resulting from the intrinsic disorder lead to Gaussian distributions of $T_{\rm c}$ with dispersions about $\Delta T_{\rm c} \simeq 2\,{\rm K}$, and have a typical planar size of about 30 nm. This $T_{\rm c}$-distribution overimposes a further rounding of the transition, additional to the critical fluctuations. Therefore it becomes necessary, in order to realistically study the $R(T)$ transition of a high-$T_{\rm c}$ film with a regular pattern of $T_{\rm c}$-domains produced by micro or nanostructuration, to also consider that inside each of these patterned domains an additional random Gaussian distribution of $T_{\rm c}$-values exists. Naturally, this significantly increases the computational weight of the corresponding finite-element simulations.

5.2.3 Finite-element computations

To calculate the $R(T)$ transition curves of each of the superconducting films discussed in this work, we wrote ad-hoc software (TOSERIS, available by request to authors) that numerically solves the mesh-current matrix equations of a film modeled, as illustrated in Fig. 1, as a 200×200 square lattice of domains where each domain i may have its own T_{ci} and thus its own resistivity vs. temperature curve. As already mentioned, for the $\rho(T, T_{ci})$ functionality we use the equations explicited in Reference [106]. As Fig. 1 also illustrates, the model includes a power source and a voltmeter connected with zero-resistance contacts to opposite edges of the sample; the $R(T)$ of the film will be obtained as the external V/I. Calculating the circuit requires to solve, for each temperature, a sparse linear system of 40001 variables, the mesh currents. This is a parallelizable computation for which we employed the supercomputer LBTS-εpsilon, which comprises about 12000 floating-point units, is able of 31 Tflops and is described in [89]. It was 100% allocated to run our software during several days.

To assign a T_{ci} to each domain i in our simulations, we employ the following two-step procedure: First, we divide the sample into a 20×20 grid, and associate to each of these cells an average critical temperature $\overline{T}_c$ according to the regular pattern that we want to simulate. Then, each of these cells is in turn subdivided into a 10×10 grid and to each of the resulting subcells a T_{ci} is randomly assigned, following a Gaussian distribution that has mean value the $\overline{T}_c$ of their parent domain in the regular pattern and full-width at half-maximum ΔT_c. Figure 1 illustrates an example.

5.2.4 Parameter values common to all simulations

We perform our simulations with the following numerical values, representative of typical cuprates: For the area of a finite-element domain i, we use $(30\,\mathrm{nm})^2$, which as mentioned in subsection 5.2.2 is expected to correspond to the size of a doping T_c-inhomogeneity [103, 108, 109]. Therefore, a patterned dot in the main Fig. 1 has area $(0.3\,\mu\mathrm{m})^2$, a size well feasible with current micro- and nanostructuration techniques, [42–44] and the whole simulated film is $(6\,\mu\mathrm{m})^2$. For the film thickness we use 100 nm. For the full-width at half-maximum ΔT_c of the random doping T_c-inhomogeneities, we take 2 K (see subsection 5.2.2 and [103, 108, 109]). For the physical parameters entering the critical fluctuation expressions summarized in Ref. [106], we use a parameter set similar to those in our previous works [106] and [102]: in-plane coherence length amplitude $\xi_{ab}(0) = 1\,\mathrm{nm}$, out-of-plane coherence length much smaller than the typical distance between superconducting $\mathrm{CuO_2}$ planes $s \sim 1\,\mathrm{nm}$ (so that fluctuations are in the 2D limit), Ginzburg parameter $\varepsilon_\mathrm{LG} = 0.01$, uncertainty-principle high-temperature fluctuation cutoff $\varepsilon^c = 0.55$, and vortex-antivortex fluctuation parameters $\Delta_\mathrm{BKT} = 2\mathrm{K}$ and $b_0 = 4$. Finally, we take $(10^{-8}\Omega\mathrm{m/K})\,T$ for the normal-state background, *i.e.*, the resistivity at temperatures well above the transition, where fluctuation and T_c-inhomogeneity effects are no longer expected to be appreciable.

5.3 Broadening the $R(T)$ transition with patterns of enhanced-T_c dots

We start by considering the simple case of a square lattice of dots having critical temperature T_c^dot constant and higher than the one of the background areas T_c^back. This corresponds to the example configuration illustrated in Fig. 1. We summarize in Fig. 2 the $R(T)$ obtained from the corresponding simulations, for patterns with different dot packing densities, *i.e.*, different values of the dot interdistance d. These results indicate a two-step-like transition at T_c^dot and T_c^back, as maybe it could have been naïvely expected, at the qualitative level, in advance. It is noticeable that increasing the dot packing density, *i.e.*, decreasing d, increases the widening of the transition. This not only happens through an increase of the height of the R jump at the larger critical temperature, T_c^dot, but also by the less trivial effect (and more relevant for some applications) of diminishing the slope $\mathrm{d}R/\mathrm{d}T$ as $R \to 0^+$: In particular, for the 25% dots configuration, *i.e.*, $d = 1$, that slope is almost halved with respect to its value for the no-dot configuration,

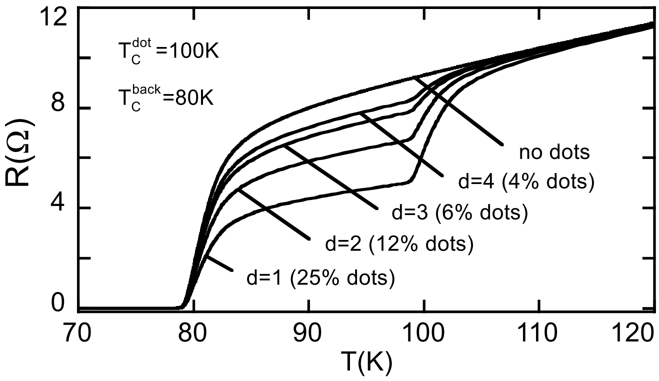

Figure 5.2: Our results for the resistance vs. temperature of a film with a square pattern of dot domains having critical temperature T_c^{dot} constant and higher than the background one, T_c^{back} (see Fig. 1). Note that the step-like broadening of the transition achieved with this patterning is intensified by increasing the dot packing density, *i.e.*, by decreasing the interdomain distance d, given here in units of the number of cells in the main Fig. 1. See main text for details.

being 66% of the value of the no-dot configuration when evaluated at a threshold of $R \simeq 0.5\,\Omega$, *i.e.*, $\rho \simeq 5 \times 10^{-8}\,\Omega$m.

To widen the transition but avoiding the step-like $R(T)$ shape, one possible option is to produce the same dotted patterns, but allowing now a different T_c^{dot} for each column of the array, in particular producing a discretized gradient of T_c^{dot} in the direction from one voltage contact to the other. Our results for that configuration, shown in Fig. 3, no longer present strong step-like features. This is in spite of the discreteness of the T_c^{dot} variations; the reason may be traced back to the rounding due to critical fluctuations and inhomogeneities. As also visible in Fig. 3, increasing the dot packing density, *i.e.*, decreasing d, increases the widening of the transition. It also diminishes the slope $\mathrm{d}R/\mathrm{d}T$ as $R \to 0^+$, this last aspect in a way quantitatively similar to what is achieved without the gradient: The slope $\mathrm{d}R/\mathrm{d}T$ evaluated at $R \simeq 0.5\,\Omega$ for the 25% dots configuration, *i.e.*, $d = 1$, is 66% of the value for the no-dot configuration.

5.4 Sharpening the $R(T)$ transition with patterns of depressed-T_c dots

We now consider regular arrays of dots with a T_c^{dot} lower than T_c^{back}. As it will be shown in this section, this case will produce the interesting situation that the overall $R(T)$ transition of the film will become sharper, instead of broader.

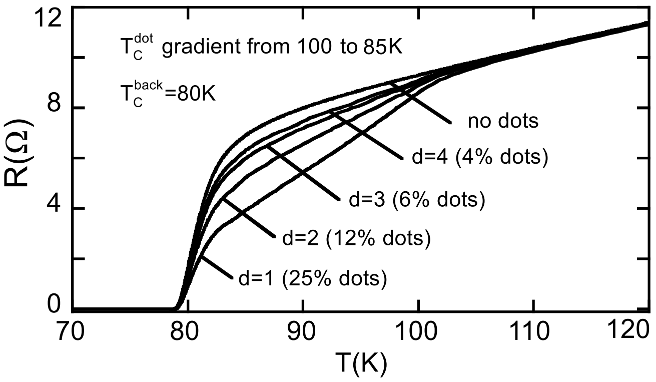

Figure 5.3: Our results for the resistance vs. temperature of a film with a square pattern of dot domains with an enhanced T_{c} which value decreases according to a constant horizontal gradient in Fig. 1. Note that $R(T)$ is no longer step-like as in Fig. 2, and that the transition gets broader by increasing the dot packing density, *i.e.*, decreasing the interdomain distance d, given here in units of the number of cells in the main Fig. 1. See main text for details.

This contrasts not only with the results of the previous section, but also with what would be obtained if the spatial pattern was fully random, in which case simulations and analytical approximations as, *e.g.*, effective medium equations, predict widened transitions [102, 122] in agreement also with measurements in randomly granular cuprates. [122]

Figure 4 shows our simulation results for dotted patterns in which $T_c^{\mathrm{dot}} < T_c^{\mathrm{back}}$, corresponding to the example in Fig. 1 but inverting its color scale, and hence the T_c^{dot} and T_c^{back} values. Note the modest sharpening of the transition, that becomes more pronounced as the dot packing density increases, *i.e.*, as d decreases. This moderate sharpening happens by *i)* a displacement of the inflection temperature ($\mathrm{d}R/\mathrm{d}T$ = max) towards a lower part of the transition and *ii)* an increase of the $R(T)$ slope as $R \to 0^+$. In particular, $\mathrm{d}R/\mathrm{d}T$ evaluated at $R \simeq 0.5\,\Omega$ for the 25% dots configuration, *i.e.*, $d = 1$, is 120% of the value for the no-dot configuration.

A valid question is whether the above moderate sharpening of the $R(T)$ transition could be made stronger by increasing the packing dot density. Given that Fig. 4 already includes the limit $d = 1$ that represents the minimum dot interdistance in our simulation procedures, we explored the effects of increasing the dot packing density by means of elongated dots, *i.e.*, regions of critical temperature T_c^{dot} that would span in Fig. 1 horizontally only one column but vertically a number (henceforth called elongation) of consecutive rows. For the distance between adjacent elongated dots we take always $d = 1$ (in both planar direc-

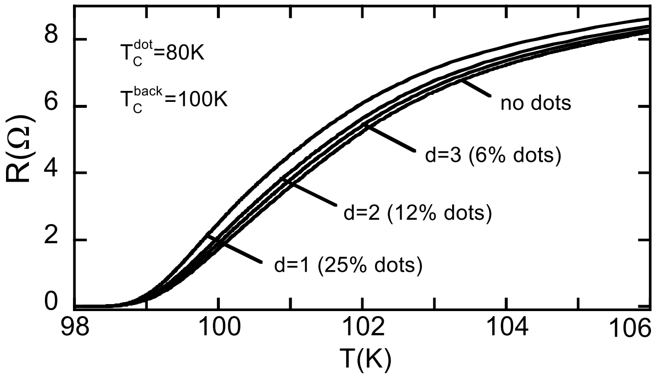

Figure 5.4: Our results for the resistance vs. temperature of a film with a square pattern of dot domains with depressed and constant T_c^{dot}. The $R(T)$ transition becomes sharper as the dot packing density grows by decreasing the interdomain distance d, given here in units of the number of cells in the main Fig. 1. See main text for details.

tions). We show in Fig. 5 our results for those elongated dots. The $R(T)$ of the no-dot configuration is also presented, to ease comparison with Fig. 4. Note that increasing the dot packing density using elongated dots further sharpen the transition significantly. The slope $\mathrm{d}R/\mathrm{d}T$ at $R \simeq 0.5\,\Omega$ also markedly increases, and for the 45% dot configuration, *i.e.*, elongation 4, is almost the double (190%) of the value for the no-dot configuration.

A crude qualitative interpretation of the above $R(T)$ transition sharpening is that the $R(T) \to 0$ temperature is determined mainly by the high-T_c background current paths, while when $R(T)$ begins to be finite it becomes also influenced by the lower-T_c phase, what decreases the rounding due to the large distance to T_c^{dot}.

5.5 Conclusions

We performed numerical simulations of the $R(T)$ curves under zero external magnetic field, in a high-T_c superconducting film with a regular pattern of local T_c-variations induced, *e.g.*, by micro or nanofunctionalization. Our simulations also include the effects of the transition rounding due both to critical fluctuations and to the intrinsic inhomogeneity associated to the nonstoichiometry of dopant ions.

Our results indicate that a regular square lattice of domains with enhanced critical temperature T_c^{dot} may broaden the transition. Also that when the regularly patterned domains have depressed critical temperatures the $R(T)$ transition

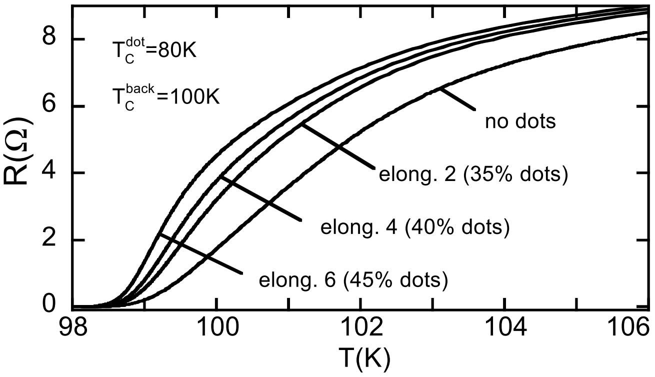

Figure 5.5: Our results for the resistance vs. temperature of a film with a square pattern of elongated dot domains with a depressed and constant T_c. The $R(T)$ transition becomes sharper as the dot packing density grows through the increase of the elongation of the domains. See main text for details.

may become sharper instead of broader. The latter effect markedly increases when the dot packing density is increased, either by making the dots closer to each other or by elongating them.

These studies support therefore the possibility to custom-engineer, on a single thin film, superconducting devices with tailored $R(T)$ curves, obtaining for instance resistive transitions that extend along a widened interval of temperature, or also transitions sharper than what could be obtained from a non-structured cuprate superconductor.

Chapter 6

Hybrid piezoelectric + superconducting devices

Summary of the chapter:

In this chapter we complement our studies in part I and II of this doctoral work of the properties of HTS materials as a function of structure. We present experimental research, (including device preparation and measurements) of hybrid devices consisting on a HTS thin film (YBCO) grown over a piezoelectric substrate (PMN-PT). In these systems, application of a transversal voltage varies the piezomechanical stress over the superconductor, changing its lattice constant and T_c. After some basic characterization of the structure and strain of the device materials at room and cryogenic temperature (magnetic and XRD measurements), we focus on elucidating whether the shift of the superconducting transition is achieved without increasing the T_c-inhomogeneities and also on studying the superconducting fluctuations in such hybrids. We conclude that they open a way to tailor the stress and T_c of HTS, without producing extra T_c inhomogeneities, and that the superconducting fluctuations are not visibly altered by the piezostress.

6.1 Introduction

The effect of the strain in the properties of High Temperature Superconductors (HTS) has been a research subject of interest since shortly thereafter the discovery of these materials, as they could be important to understand the mechanism of HTS. [123–133] These compounds are layered materials, and their superconducting properties change significantly depending on the applied pressure. [123–133]

The uniaxial pressure experiments are useful to separate the contributions from each axis compression. It is well known that a compression in the CuO_2 in-plane direction enhances the critical temperature, while the uniaxial pressure in the out-of-plane direction decreases it. [123, 125, 126] Therefore, the effect of the pressure is different depending on the crystallographic axis. Note that the uniaxial pressure experiments are limited by the pressure that the HTS is able to receive without cracking. Hydrostatic pressure experiments are more useful to reach high pressures, of the order of GPa. [123–125] Under these conditions, the critical temperature increases with pressure to reach a maximum, and then it starts to decrease again with pressure. [123–125] Some phenomenological proposed that the change of the critical temperature could be understood as a change in the doping, that leads to a movement in the phase diagram of HTS. [123, 134]

Other way to study the effect of the strain in the superconducting properties is to grow HTS films over substrates with different lattice parameters. [127–129] The lattice mismatch between the HTS film and the substrate induces a biaxial strain in the film, that changes the superconducting properties of the sample. For instance, Locquet et al. doubled the LSCO critical temperature using a substrate with an in-plane lattice parameter that compresses the HTS film. [127] However, this method has also some drawbacks when used to compare the superconducting properties as a function of stress, because in order to vary strain a new (and then different) sample has to be grown for each strain, and also because the stress is not continuously variable. [127–129]

To address this problem, it has been proposed to use a piezoelectric substrate to study the effect of different strains in HTS films without using different samples. [130–133] This method also allows to study how the superconducting properties change under expansion and compression, by applying positive or negative piezovoltages. It also enables to compress the copper-oxide planes at the same time as expanding the out of plane direction, optimizing the T_c variation.

In the experimental works [130–133] the group of Professor Hühne in Dresden have grown several of such piezoelectric+superconducting devices and measured in them quantities such as the resistive transition and X-ray diffractogram at room temperatures. In this chapter, we present study in which we focus mainly on two aspects not fully addressed by previous pioneering works: First, we try to elucidate whether the shift of the superconducting transition due to piezostress is accompanied by a change of the T_c disorder distributions. Secondly, we also study the superconducting fluctuations on such hybrid systems.

For that aim, we will employ hybrid piezoelectric high-temperature superconducting films grown in our group in Santiago[1]; in Section 6.2 we briefly summarize the fabrication of such films, in which the piezoelectric that has been used is $Pb(Mg_{1/3}Nb_{2/3})_{0.72}Ti_{0.28}O_3$ (PMN-PT) and the superconductor is a $\sim$100 nm layer of $YBa_2Cu_3O_{6.9}$ (YBCO). Then, we have performed basic characterization measurements of such films by means of XRD, magnetization and resistivity measurements, under no piezostress, (Section 6.3) and under different piezostresses (Section 6.4).

In Section 6.5 we address our main objective in this chapter, *i.e.*, to discuss the resistive transition of these hybrids as a function of the piezostress. First, we show that the width and shape of the transition itself is not altered by the piezostress except for a shift in the temperature. Secondly, we show that the width and shape of the transition itself is not altered by piezostress except for a shift in the temperature. Secondly, we show that the superconducting fluctuations above the transition can be understood, for all the studied piezostresses, in terms of the Ginzburg-Landau-like models for paraconductivity fluctuations, indicating then that piezostress changes the critical temperature of the transition but not the excitation energy responsible of superconducting fluctuations. Finally, in Section 6.6 we summarize our findings and conclusions.

6.2 Sample preparation

The c-axis oriented YBCO thin films were grown by professor J. A. Veira in our research group in Santiago de Compostela, using a DC cathodic sputtering device. The substrates are (001) PMN-PT monocrystals (TRS Technologies). The superconducting bulk employed as sputtering target was $YBa_2Cu_3O_x$ ($6.4 < x < 7$) with a purity of 99.999% (commercially provided by Superconductive Components, Inc.). During deposition, by dc sputtering with an on-axis cathode-substrate configuration, the substrate is held at 750 °C in a flow of oxygen at partial pressure of 0.3 Torr and a flow of argon with a total pressure of 0.75 Torr. The applied discharge current is 240 mA at 370 V and the distance between cathode and substrate is 3 mm. Under these conditions, films with a thickness of about 120 nm were grown within 2 h. After deposition, the film is cooled down at a rate of 70 °C min^{-1} down to 600 °C while the oxygen pressure increases up to 500 Torr, being maintained at this temperature and pressure for 30 min.

In order to be able to apply a transversal voltage to the piezoelectric su-

---

[1] These films were grown by Professor J.A. Veira of our research group. The subsequent sample measurements were done by the author (help is acknowledged to M. Martínez, A. R. Álvarez, J. Mosqueira and J.A. Veira).

perconducting hybrid, and also to measure its in-plane electrical resistivity, we deposited metallic electrical contact pads. In particular, by using a HLT 150 Balzers thermal evaporation system.

We first deposited a layer of gold of thickness about 200 nm in the bottom of the film (the free surface of the piezosubstrate). Then, in the opposite surface (on top of the YBCO) we deposited 4 parallel gold bands, of similar thickness and 1 mm width, using the same evaporation device and an ad-hock mask. The upper contacts will be used fot resistivity measurements in 4-probe configuration; The piezovoltage will be (simultaneously, if needed) applied between the bottom contact and one of the middle upper bands. For that, we bond copper wires of diameter about 0.2 mm pasting them using a silver-based epoxy that is conductive at cryogenic temperatures. These wires are welded to the sample holder, that has an space to incorporate a platinum thermometer.

Magnetic susceptibility measurements were done before the deposition of the electrical contacts, to avoid their magnetic signal. XRD measurements under no piezovoltage were also done before deposition (and confirmed afterwards).

6.3 Characterization under no piezostress

6.3.1 XRD measurements

We have characterized the quality of YBCO films grown on PMN-PT with different techniques. First of all, we have measured the x-ray diffraction (XRD) patterns of our samples to analyze if they were correctly grown in the c-axis direction. These measurements were performed with a PANalytical's Empyrean diffractometer, equipped with a 5-axes goniometer and an area detector PIXcel^{3D}. The radiation used for the measurement has wavelength $\lambda(K_{\alpha 1}) = 1.5406\,\text{Å}$ obtained from a sealed Cu tube and a hybrid 2-bounce Ge(220) monochromator. The angular region used for the measurement is between $20° < 2\theta < 90°$with a step of $0.02\,\text{s}^{-1}$ and accumulating a time of 2 s per step.

The results of the measurements are plotted in Figure 6.1, in which it is possible to check that both the substrate and the thin film peaks correspond to crystallographic indexes in the c-direction, and therefore we can conclude that the film is oriented in the desired position. These measurements also lead us to obtain the c-axis lattice parameter of both the YBCO and the PMN-PT. The lattice parameter obtained for YBCO is $c = 11.68\,\text{Å}$, and for PMN-PT is $c = 4.02\,\text{Å}$. It is important to remark that these lattice parameters have been measured before any polarization procedure (application of transversal voltage) was done over the sample.

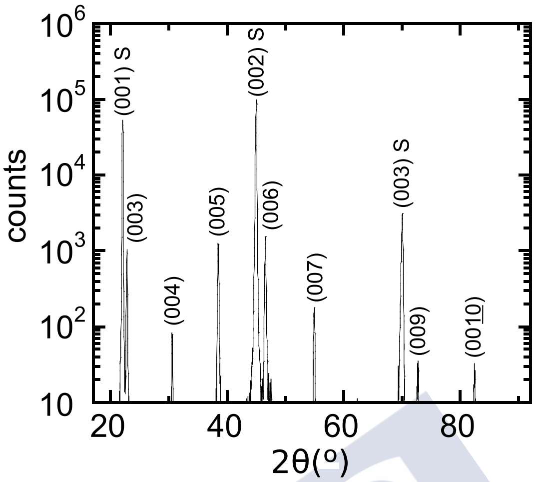

Figure 6.1: In this figure we show the XRD diffractogram of one of our YBCO+PMN-PT hybrids. The substrate (PMN-PT) peaks are marked with an S, whereas the YBCO ones are marked with only the corresponding crystallographic indexes.

6.3.2 Susceptibility measurements

The macroscopic superconducting critical temperature and the distribution of critical temperatures in our samples, without any transversal piezovoltage, can be obtained from the magnetic susceptibility χ of the superconducting films, following standard procedures our group used and described in detail, *e.g.*, in References [103, 135]. We have measured the susceptibility using a Quantum Design's MPMS-XL magnetometer, that achieves enough sensitivity as to perform this kind of measurements in thin films.

The procedure is based on the measurement of the magnetic moment of the sample when it is under a dc magnetic field applied in the out of plane direction following a zero-field-cooled procedure. The nominal magnetic fields used to measure the magnetic moment of different samples are between 3 and 3.3 Oe.

Because the substrate value of the magnetic susceptibility χ is so much larger in the superconducting state (where $\chi \simeq -1$) than in the normal state (where $|\chi| \sim 10^{-5}$), and χ being an extensive quantity, the value $|\chi(T)|$ directly reports the fraction of the sample that has become superconducting at that temperature T. Therefore, the $d\chi/dT$ near the transition is an excellent approximation to the distribution of local T_c values in the sample, $\omega(T_c)$. [103, 135, 136]

Susceptibility measurements in two examples of our YBCO+PMN-PT hybrids are plotted in Figure 6.2 and its insets. The criteria that we have used to fix the critical temperature of each sample is taking the maximum of the Gaussian fit to the solid lines in $d\chi/dT$ peak at the transition. These derivatives and the fits are plotted in Figure 6.2.

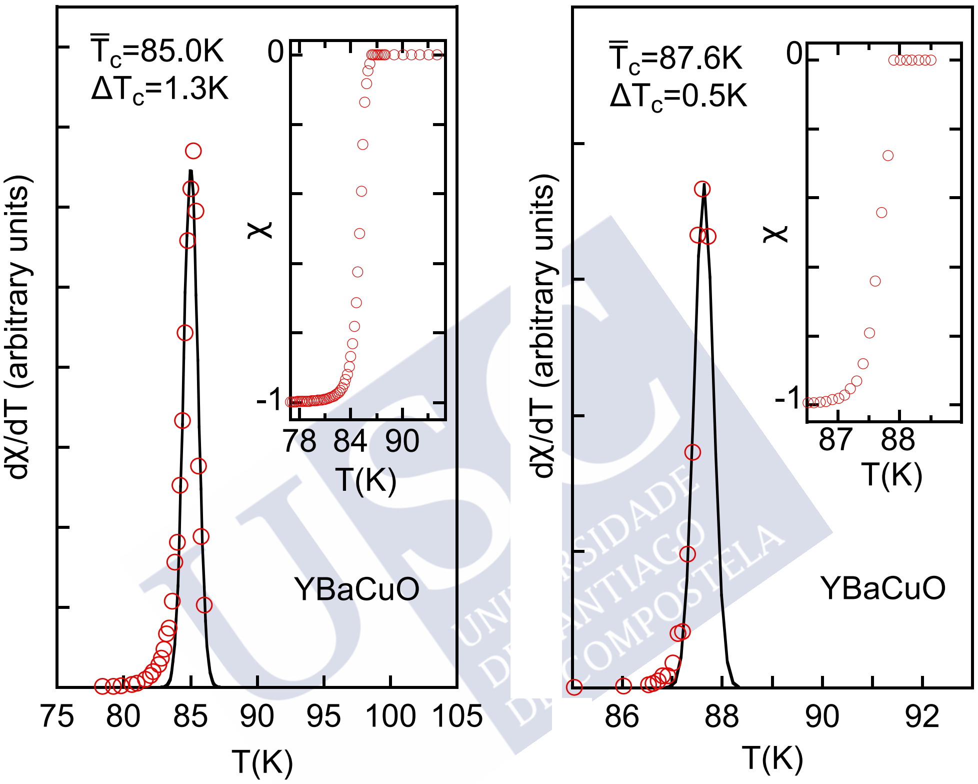

Figure 6.2: In this figure we show two SQUID measurements of the susceptibility for two samples of our YBCO+PMN-PT hybrid. The main figures show the derivative of the susceptibility, that may be identified to the T_c distribution, $\omega(T_c)$, of the film. We have also plotted, in the insets, the value of the susceptibility (in SI units) in function of the temperature for these samples. The data have been fitted by a Gaussian function, which maximum may be interpreted as the average of the critical temperature of the film $\overline{T}_c$, and the Full Width at Half Maximum (FWHM, ΔT_c) as a measure of the inhomogeneity.

These $d\chi/dT$ peaks indicate that the quality of the films grown in our laboratory is optimal in terms of the transition width and in terms of the homogeneity of T_c, as they shows transition widths (ΔT_c, taken as the FWHM of the Gaussian

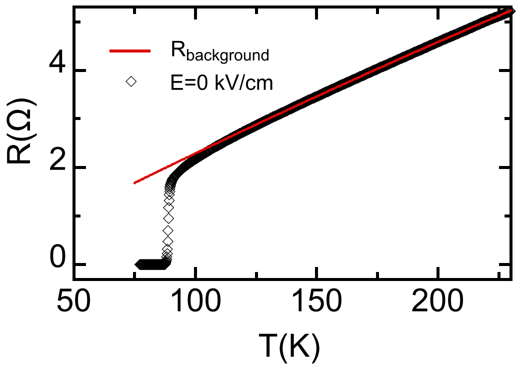

Figure 6.3: In this Figure resistance measurements obtained for a YBCO thin film are plotted with the normal state background. The black rhombs represent the data obtained for $E = 0\,\mathrm{kVcm}$ and the red line is the background Resistance $R_{\mathrm{background}}$. A zoom near the transition may be seen in Figure 6.8 (rhomb data again).

peaks) between 0.5 and 1.3 K. Moreover, the critical temperatures shows that our samples are near the optimal doping, where $T_c \sim 90\,\mathrm{K}$.

6.3.3 Resistivity measurements

Another way to study the quality of the superconducting YBCO films is to analyze the resistance curves versus temperature in a wide range of temperatures.

We have measured the electrical resistance of our films with the four-probe method, with a current bias of 0.9 mA. To achieve the cryogenic temperatures we have used a cryostat to measure with a very low temperature rate of change, measuring the resistance applying opposite currents at each temperature, to calculate the mean value with the aim of eliminating possible thermoelectric effects.

In Figure 6.3 we show an example of resistance curve measured in one of our hybrid devices, taken without any polarization of the piezosubstrate (no voltage between any of the upper contacts and the one at the bottom of the piezosubstrate). The curve shows an inflexion-point critical temperature of about 88.9 K, a value near the one expected for optimal doping in YBCO films of similar thickness in $SrTiO_3$ substrates. The transition width is $\Delta T \sim 1\,\mathrm{K}$, which stands for a very good film quality. The normal-state resistance $R_{\mathrm{background}}$ follows a polynomial function, as is also plotted in the Figure 6.3.

6.4 XRD measurements of the strain under different piezostresses

As it has commented in the introduction, the inverse piezoelectric effect enables us to change the lattice parameters of the sample by applying an electric field. To study this change, we have measured the strain ε defined as:

$$\varepsilon_{\mathrm{c}} = \frac{c(E) - c(E=0)}{c(E=0)}, \tag{6.1}$$

where E is the applied electric field applied transversally (along the out of plane or c-direction) to the piezosubstrate and c is the out-of plane lattice parameter.

For these measurements we have used a Rigaku Miniflex II diffractometer. The radiation used for the measurement has a wavelength $\lambda(K_{\alpha 1}) = 1.5406\mathring{A}$ obtained from a sealed Cu tube. In this case we don't have the monocromator, so that the radiation has also contributions $\lambda(K_{\alpha 2}) = 1.5443\,\text{Å}$, and $\lambda(K_{\beta}) = 1.3920\,\text{Å}$respectively, with an intensity of $0.5\,I$ and $0.05\,I$, where I is the intensity of the $K_{\alpha 1}$ radiation. Because of the proximity of $\lambda(K_{\alpha 1})$ and $\lambda(K_{\alpha 2})$, the peaks they produce overlap each other; we remove this K_{α_2} contribution from our data using the commercial software PDXL which uses the Rachinger method. The data treatment also includes an smoothing (that is performed optimizing the B-spline function to the measured data using the least-squares method) and a background substraction (obtained using the Sonneveld-Visser method). The angular region used for the measurement fixed a step of $0.02\,\mathrm{s}^{-1}$ and accumulating a time of 2 s per step.

6.4.1 Comparison between the strains in the piezosubstrate and in the superconductor

In the Figure 6.4 we show the movement of the (003) peak of a PMN-PT and the (005) peak of YBCO for an applied electric field of 10 kV/cm at room temperature. Note that (as we describe in more detail in the next section) the values of the properties of related to the hybrid compound (strain, resistance, magnetization, etc.) depend highly on the history of the sample, because of the hysteresis of the inverse piezoelectric effect. [137–143] Here we have plotted the peaks obtained after polarizing the sample with 10 kV/cm, taking the first measurement at 0 kV/cm and then increasing the electric field up to 10 kV/cm.

By applying Bragg's law to the location othe maximums of these peaks, we obtain the corresponding ε_c by applying Equation 6.1. What we can infer from the measurements is that only a about 10% of the strain is transmitted to the YBCO film in the c-direction. It is important to remark that the direct transmission of strain is in the ab-plane, and this strain induces an strain in the c-direction, which is always lower than the strain in the ab-plane, due to the Poisson coefficient of the material.

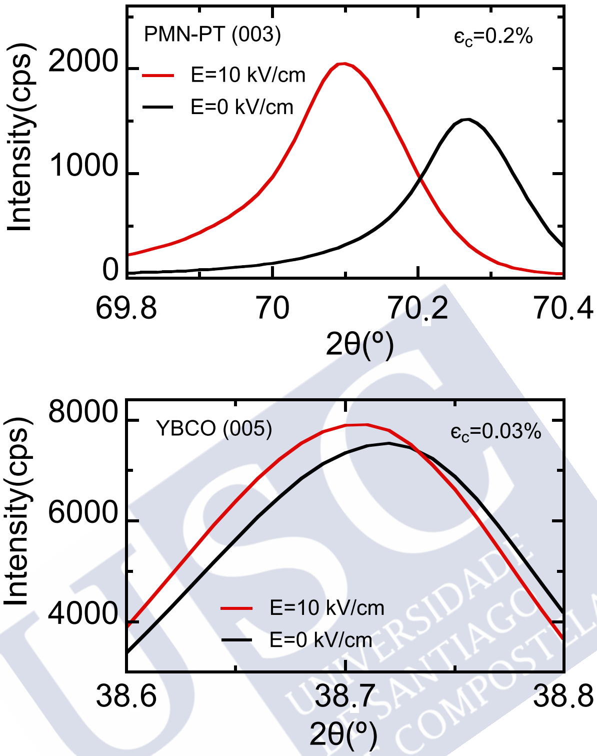

Figure 6.4: The top figure shows the (003) Bragg peak of the PMN-PT XRD spectra in one of our piezodevices, when two different piezovoltages are applied to the sample corresponding to transversal electrical fields $E = 0$ and $10\,\mathrm{kV/cm}$. The bottom figure shows the (005) peak of YBCO for the same electric fields and sample. All these measurements have been taken at room temperature. In both cases the measurements at $E = 0\,\mathrm{kV/cm}$ were obtained after poling the sample during 30 minutes at $10\,\mathrm{kV/cm}$, and the other values after the direct increase of the electric field after the first measurement.

6.4.2 Temperature and hysteresis effects

An interesting point to be made is the fact that the inverse piezoelectric effect in our devices, and thus the piezostress, displays at room temperature hysteresis behavior, while at cryogenic temperature the effect is instead reversible and almost linear. This behavior could be in fact expected already from earlier measurements as a function of temperature of the coercive field of PMN-PT. [137] We measured such behavior by means of XRD measurements under different piezovoltages and under different temperatures, including cryogenic ones. For that, we built a cryogenic module that we incorporated to the same Rigaku Miniflex II device described before. The module also allows application of the piezovoltage. Teh so-obtained ε_c strains (as given by Equation 6.1 using the displacement of the (003) PMN-PT peak) are plotted in Figures 6.5 and 6.6, for room temperature and 162 K respectively. These figures evidence the markedly different behavior at room and cryogenic temperatures.

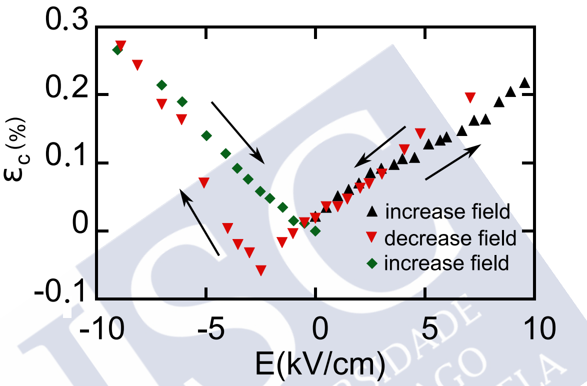

Figure 6.5: The hysteresis loop represented in this plot was obtained by measuring the (003) PMN-PT Bragg peak (in the same sample as in Figure 6.4) at room temperature. We start the measurement after poling the sample during 30 minutes, and then we measure the value at 0 kV/cm. Then we start to increase the transversal electric field, showing the data obtained using the black upwards triangles. We rise then the electric field up to 15 kV/cm and then we start to decrease it up to −15 kV/cm (red downwards triangles). Finally we increase again the electric field up to 0 kV/cm (green diamonds). To calculate the value of the strain ε_c, we have taken as a reference the last value of the lattice parameter that has been measured in this hysteresis loop at 0 kV/cm.

First of all, at cryogenic temperatures, as shown in Figure 6.6, the strain of the substrate depends highly on the history of the sample. This is due to the fact that at room temperature, the coercive field of the PMN-PT only about 1.5 kV/cm [137]. Below the coercive field, the response of the PMN-PT is linear and reversible, which means that there is no hysteresis. This is due to the fact that the electric field affects directly to the polarization of the unit cells, and does not change the orientation of the polarization domains of the sample. [142, 143] When this domains change their orientation, the substrate response is no longer

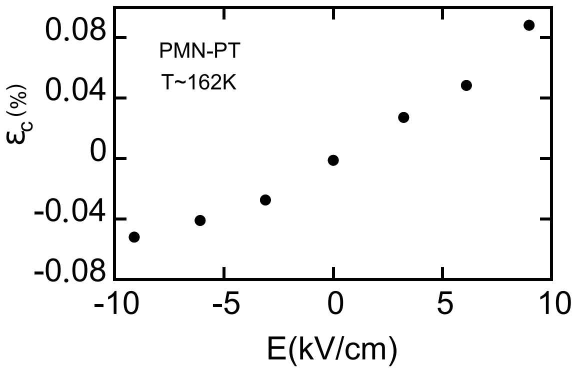

Figure 6.6: Effect of the transversal electric field over the ε of the PMN-PT at a temperature of 162 K. This measurement demonstrates that the coercive field is increased at cryogenic temperatures, and thus the linear region of the system is also increased. This lead us to obtain expansion or compression in the sample applying positive or negative electric fields, respectively. Also, hysteresis is not seen during these measurements, that are reproducible when increasing or decreasing E within this range (in contrast to the situation at room temperatures, see Figure 6.5).

reversible and depends on the history of the system. As shown in Figure 6.5 we have measured the strain of the c-axis parameter of the PMN-PT at room temperature for applied electric fields between 15 to -15 kV/cm starting from 0 kV/cm to 15, achieving the so-called butterfly piezoloop, as studied in general, *e.g.*, in References [138, 143].

In contrast, at cryogenic temepreatures the coercive field is well higher. [137] Therefore, we can apply high electric fields (at least to 10 kV/cm) without entering in the hysteresis loop. This lead us to obtain more reproducible measurements, and to obtain expansion and compression for positive and negative applied electric fields, respectively. Our results in Figure 6.5 also show that the effect is not exactly symmetric. This is, we can obtain higher strain with positive electric fields than with negative ones. This is a similar result to the one obtained in Reference [137] at 90 K for PMN-PT monocrystals.

6.5 Electrical resistivity measurements under different piezostresses

To measure the resistance of the YBCO layer under different stresses exerted by the piezosubstrate, we have used the same experimental setup as we described in

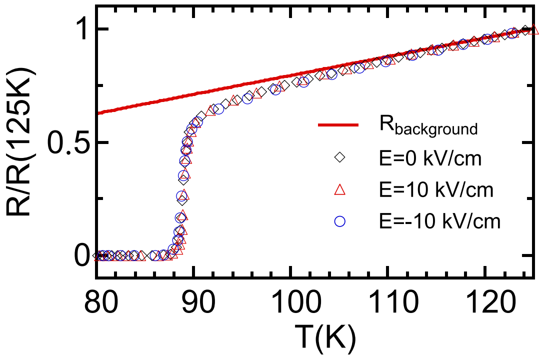

Figure 6.7: In this graph it is shown the experimental data obtained for the resistance curves for the three applied electric fields plus the background polynomial curve obtained from the normal state data. The black diamonds represent the data obtained for $E = 0\,\mathrm{kVcm}$, the red triangles represent the data for $E = 10\,\mathrm{kV/cm}$, the blue circles are the data obtained for $E = -10\,\mathrm{kV/cm}$, and the red line is the background Resistance $R_{\text{background}}$.

Subsection 6.3.3, *i.e.*, we measure in a 4-wire configuration the in-plane resistance of the YBCO layer. The piezovoltage is applied between the bottom contact in the piezoelectric and one of the voltage contacts in the upper side of the YBCO film. The protocol for the application of the piezovoltage is as follows: First of all, we polarize the system at room temperature during 30 minutes with a piezovoltage of 300 V. After this, we decrease the temperature until 77 K, where we apply the desired piezovoltage for the measurement during another 30 minutes at stable temperature. Finally we increase the temperature slowly up to room temperature with the applied piezovoltage to measure the resistivity.

6.5.1 Shift of the resistive transition with piezostress

Our measurements for the YBCO resistivity measured under different electrical fields E applied to the piezoelectric are plotted in Figures 6.7 and 6.8. The first Figure shows an overview with respect to temperature and also the same normal-state background $R_{\text{background}}$ already used previously in Section 6.3.3 and Figure 6.3 and that, as shown by Figure 6.7, is valid for the three electrical fields E.

In Figure 6.8, we zoom the T-region near the superconducting transition. This figure clearly evidences that, contrarily to the normal-state background, the critical temperature is significantly shifted by the piezostress. In particular, a first account of this shift may be quantified through the inflexion temperature in the middle of the transition, that for no piezovoltage is $T_{ci} = 88.93\,\mathrm{K}$, while for

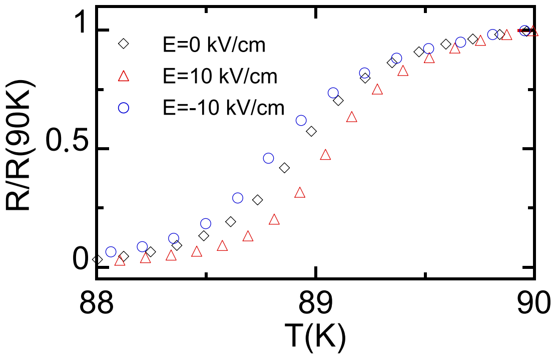

Figure 6.8: Zoom of the resistance transition of the hybrid compound YBCO+PMN-PT for different electric fields. The black diamonds represent the data obtained for $E = 0\,\mathrm{kVcm}$, the red triangles represent the data for $E = 10\,\mathrm{kV/cm}$, and the blue circles are the data obtained for $E = -10\,\mathrm{kV/cm}$.

$E = 10\,\mathrm{kV/cm}$ is $T_{ci} = 89.07\,\mathrm{K}$ and for $E = -10\,\mathrm{kV/cm}$ is $T_{ci} = 88.83\,\mathrm{K}$. The positive electric fields corresponds to the case in which the c lattice parameter of the PMN-PT is expanded, so the in plane lattice parameter of both the PMN-PT and the YBCO is compressed, and thus the c-axis parameter of the YBCO is expanded. This leads to an increase of the critical temperature. Conversely, with negative electric field, the c-axis lattice parameter of the YBCO is decreased, and the critical temperature is also diminished.

When combined with our measurements of the piezostress as a function of the piezovoltage, *i.e.*, our data of Figure 6.6, our resistivity measurements provide a value of the variation of T_{ci} with respect to the c-axis of $dT_{ci}/d\varepsilon_c = 2.6\,\mathrm{K}$.

6.5.2 Paraconductivity

The shift of the critical temperature with piezostress indicates a change of the fundamental-state energies that determine the appearance of superconductivity. It would be interesting, however, to test whether also the excitations above that groundstate are affected by piezostress. A common related experimental probe is the so-called paraconductivity or fluctuation-induced electrical conductivity, *i.e.*, the rounding of the resistivity transition, or the difference, in conductivity units, between the measured resistance near but above T_c and $R_{\mathrm{background}}$. In Section 4.2.3 we have written down a definition formula for the paraconductivity $\Delta\sigma$ (Equation 4.7) and we also detailed different equation predictions (Equation 4.8) for $\Delta\sigma$ as a function of the reduced temperature $\ln(T/T_c)$ obtained on the grounds of Ginzburg-Landau approaches with Gaussian fluctuation thermodynamic theories. The comparison of our data with such predictions also open a way to probe

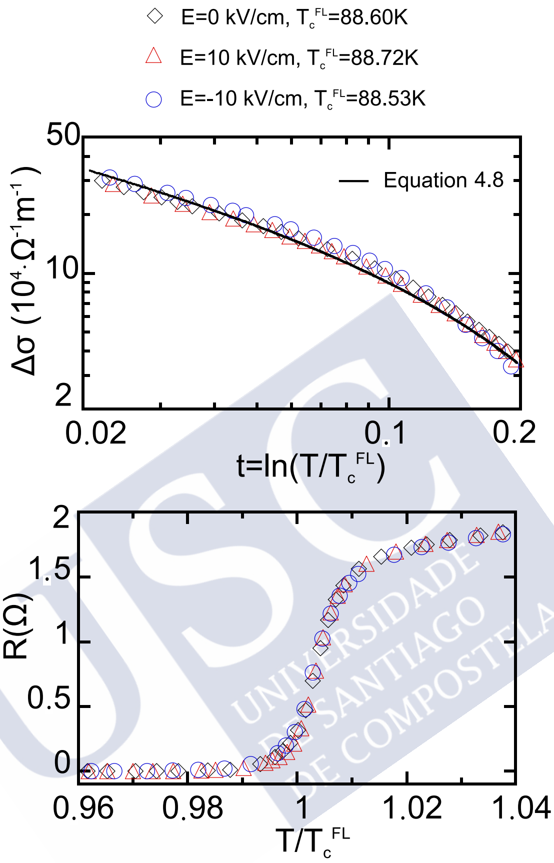

Figure 6.9: In the upper part of the Figure it is shown the representation of the data obtained for the paraconductivity for the three resistance transitions measured for three different electric fields. The fit to the paraconductivity equation 4.8 is also plotted as a black line. In the lower part of the graph, it is shown the experimental measurements in terms of T/T_c^{FL}, being T_c^{FL} the value of the critical temperature obtained for each fit to the paraconductivity equation. In both parts of the graph, the black diamonds represent the data obtained for $E = 0\,\mathrm{kVcm}$, the red triangles represent the data for $E = 10\,\mathrm{kV/cm}$, and the blue circles are the data obtained for $E = -10\,\mathrm{kV/cm}$.

the dependence of T_c with the piezoelectrical field E and piezostress ε_c maybe more accurate than the simple analysis of the inflection point temperature T_{ci} alone.

For that purpose, we have obtained $\Delta\sigma$ from our measurements with different E values. The results are plotted in the upper panel of Figure 6.9, together with the best fit to the Gaussian-Ginzburg-Landau approach (Equation 4.7) using the well accepted parameter values for optimally-doped YBCO [99,100] $\xi_c(0) = 1.1\,\text{Å}$, $d = 5.85\,\text{Å}$, and $c = 0.7$, the only free parameter being the critical temperature itself. The so-obtained critical temperature is called henceforth (and also in our Figures) T_c^{FL}. As evidenced in Figure 6.9, it is possible to obtain excellent agreement between this theoretical approach and our data at least in the range $0.02 < \ln(T/T_c^{\text{FL}}) < 0.2$ (corresponding to a T-range of about 18 K).

In fact, a notable point evidenced by such paraconductivity analysis is that the data for different E collapse in a single common $\Delta\sigma$ vs $\ln(T/T_c^{\text{FL}})$ curve. This indicates that piezostress does not alter the nature of the excitations in the system behind paraconductivity.

Note that T_c^{FL} (see Figure 6.9) is slightly below T_{ci} in all our measurements. By combining these values with strain measurements (Figure 6.6) we obtain $dT_c^{\text{FL}}/d\varepsilon_c = 2.1\,\text{K}$ (to be compared to $dT_{ci}/d\varepsilon_c = 2.6\,\text{K}$).

It may be interesting to probe whether the superconducting fluctuations remain universal with respect to T_c^{FL}, for different values of E also outside of the temperature range $0.02 < \ln(T/T_c^{\text{FL}}) < 0.2$. As already commented on in Section 4.2, outside of this window simple Gaussian approaches are no longer applicable.

However, an effective way to check this aspect is to simply plot R versus T/T_c^{FL}. This is done in the lower panel of Figure 6.9, that shows that normalization of temperature as T/T_c^{FL} transforms all the resistivity transition in universal curves (*i.e.*, all curves for different E values collapse in a common shape). This indicates that also close to T_c the superconducting fluctuations only change with E in the shift of the T_c^{FL} value (the same analysis could be also extended to the high temperature region, $\ln(T/T_c\text{FL}) > 0.2$, but we feel that our experimental uncertainties, *i.e.*, the dispersion of the data points, does not allow to draw reliable conclusions).

6.6 Conclusions

By using YBCO thin films of very good quality grown over PMN-PT substrates, and we have characterized the transition of the superconducting layer through resistance measurements and through magnetic susceptibility measurements.

Moreover, we have studied the room temperature properties of the inverse piezoelectric effect of the PMN-PT through x-ray measurements for different applied fields. The transmission of the strain to the YBCO film has also been studied at room temperature. The c axis parameter dependence of the electric field for the PMN-PT has also been studied for cryogenic temperatures, showing a different, reversible behavior in relation to room temperatures.

We have analyzed the paraconductivity of the resistance measurements for three different electric fields, showing that the superconducting fluctuations above the critical temperature can be well explained using the equation 4.8 and leaving T_c^{FL} as the only free parameter. Moreover, it is also clear that the effect of the electric field can be explained just as a temperature shift in the whole transition.

USC
UNIVERSIDADE
DE SANTIAGO
DE COMPOSTELA

IIB: ELECTROSTATIC NANOSTRUCTURED MICROPOROUS MEDIA FOR NANOFLUID FILTRATION

The contents in this part are based on an article by J.C. Verde et al. under consideration for publication in Physical Review E. Most of the computations presented in this Part IIB have been done with the software NanoF-SimTool developed in our laboratory to simulate nanofiltration using ENM media. This product, through the Technology Transfer and Entrepreneurship Office of our University, is registered software (code 03/2016/1356 date 17 Nov 2016) and was licensed to the filtration company ASB, SL.


USC
UNIVERSIDADE
DE SANTIAGO
DE COMPOSTELA

Chapter 7

Electrostatic nanostructured microporous (ENM) media: Overview of theory and computational methods

Summary of the chapter:

We present and adapt the main theory tools that we shall use in our studies of the influence of microgeometry over the nanofiltration characteristics of electrostatic-nanostructured microporous (ENM) media. First, the governing equations for the process of successive impurity trapping in ENM media are presented, based on previous work of our research group in Santiago (effective-charge model). Then, we adapt these model equations to the case of interest in our present work, *i.e.*, we update these equations to account for possible variations of the radius of the microconduits along a finite length. We also bring them into a finite-difference form, so to allow their computational implementation. Other simulation details, including also typical parameter values in actual ENM media introduced by academia and industry, are also provided.

7.1 Introduction

One of the most innovative and promising techniques for water filtration is the application of nanotechnology. For example, in recent years both academia and industry [51–60] have become progressively interested in filtering media and membranes that achieve nanofiltration (*i.e.*, removal of impurities of size $\lesssim 20\,\mathrm{nm}$) by means of nanofunctionalization of the inner walls of pores of diameters in the micrometric ~ 0.2–$2\,\mu\mathrm{m}$ (such micrometric pores are somewhat counterintuitively called *macropores* in IUPAC terminology [144]). In these investigations [51–60] it has been revealed the surprisingly good capability of such media to filter out nanosized impurities from an aqueous solution, principally when the signs of the ζ-potentials of impurities and functionalized pore walls are opposite and electrostatic effects enhance the filtration. This is in spite of the relatively large diameter of the pores (note that for a pressure-driven flow passing through a cylindrical conduit with diameter $1\,\mu\mathrm{m}$, only about 0.04% of the fluid will transit closer than 10 nm from the walls). A key practical advantage of these novel ENM is that they are not affected by the very large hydrodynamic resistance of the media composed by pores of nanometric diameter. In fact, industry has already commercialized some of those nanoenhanced filters, [58–60] not only for drinking water purification but also for other applications (clinical analyses, industrial effluent treatment, etc.).

It is currently possible to custom-engineer the geometry profiles of micrometric-diameter pores of filtering media and membranes (see, *e.g.*, References [145–149] for a description of different ad-hoc geometries and the experimental techniques used to obtain them). These feasible designs include, among others, tubular conduits with cylindrical shapes having different diameters, [146] corrugated conduits, [145] or pores with cone-like shapes. [147–149] Investigating conduits with different nominal geometries may also be relevant for random media, in which interconnections and throats between pores may be appropriately studied in terms of conduits with sinus-like corrugated shapes. [150–153]

However, no investigation seems to exist up to now of the influence over the nanofiltration characteristics of the nominal conduit geometry of ENM. For that purpose, in part IIB of the present thesis we will present numerical simulations (and also some analytical results) of the nanofiltration performance and operational lifetime of nanoenhanced micropores with different geometries. The governing equations used for our numerical simulations will be taken from a recent model [61] describing the trapping of nanoimpurities by analogous electrostatic inner walls in a short cylindrical conduit. We rewrite these equations into a finite-difference form, enabling them to be used in the computational assessment of conduits of finite length and arbitrary variations of radius (and therefore allow to study conduits of different microgeometry). The model in [61] may be also related to the so-called lubrication model independently developed in a different context (electrophoresis) by Ghosal in [154–156] (see also Section 7.2.1).

The present chapter is organized as follows: in Sections 7.2.1 to 7.2.3 we introduce the model and governing equations of [61] in a finite-difference version appropriate for numerical treatment. Sections 7.2.4 and 7.2.5 describe our computational methods and the parameter values used in the simulations. The application of these methods to different specific conduit geometries is deferred to Chapter 8.

7.2 Model equations

7.2.1 Initial considerations

We consider a tubular conduit of micrometric diameter whose inner walls have a (initially homogeneous) nanotexture. The tube has a nominal diameter $d(x)$ that may, in general, vary along the axial coordinate x (with $0 \leq x \leq L$, where L is the tube length). A fluid passes through, carrying a certain concentration of nanoimpurities to be filtered out. All of the impurities are taken to be equal and have average radius ρ_0. Our task is to obtain the evolution with space x and time t of the impurity concentration $C_{\mathrm{imp}}(x,t)$ in the fluid, and of the areal density of impurities $n(x,t)$ trapped in the tubes (throughout this article, by "areal density" we refer to quantities normalized using the nominal area of the tube inner wall).

Initially ($t = 0$) the system is in the "clean state", in which $n(x,0) = 0$ and the diameter available to the flow is $d(x)$. As time and flow passes, impurities get trapped and progressively cover the tube inner walls. Eventually, a "saturated state" is reached in which the nanotexture of the walls no longer electrostatically attracts further impurities. In the saturated state, n is n_{sat} and the diameter available to the flow decreases down to a value $d(x_i) - \delta_{\mathrm{sat}}$. We will consider in this article that after this saturated state the impurity trapping capability of the walls (and hence the filtration performance) is zero, so that we focus only on the effects of nanostructuring and neglect conventional filtration mechanisms.

In order to evaluate the effects of variations of the diameter along the tube's axial coordinate, and also to allow computation of successive spacial and temporal finite-difference iterations, we discretize the problem as follows: We divide the tube into $i = 0, 1, \ldots N$ parallel slices of coordinates $x_i = (L/N)i$ and also discretize time as $t_{j+1} = t_j + \Delta t_j$ with $j = 0, 1, \ldots$ (the reason to allow the timestep to vary with j will be to optimize our computational algorithms, see Section 7.2.4).

Let us now briefly describe the key ingredients of the model introduced in [61] for the impurity-trapping dynamics of the nanostructured conduits, focusing mainly on its adaptation to the finite-difference formalism needed for our present purposes (see [61] itself for a more comprehensive discussion of the underlying basic aspects of the model):

i) The starting point of model [61] is to consider the effects of electrostatic attraction on the probability of collision between the impurities circulating in the liquid flow and the conduit walls. For that, it introduces an "effective charge" of the walls (proportional to their ζ-potential) that will decay as impurities cover them and screen out the charges exposed in the nanotexturing. It is then calculated the "collision distance" $\rho_{\rm e}$, or typical impurity-wall separation below which an impurity in the flow will acquire course of inevitable collision with the wall. From simple electrostatic escape-distance estimates, it may be expected that $\rho_{\rm e}$ should grow roughly linearly with $z_{\rm e}$. [61] When also taking into account the effects of screening due to the Debye length of the fluid $\lambda_{\rm D}$, a more precise law is obtained: [61]

$$\rho_{\rm e}(x_{\rm i},t_{\rm j}) = \rho_0 + \lambda_{\rm D}\, W\left(\frac{\rho_{\rm e0}-\rho_0}{\lambda_{\rm D}}\left(1-\left\|\frac{n(x_{\rm i},t_{\rm j})}{n_{\rm sat}}\right\|\right)\exp\left(\frac{\rho_{\rm e0}-\rho_0}{\lambda_{\rm D}}\right)\right)\,, \tag{7.1}$$

where $\rho_{\rm e0}$ is the collision distance in the clean state, $W(x)$ is the the principal Lambert function and the notation $\|x\|$ stands for $\min(1,x)$.

ii) Secondly, the model [61] assigns a impurity-wall binding probability for the impurities that do collide with the walls. This has to linearly decrease with the number of binding centers in the nanotextured walls, *i.e.*, with $n(x,t)$. Therefore, it is maximum in the clean state. It is possibly noteworthy to note here that, when adapting the equations in [61] to a finite-difference treatment, the survival probabilities for x-slices of finite thickness accumulate over length multiplicatively, not linearly as considered for differential x-lengths in [61]. So, the binding probability for the clean state Ω_0 in [61] has to be replaced by $\Omega_0^{\rm finite} = (N/L)[1-(1-\rho_0\Omega_0)^{L/\rho_0 N}]$. As expected, for $N\to\infty$ this recovers probabilities linear with length. In all the simulations performed in our present work, N is as large as 10^6 and the differences between $\Omega_0^{\rm finite}$ and Ω_0 remain below 0.05%. However, for smaller values of N the difference may be relevant.

iii) Finally, model [61] assumes flow conditions realistic for most water filtering applications. This includes moderate flow velocities, for which it is valid to neglect turbulence and the effects of axial advection on the transversal dynamics (see Section 7.2.5 for a more comprehensive discussion of this latter aspect and the implications over the parameter values chosen for the simulations). The model also considers a pressure-driven flow (in contrast to electrical-driven-like in the models proposed by Ghosal in [154–156] for electrophoresis applications). As discussed in detail for instance in [157,158], if the radiuses of the conduits remain $\gtrsim 10\,$nm and with moderate variations in space, the aqueous flows driven by hydrostatic pressure are in the Poiseuille regime. The corresponding velocity profile may be thus used to obtain the fraction $f_{\rm e}$ of impurities that travel within the collision distance ρ_e from the walls:

$$f_\mathrm{e}(x_\mathrm{i}, t_\mathrm{j}) = \left(\left(\left\| \frac{2\rho_\mathrm{e}(x_\mathrm{i}, t_\mathrm{j})}{d(x_\mathrm{i}) - n(x_\mathrm{i}, t_\mathrm{j})\delta_\mathrm{sat}/n_\mathrm{sat}} \right\| - 1 \right)^2 - 1 \right)^2 . \tag{7.2}$$

where ρ_e is again given by Equation (7.1). Therefore, of the impurities that flow through a given slice of the conduit, the fraction f_trapped of them that become trapped by the conduit walls is, in the clean state, the multiplication of $f_\mathrm{e}(x_\mathrm{i}, t_\mathrm{j})$ by Ω_0^finite and by the length of the finite-difference slice L/N. As further flow passes and impurities progressively cover the nanotexture of the walls, the fraction will decrease linearly with the increase of $n(x_i, t_i)$ and become zero when $n = n_\mathrm{sat}$. Therefore its expression becomes

$$f_\mathrm{trapped}(x_\mathrm{i}, t_\mathrm{j}) = \frac{L}{N} \, f_\mathrm{e}(x_\mathrm{i}, t_\mathrm{j}) \, \Omega_0^\mathrm{finite} \left(1 - \left\| \frac{n(x_i, t_i)}{n_\mathrm{sat}} \right\| \right) . \tag{7.3}$$

This allows now to calculate the finite-difference equations for the full filtration dynamics of the nanostructured filter, that are summarized in the following Subsection.

7.2.2 Recursive finite-difference equations for $n(x_i, t_j)$, $C_\mathrm{imp}(x_i, t_j)$ and $\Phi(t_j)$

By using the trapping probabilities discussed in the previous Subsection, finite-difference-iterative expressions may be now obtained for the areal density of trapped impurities $n(x_i, t_j)$ in each x_i slice of the tube at the time t_j, for the concentration of flowing impurities in the liquid flow $C_\mathrm{imp}(x_i, t_j)$, and for the liquid flow $\Phi(t_j)$ passing through the tube. For the areal density of trapped impurities we have:

$$n(x_i, t_{j+1}) = n(x_i, t_j) + \frac{\Delta t_j C_\mathrm{imp}(x_i, t_j) \Phi(t_j) \Omega_0^\mathrm{finite}}{\pi \, d(x_i)} \left(1 - \left\| \frac{n(x_i, t_j)}{n_\mathrm{sat}} \right\| \right) f_\mathrm{e}(x_\mathrm{i}, t_\mathrm{j}). \tag{7.4}$$

The finite-difference expression (but now with the iteration happening in the spatial variable) for the concentration of impurities in the fluid may be also obtained:

$$C_\mathrm{imp}(x_{i+1}, t_j) = C_\mathrm{imp}(x_i, t_j) - \frac{\pi L \; d(x_i)}{N \Delta t_j \Phi(t_j)} \Big(n(x_i, t_j) - n(x_i, t_{j-1}) \Big). \tag{7.5}$$

For the fluid flow $\Phi(t_j)$, as already mentioned above we will assume in this article that the liquid is driven by a constant hydrostatic pressure difference P

between opposite ends of the tubular conduits. We thus use a Poiseuille relationship: [61,154,157]

$$\Phi^{-1}(t_j) = \frac{128\eta L}{\pi P N} \sum_i \left(d(x_i) - \frac{n(x_i, t_j)\, \delta_{\text{sat}}}{n_{\text{sat}}} \right)^{-4}. \tag{7.6}$$

Note that the flow becomes t-dependent even with constant P, due to the progressive narrowing of the conduit as the filter becomes dirtier. Eventually, if $d(x_i) - n(x_i, t_j)\delta_{\text{sat}}/n_{\text{sat}} = 0$ at some x_i, the conduit is clogged and $\Phi = 0$.

7.2.3 Logarithmic removal value LRV and operational lifetimes

As customary, [51–53, 55–59, 159] we will characterize the filtration performance through the so-called "logarithmic removal value":

$$\text{LRV}(t) = -\log_{10} \frac{C_{\text{imp}}(x = L, t)}{C_{\text{imp}}(x = 0, t)}. \tag{7.7}$$

For instance, 99.9% impurity removal corresponds to LRV=3. We will use the notation LRV_0 for $\text{LRV}(t = 0)$. Also, to characterize the endurance of the filter, we define the following two characteristic times: The so-called "LRV≥5 lifetime" and the "LRV≥1 lifetime", defined as the t-values at which the LRV becomes 5-log and 1-log, respectively. In practice, which of these endurance criteria (5-log or 1-log) is more relevant will depend on the specific application intended for the filter.

7.2.4 Computational procedures

Equations (7.4) to (7.6) form a set that may be iterated to compute the x- and t-variation of the characteristics of the filter. For that purpose, the parallel computer LBTS-εpsilon was allocated in full to that task. This computer is composed of about 9000 math coprocessors working in parallel and has 20 Tflops peak computing speed at 32-bit precision (for a more detailed description, see http://lbts.usc.es/epsilon/version2014). The simulations were implemented writing ad-hoc software that accepts arbitrary user-defined geometries for the nominal diameters $d(x)$. It iterates in both the j and i indexes (parallelizing the later), continuously calculating self-adaptively the timesteps Δt_j by requiring that successive instants vary $n(x_{\text{i}}, t_{\text{j}})$ less than 0.01% (for all x_{i} values). This results in about 10^4 time-intervals for each simulation. For the spacial discretization, we divided the tubular conduits into $N = 10^6$ finite-difference slices (this leads in our simulations to a trapping probability for each impurity colliding with the walls always below 10^{-4} per finite-difference x-slice).

For the boundary conditions of our simulations we take as initial state $n(x, 0) = 0$ (*i.e.*, clean state for $t = 0$) and $C_{\mathrm{imp}}(x \neq 0, 0) = 0$. For the spatial boundary condition we take $C_{\mathrm{imp}}(0, t) = C_0$ (*i.e.*, a constant impurity concentration for the fluid at the entry of the tubular conduit).

7.2.5 Typical parameter values

For the various parameters describing the characteristics of the nanofunctionalized macropore conduits in Equations (7.4) to (7.6) we will use values of the same order of magnitude as the ones that were found in [61] to produce good agreement with the available data in various real systems (in particular with those in [51, 52, 58, 59]): We will use a nanoimpurity radius $\rho_0 = 10$ nm, an effective collision distance in the clean state $\rho_{e0} = 30\,\mathrm{nm}$, a binding probability in the clean state $\Omega_0 = 10^{-4}/\,\mathrm{nm}$, a saturation impurity layer thickness $\delta_{\mathrm{sat}} = 40\,\mathrm{nm}$ and a saturation impurity areal density $n_{\mathrm{sat}} = 10^{-2}\,\mathrm{nm}^2$.

For the Debye length, we will use $\lambda_{\mathrm{D}} = 10\,\mathrm{nm}$. We will also use an incoming impurity concentration $C_0 = 10^{10}/\mathrm{m}^3$, the viscosity typical of water $\eta = 10^{-3}\,\mathrm{Pa\,s}$, and a pressure difference $P = 10^5\,\mathrm{Pa}$. These parameter values are also of the same order as the experimental conditions imposed in [51, 52] and in [58, 59]. We have checked, however, that the results of our simulations are invariant with respect to the last three parameters except for a multiplicative rescaling of the time values; as already described in detail in [61], this is due to the symmetry of the starting formulas. Consequently, in the present article we shall preferentially express the times resulting from all our simulations normalized with respect to a common reference value t_{ref}. In particular, for this t_{ref} we will choose (as described in detail in Section 8.4.1) the half-saturation time of the cylindrical cylinder with diameter 300 nm. Increases in η would merely increase t_{ref} linearly, while increases in C_0 and P would induce an inversely proportional change in t_{ref}.

Concerning the size of the tubular conduits, we will always use a length $L = 1\,\mathrm{mm}$. For cylinders (Section 8.4.1) we will use diameters from 250 nm to 400 nm. For tube geometries with variable diameter (Sections 8.4.2 to 8.4.4) we will use minimum, average and maximum diameters of, respectively, 200 nm, 300 nm and 400 nm.

Let us also briefly comment here on the fact that the above typical parameter values (especially pressure) correspond to moderate flow velocities, in particular small enough to fulfill the assumption made by the model equations that axial advection effects do not complicate the recovery, after each impurity is removed from the liquid flow, of transversal equilibrium in the impurity concentration profile. [61] This is because the typical time it takes diffusion to rebuild transversal equilibrium is orders of magnitude smaller than the typical time each impurity travels within the collision distance from the walls before being removed from the liquid: The first of those times may be estimated as λ^2/D, [160] where D is the diffusion coefficient ($\sim 10^{-9}\mathrm{m}^2\,\mathrm{s}$) and λ the typical transversal distance over which equilibrium has to be reestablished (in our case this may be taken somewhere between λ_D and ρ_e, *i.e.*, 10–30 nm). This leads to times of the order of 10^{-6} s. In contrast, the typical time that each impurity travels within the collision distance from the walls before being removed from the liquid may be estimated to be orders of magnitude larger, of the order of 4×10^{-2} s (by simply combining an average Poiseuille velocity of $Pd^2/(32L\eta)$, a typical diameter $d \sim 300$ nm, and a typical distance traveled before being trapped of $1/\Omega_0 = 10^{-5}$ m).

Chapter 8

Results for the influence of the microgeometry of ENM on the nanofiltration characteristics

Summary of the chapter:

We consider the possibility of improving by means of microgeometry optimization the operational characteristics of electrostatic nanostructured microporous (ENM) media when used for trapping (nanofluid filtration). For that task, we apply the computational methods introduced in the previous chapter, to different candidate and representative shapes for the microconduits, including cylindrical (of different radius), increasing conical, decreasing-conical and sinusoidal-corrugated, we focus only in the logarithmic removal rate (LRV) performance (important for clinical and drinking water applications) but also on energy optimization (crucial for large-scale industrial effluent treatment). Our results suggest, for instance, that decreasing-conical and sinusoidal-corrugated microconduits have better initial nanoimpurity removal rate (and longer operational lifetime, for most standard requirement criteria) than the one achieved by simple cylindrical microconduits. These geometries also improve the energy efficiency of the filtration (watts per spent removed nanoimpurity), with the decreasing-cone geometry particularly standing out in this respect.

8.1 Overview

In the last chapter we have remarked the importance of the development of new techniques of water filtration and their application in both academy and industry. [51–60] The improvement of such techniques is also important to optimize the industrial processes. As we commented before, one of the most promising filtration techniques is based on the nanofunctionalization of the inner walls of pores of diameters with charged nanoparticles. [51–60]

For that reason we have used the adapted theory detailed in the last chapter that is used to describe the filtration in this kind of nanostructured media to study the influence of the geometry in the filtration performance of this type of filtration technique. We thus study this influence through some analytical results within this theory, and some numerical results obtained computationally with the LBTS-εpsilon.

We are able to study different parameters, as the filtration performance LRV, the operational lifetime, and the energetic balances of each geometry. With all these parameters it is possible to optimize the geometry of the conduits to improve the removal features of the filter.

In Section 8.2 we present our results for the filtration performance in the initial, clean state of the macropores. The results in that Section include also analytical equations (exact within the model) for the initial logarithmic removal value LRV_0 for some relevant geometries: cylinders, increasing and decreasing cones, and sinusoidally corrugated tubes. In Section 8.3 we present analytic equations for the hydrodynamic energy per mean areal density of trapped impurities at initial time for cylinders with different diameters, and we compare them with the values obtained numerically. In Section 8.4 we compute, for each of those macropore geometries, the full evolution of the filtration characteristics with time (as impurities flow and progressively cover the nanotexture, reducing the filtration performance). This includes, *e.g.*, the evolution of the filtration performance, the thickness of the trapped-impurity layer, or the operational lifetime for each macropore geometry. Finally, Section 8.5 summarizes our main conclusions.

8.2 Initial, clean state performance of the nanofunctionalized microporous media

In this Section we will obtain some analytical expressions for the initial ($t = 0$) logarithmic removal value LRV_0 of tubular conduits with different geometries by studying Equations (7.4) to (7.6). This will be useful both *per se* and as a consistency check of the validity of the computations.

While the LRV may in principle be numerically computed, for arbitrary t-values, directly from Equation (7.7), a more interesting analytical expression is derived by obtaining from Equation (7.4) the trapping probabilities in each finite x-slice, and from them the non-trapping probabilities. The latter have to be multiplicatively accumulated over all of the conduit, and we take the logarithm of the result to obtain LRV(t):

$$\begin{aligned}\mathrm{LRV}(t) &= -\sum_i \log_{10}\left[1-\Omega_0^{\mathrm{finite}}\left(1-\left\|\frac{n(x_\mathrm{i},t_\mathrm{j})}{n_\mathrm{sat}}\right\|\right)\times\right. \qquad (8.1)\\ &\qquad \left.\left(\left(\left\|\frac{2\rho_\mathrm{e}(x_\mathrm{i},t_\mathrm{j})}{d(x_\mathrm{i})-n(x_\mathrm{i},t_\mathrm{j})\delta_\mathrm{sat}/n_\mathrm{sat}}\right\|-1\right)^2-1\right)^2\Delta x\right].\end{aligned}$$

In the clean state (*i.e.*, in the initial time $t=0$) it is $n(x_i,0)=0$ and $\rho_e(x_i,0)=\rho_{\mathrm{e0}}$, so that

$$\mathrm{LRV}_0 = -\sum_i \log_{10}\left(1-\Omega_0^{\mathrm{finite}}\left[\left(\left\|\frac{2\rho_\mathrm{e0}}{d(x_\mathrm{i})}\right\|-1\right)^2-1\right]^2\Delta x\right). \qquad (8.2)$$

By considering in the above expressions the limit $\Delta x \to dx$, we obtain for the continuous model:

$$\mathrm{LRV}_0 = (\ln 10)^{-1}\int_{x=0}^{L}\Omega_0\left[\left(\left\|\frac{2\rho_\mathrm{e0}}{d(x)}\right\|-1\right)^2-1\right]^2\mathrm{d}x, \qquad (8.3)$$

where we employed the power expansion $\log_{10}(1-y\mathrm{d}x)\approx -y\mathrm{d}x/\ln 10$. Let us now apply this result to some relevant geometries (the same as also considered in Section 8.4). We start with a cylindrical conduit of constant diameter $d=\rho_\mathrm{e0}\delta$ (we introduce here normalization by ρ_e0 for the shake of brevity of our final expressions). Application of Equation (8.3) leads to:

$$\mathrm{LRV}_0^{\mathrm{cylinder}} = \frac{16\Omega_0 L}{\ln 10}\left[\frac{1}{\delta^2}-\frac{2}{\delta^3}+\frac{1}{\delta^4}\right] \qquad (8.4)$$

(where we assumed $d>2\rho_\mathrm{e0}$; for the general case just replace $2/\delta$ by $||2/\delta||$). For a conical tube with maximum and minimum diameters $\rho_\mathrm{e0}\delta_\mathrm{M}$ and, respectively, $\rho_\mathrm{e0}\delta_\mathrm{m}$, Equation (8.3) leads to (again we assume $d(x)>2\rho_\mathrm{e0}$ for notational simplicity):

$$\mathrm{LRV}_0^{\mathrm{cone}} = \frac{16\Omega_0 L}{3\ln 10}\left[\frac{3}{\delta_\mathrm{m}\delta_\mathrm{M}}-\frac{\delta_\mathrm{m}+\delta_\mathrm{M}}{(\delta_\mathrm{m}\delta_\mathrm{M})^2}+\frac{(\delta_\mathrm{m}+\delta_\mathrm{M})^2-\delta_\mathrm{m}\delta_\mathrm{M}}{(\delta_\mathrm{m}\delta_\mathrm{M})^3}\right]. \qquad (8.5)$$

Let us emphasize here that Equation (8.5) is valid both for diameters increasing or decreasing along the axial coordinate. The results for $t \neq 0$ that will be obtained in Sections 8.4.2 and 8.4.3 will show that decreasing-conical and increasing-conical conduits experience different time-evolution in spite of their equal initial filtration performance.

Let us now consider a sinusoidally corrugated tube with maximum and minimum diameters $\rho_{\mathrm{e}0}\delta_{\mathrm{M}}$ and, respectively, $\rho_{\mathrm{e}0}\delta_{\mathrm{m}}$, and an integer number n of oscillation periods of the diameter profile. Specifically, $d(x)$ is given by $2d(x)/\rho_{\mathrm{e}0} = \delta_{\mathrm{M}} + \delta_{\mathrm{m}} + (\delta_{\mathrm{M}} - \delta_{\mathrm{m}})\sin(2n\pi x/L)$. For $\mathrm{LRV}_0^{\mathrm{sinus}}$ we obtain, using Equation (8.3) (again for $d(x) > 2\rho_{\mathrm{e}0}$):

$$\begin{aligned} \mathrm{LRV}_0^{\mathrm{sinus}} \quad = \quad & \frac{\Omega_0 L}{\ln 10}\left[\frac{8(\delta_{\mathrm{M}}+\delta_{\mathrm{m}})}{(\delta_{\mathrm{M}}\delta_{\mathrm{m}})^{3/2}} + \frac{4(3{\delta_{\mathrm{M}}}^2 + 2\delta_{\mathrm{M}}\delta_{\mathrm{m}} + 3{\delta_{\mathrm{m}}}^2)}{(\delta_{\mathrm{M}}\delta_{\mathrm{m}})^{5/2}} + \right. \\ & \left. \frac{(\delta_{\mathrm{M}}+\delta_{\mathrm{m}})(5{\delta_{\mathrm{M}}}^2 - 2\delta_{\mathrm{M}}\delta_{\mathrm{m}} + 5{\delta_{\mathrm{m}}}^2)}{(\delta_{\mathrm{M}}\delta_{\mathrm{m}})^{7/2}}\right]. \end{aligned} \tag{8.6}$$

Note that the result is independent of the number of oscillations n. This holds true only if n is integer (and nonzero).

While the numerical results for $\mathrm{LRV}(t)$ in different geometries $d(x)$ presented in Tables 8.1 and 8.2 and in Figure 8.5 correspond to the values obtained by numerical simulation of Equations (7.4) to (7.6) (see Section 8.4 for details), we note here that the values for $t = 0$ (*i.e.*, LRV_0) in those Tables and Figures fully coincide with the results obtained by directly applying Equations (8.4) to (8.6).

8.3 Initial, clean state energy consumption rate for filtration

In this Section we will obtain some analytical expressions for the initial energy consumption cost of filtration per trapped impurity, henceforth noted $\mathcal{E}(t = 0)$. This is going to be useful *per se* to compare the energetic balance between geometries, and to check the validity of our simulations.

We start by considering the hydrodynamic energy, or the energy applied to the system to transport the total volume of liquid from the beginning to the end of the channel. This energy can be calculated using the analogy with the theory of electrical circuits. The power dissipated is given by the product of the the voltage V and the intensity I. In the case of the fluid mechanics, the paper of voltage is played by the pressure P, and the analog of the intensity is the flow rate Φ. Therefore, the power dissipated is given by the product of the pressure and the flow. Thus, the hydrodynamic energy wasted at time t is the integration of the power dissipated from initial state up to that time t:

$$E(t) = \int_0^t P\Phi(t'). \tag{8.7}$$

We are interested in calculating the hydrodynamic energy per trapped impurities in the whole tube n_{tot}, *i.e.*, the energy that is needed to increase the number of impurities added to the walls in the whole tube an amount dn. Therefore, n_{tot} is given by:

$$n_{\text{tot}} = 2\pi \int_0^L n(x,t) r_0(x) dx, \tag{8.8}$$

where $r_0(x)$ is the clean-state radius of the tube in the x position. It is important to remark that the areal density n is always defined respect to the transversal area in the clean state. Therefore, $r_0(x)$ does not depend on time. Taking this definition into account, $\mathcal{E}$ can be written in terms of two derivatives in this way:[1]

$$\mathcal{E} = \frac{dE}{dt}\frac{dt}{dn_{\text{tot}}}. \tag{8.9}$$

The first derivative is simply given by the product of flux $\Phi(t)$ at time t and the pressure P. On the other hand the inverse of second derivative is directly given by the equation 7.4. Taking into account these, it is possible to obtain a general analytic equation for $\mathcal{E}(t)$, given by:

$$\mathcal{E}(t) = \frac{P}{\int_0^L C_{imp}(x,t)\Omega_0^{finite}\left(1 - n(x,t)/n_{sat}\right) f_e(x,t) dx}. \tag{8.10}$$

We are interested in obtaining this quantity for the initial state, *i.e.*, $t = 0$ and $n(x, t = 0) = 0$. This greatly will simplify the above equation, because we know the analytic values of $f_e(x, t = 0)$ and Ω_0^{finite}. On the other hand, it is possible to calculate the value of $C_{imp}(x, t = 0)$ for some geometries.

Taking into account the same argument used for the LRV in the previous chapter (Section 7.2.1) to analyze it in terms of a discretized model, if we take

---

[1] The hydrodynamic energy rate is full rigor not the only energy that is playing a role in this kind of filtration. The other contribution that could play an important role in the filtration process is the binding energy per impurity. However, this becomes negligible, as may be seen by comparing the order of magnitude between the hydrodynamic energy rate and the binding energy. In the most extreme case, the more energetic bond between the impurities and the walls is going to be an ionic one, that has typically 10^{-18} J/impurity. If we compare this with the minimum hydrodynamic energy rate that plays a role in our filtration, given by Equation (8.15), we have a value about 10^{-5} J/impurity. Therefore, independently of the exothermic or endothermic character of the bonding, the hydrodynamic rate overcome the other energy contributions.

into account that the probabilities of accumulating impurities are multiplicative, we can write $C_{imp}(x_i, t=0)$ as:

$$C_{imp}(x_i, t=0) = C_0 \prod_{k=1}^{i} \left(1 - \Omega_0 f_e(x_k, t=0) \frac{x_k}{i}\right). \tag{8.11}$$

It is important to remark that the ratio $x_k/k = \Delta x$ is constant. Therefore, if $f_e(x_k, t=0)$ is also constant (*e.g.*, for the cylindrical case), the equation simplifies to:

$$C_{imp}(x_i, t=0) = C_0 \left(1 - \Omega_0 f_e^0 \frac{x_i}{N_i}\right)^i, \tag{8.12}$$

where f_e^0 is the constant value $f_e(x_k, t=0)$. Moreover, if i is large enough, it can be approximated as:

$$C_{imp}(x_i, t=0) \approx C_0 exp\left(-\Omega_0 f_e^0 x_i\right). \tag{8.13}$$

This is the case of the cylinder. Introducing this result in equation 8.10 we get an analytically closed energy cost per trapped impurities for a conduit with a cylindrical shape:

$$\mathcal{E}(t=0) = \frac{P}{C_0\left[1 - \exp(-\Omega_0 f_e^0 L)\right]} \tag{8.14}$$

We have confirmed that the value obtained with this equation for cylinders with diameters 250, 300, 350 and 400 nm are the same values as obtained integrating numerically equations 7.4 and 7.5. In this equation, the quantity that depends on the diameter d_0 is f_e^0 (See Equation (7.2)). However, with these values of diameter, the product $\Omega_0 f_e^0 L \gg 1$, so the value of the exponential is almost 0, and $\mathcal{E}(t=0)$ is simply:

$$\mathcal{E}(t=0) \approx \frac{P}{C_0}. \tag{8.15}$$

Therefore, in this regime there is no dependence with the diameter of the cylinder. It is necessary to remark that this regime corresponds to the cases where the initial LRV value is very high, *i.e.*, when the channel is able to filter the total amount of impurities in the tube and the shape of the tube does not change with time. This is valid for tubes with small enough radius at initial times. In this case, the total energy rate is given by the ratio between the hydrodynamic energy that is needed to carry the volume of liquid through the tube at pressure P and the number of impurities that are contained in the tube. This is given by Equation (8.15).

However, when the filter starts to get saturated, the amount $\Omega_0 f_e^0 L \approx 0$, and the energy rate increases.

For a non-cylindrical shape, it is possible to integrate numerically equation 8.10 to obtain the value at initial-clean state, taking into account that $C_{imp}(x_i, t = 0)$ is given by equation 8.11. We have also checked that these values are the same as calculated by the numerical integration of equations 7.4 and 7.5, confirming the validity of our simulations. That main result in this case is that in the limit that we are analyzing, the initial $\mathcal{E}$ does not depend on the shape of the conduit if it has the same mean diameter and length.

8.4 Time-evolution of the nanofiltration

8.4.1 Simulation results for cylindrical conduits

We first explore the filtration characteristics of cylinders as a function of their diameter. For that purpose, let us consider four cylinders, of diameters 250, 300, 350 and 400 nm (the rest of the parameters entering Equations (7.4) to (7.6) being, for all the cylinders, equal to those detailed in Section 7.2.5).

We present in Table 8.1 the numerical results obtained for the initial logarithmic removal value LRV_0 and the operational lifetime (for the $\mathrm{LRV} \geq 5$, $\mathrm{LRV} \geq 2$ and $\mathrm{LRV} \geq 1$ criterions) of these cylindrical nanofunctionalized macropore conduits. Also, Figure 8.1 illustrates the results of our simulations for two example diameters (300 and 400 nm). In particular, the left-hand column of Figure 8.1 (*i.e.*, panels 8.1(a) and 8.1(c)) shows the internal profile of the trapped-impurity layer in each tube at different instants of the time evolution, *i.e.*, their true internal radius as the conduits become narrower due to the accumulation of trapped impurities. These profiles are shown for the following instants of time: For $t = 0$, or clean state (when the radius coincides with its nominal value $d(x)/2$); for $t = t_{\mathrm{sat}}$, *i.e.*, when all of the conduit has reached its saturated state (and the internal radius equals $(d(x) - \delta_{\mathrm{sat}})/2$); and also for two intermediate times, $t_{0.15}$ and $t_{1/2}$, defined by the conditions $\bar{n}(t = t_{0.15}) = 0.15$ and $\bar{n}(t = t_{1/2}) = 0.5$, where $\bar{n}$ is the average areal density of trapped impurities in the whole tube.

A first result of our simulations, already easily visible in these Figures 8.1(a) and 8.1(c), is that the impurities accumulate first at the beginning of the cylinders, instead of uniformly.

The right-hand column of Figure 8.1 (*i.e.*, panels 8.1(b) and (d)) shows the time-evolution of the areal density of trapped impurities at opposite ends of the cylindrical tube, $n(x = 0, t)$ and $n(x = L, t)$. It also shows the average areal density $\bar{n}(t)$ used to calculate the times $t_{0.15}$ and $t_{1/2}$ (that are marked as solid points in these panels). The timescale in this Figure is normalized as t/t_{ref}, where t_{ref} is chosen as the $t_{1/2}$ value of the cylinder with diameter 300 nm. The same

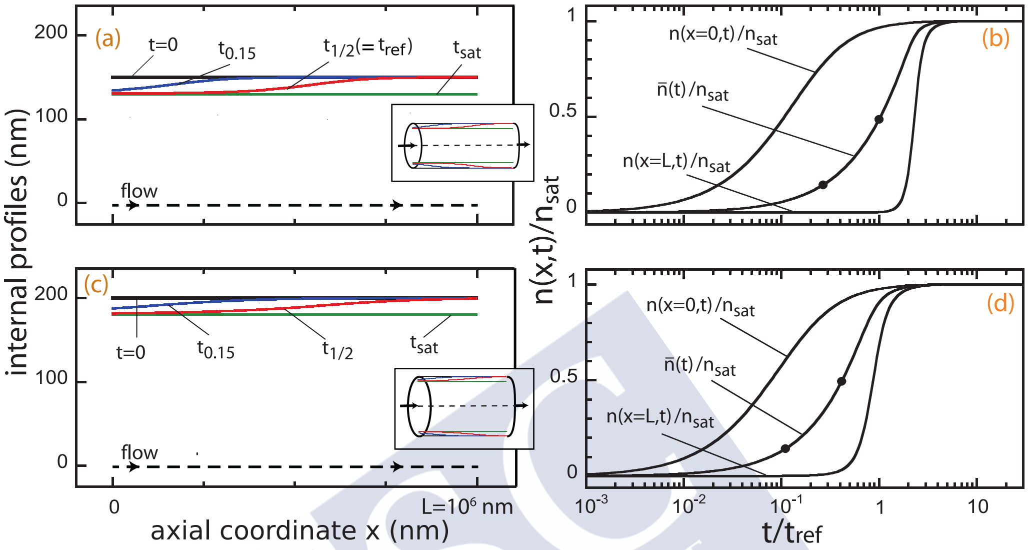

Figure 8.1: Results of our numerical simulations for nanofunctionalized macropore conduits with the geometries shown in the insets of the left column (cylinders of nominal diameter 300 and 400 nm). Sections 7.2.4, 7.2.5 and 8.4.1 of the main text detail the parameter values and the procedural details used to obtain these results. Figures (a) and (c) show the internal profiles of the trapped-impurity layer as time advances and impurities accumulate on the walls. At $t = 0$ the internal radius equates the nominal value. The time t_{sat} corresponds to the fully-saturated state. The intermediate times $t_{0.15}$ and $t_{1/2}$ (solid points in Figures (b) and (d)) are defined as the instants when the areal density of trapped impurities averaged over all of the tube, $\bar{n}(t)$, becomes respectively 0.15 and 1/2 times the saturation value n_{sat}. Figures (b) and (d) show the time-evolution of the areal density of trapped impurities evaluated at both the entrance and the exit of the conduit, and also the average $\bar{n}(t)$. Note that the time axis is logarithmic and normalized by a reference value, t_{ref}, common for all our simulations and geometries and defined as the value of $t_{1/2}$ of the cylinder of diameter 300 nm (see Figure (a)). See also Table 8.1 for further numerical information on these simulations.

common t_{ref} will be used in all of the Figures and Tables of the present work.

These representations evidence that for cylindrical conduits the growth with time of $n(x,t)$ happens earlier when closer to the start of the tube ($x = 0$) than when closer to the exit point ($x = L$), by at least one order of magnitude in time value (note that the time axis in Figure 8.1 is logarithmic). As it could be expected, the behavior of $\bar{n}(t)$ is intermediate between the ones at both edges of the conduit.

The results of our simulations also serve to study the influence of the diameter of the cylinders over the filtration performance and operational lifetime, as given by the logarithmic removal value LRV. In Table 8.1 we list for each diameter the LRV value computed at the initial time, LRV_0, that characterizes the maximum filtration capability of the cylinder (achieved in the initial, clean state). The results in Table 8.1 indicate a better LRV_0 for the smaller diameters, as it could be probably expected by arguing that for smaller diameters a larger percentage of the fluid moves closer than $\rho_{\mathrm{e}0}$ from the walls.

Table 8.1 also lists the times at which the LRV reaches the thresholds LRV$= 5$, LRV$= 2$ and LRV$= 1$, *i.e.*, the operational lifetimes for three different filtration requirements. Logically, the LRV ≥ 5 lifetime is null for the cases in which $\mathrm{LRV}_0 < 5$. The results in this Table show that the lifetimes become significantly larger when the diameter becomes smaller. This trend may be already noticed in Figures 8.1(b) and (d), where a similar change may be seen in the times at which the $n(t)$ curves reach the saturation value (in fact, a similar evolution may be also noticed for $t_{0.15}$ and $t_{1/2}$). This is likely also influenced by the fact that the flow is slower when the diameter decreases, making the absorption slower too (note that our simulations are performed at constant P, rather than at constant Φ).

Note that initial hydrodynamic energy rate is going to be constant for all the diameters that we are analyzing, because we are in the regime where $\Omega_0 f_e^0 L \gg 1$, so $\mathcal{E}$ is given by Equation (8.15). The limit when the exponential factor is about 0.01, and this correction starts to be significant in the calculation of the hydrodynamic rate, is $d = 530\,\mathrm{nm}$. However, in this regime, the value of the hydrodynamic energy rate is going to change differently for different diameters with time, as we can see from Equation 8.10. Thus, this special case only happens for the initial value.

8.4.2 Simulation results for increasing-conical tubular conduits.

Let us now show that other conduit geometries may improve the filtration performance and/or operational lifetimes with respect to those obtained for cylinders. We begin that investigation by studying, in this Subsection, conical tubular conduits with diameter increasing in the direction of the fluid flow. Note that these are indeed feasible macropore geometries: there exist experimental studies of membranes with conical (increasing and decreasing) pore shapes [147–149] for different applications, such as the study of resistive-pulse biosensors [147] or capillary electrophoresis [149]. However, none of these researches have studied the nanofunctionalization of these conical-shape pores for water filtration applications.

In Figure 8.2 we present the results obtained by performing our simulations with the $d(x)$ function corresponding to the increasing-conical geometry. In particular, the diameter increases linearly from the value 200 nm at the entrance to the tube up to the value 400 nm at the exit point (this is to be compared therefore with the 300 nm cylinder). Again it is visible that impurities accumulate sooner at the entrance of the tubes than at their exit. But it can be noticed in the Figures that the differences are now even larger than in the cylindrical case. As a consequence, the $\bar{n}(t)$ evolution also spreads over a wider t-range.

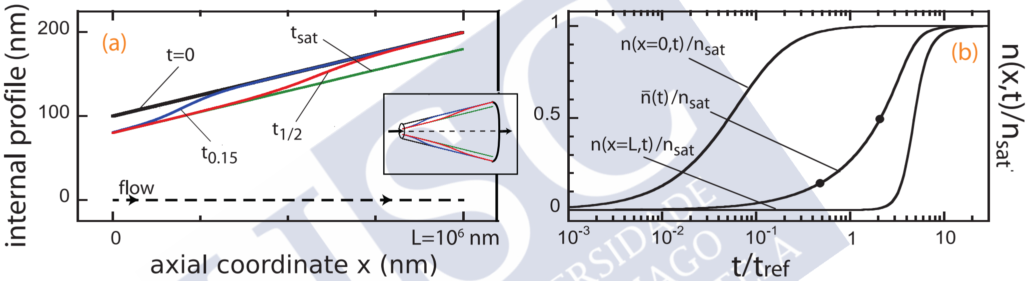

Figure 8.2: Results of our numerical simulations for a nanofunctionalized macropore conduit of the increasing-conical geometry pictured in the inset of (a) (with a nominal diameter value 200 nm for the narrower section and 400 nm for the wider section, and therefore 300 nm as average diameter). Sections 7.2.4, 7.2.5 and 8.4.2 of the main text provide parameter values and further details of these simulations. Figure (a) shows the internal profile of the trapped-impurity layer as time advances and nanoimpurities accumulate in the walls. The times t_{ref}, t_{sat}, $t_{0.15}$ and $t_{1/2}$ are defined as in Figure 8.1 and its caption (in Figure (b) $t_{0.15}$ and $t_{1/2}$ are signaled as solid points). Figure (b) shows the time-evolution of the areal density n of trapped impurities evaluated at both the entrance and the exit of the conduit, and also the average $\bar{n}(t)$. See also Table 8.2 and Figure 8.5 for further information on these simulations.

As it may be noticed from the values listed in Table 8.2, the LRV_0 value achieved by the increasing cone improves the one of the equivalent cylinder (6.2-log versus 5.6-log).

More significantly, Table 8.2 also indicates that the increasing-cone geometry increases the operating lifetimes by about 24% (for the LRV$\geq$ 5 criterion), a 40% (for the LRV$\geq$ 2 criterion) or by about 71% (for the LRV$\geq$ 1 criterion) with respect to cylinders with the same average diameter. These differences are also illustrated in Figure 8.5, that compares the LRV(t) curves of conduits with different shapes (but with equal average diameter along the axial direction). We note again that the time axis in all our Figures is expressed normalized by a common reference value (t_{ref} defined as $t_{1/2}$ of the $d = 300\,\mathrm{nm}$ cylinder) and in logarithmic scale.

These results indicate, therefore, that a possible path to greatly increase the operational lifetime of nanoenhanced macropore filters is to employ a supporting media containing pores with variable diameter. In the following Sections, this conclusion will be extended to other example conduit shapes.

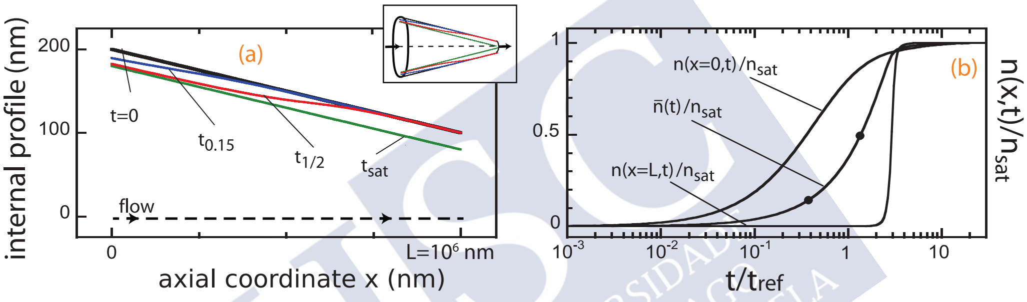

Figure 8.3: Results of our numerical simulations for a nanofunctionalized macropore conduit of the decreasing-conical geometry pictured in the inset of (a) (with a nominal diameter value 200 nm for the narrower section and 400 nm for the wider section, and therefore 300 nm as average diameter). Sections 7.2.4, 7.2.5 and 8.4.3 of the main text provide parameter values and further details of these simulations. Figure (a) shows the internal profile of the trapped-impurity layer as time advances and nanoimpurities accumulate in the walls. The times t_{ref}, t_{sat}, $t_{0.15}$ and $t_{1/2}$ are defined as in Figure 8.1 and its caption (in Figure (b) $t_{0.15}$ and $t_{1/2}$ are signaled as solid points). Figure (b) shows the time-evolution of the areal density n of trapped impurities evaluated at both the entrance and the exit of the conduit, and also the average $\bar{n}(t)$. See also Table 8.2 and Figure 8.5 for further information on these simulations.

In relation to the hydrodynamic energy rate, Figure 8.6 shows taht the initial $\mathcal{E}$ is the same for all the channels with same mean diameter. However, the evolution with time is quite different depending on the geometry. This figure and its inset shows that trapping impurities costs more hydrodynamic energy for the increasing-cone geometry than for the cylinder after the time given by the

LRV$\geq$ 2 criterion. To sum up, this geometry improves the initial LRV and the lifetime in relation to the cylinder, but it needs a higher amount of hydrodynamic energy to filter.

8.4.3 Simulation results for decreasing-conical tubular conduits.

We consider now a decreasing-conical geometry, *i.e.*, a linearly decreasing diameter $d(x)$ function. Again we use in our simulations 200 and 400 nm for the extreme diameter values, and the mean diameter along the axial direction remains 300 nm. Figure 8.3 illustrates the results of our simulations for that geometry. A significant qualitative difference with respect to the previous increasing-cone conduit is that now the plots versus time of $n(x = 0, t)$ and $n(x = L, t)$ are significantly closer to each other. In fact, near the saturation state both lines even cross each other. This means that no longer is always true that the beginning of the conduit, $x = 0$, accumulates impurities faster than its end, $x = L$. Instead, the smaller section at the end of the cone is able to overcome the rhythm of impurity accumulation of the first slices of the cone before these get saturated.

This more uniform filling by impurities results in a different evolution with time of the filtration performance. As revealed by the values listed in Table 8.2 (see also Figure 8.5), the initial LRV values of the increasing and decreasing cones are coincident, but the LRV$\geq$ 5 lifetime of the decreasing cone is even longer than the one of the increasing cone (about 3.5 times longer than in the increasing cone, and also $\sim$ 335% longer than in the cylinder of equal mean diameter). In contrast, the LRV$\geq$ 1 lifetime of decreasing cones is shorter that the one of increasing cones (14% shorter, though still 48% longer than for equivalent cylinders). On the other hand, the LRV$\geq$ 2 criterion reveals a tendency located in the middle of the other two criterions, getting a higher lifetime in comparison both with the cylinder (73% higher) and the increasing-cone (24% higher). This can be understood by observing in Figure 8.5 that the LRV(t) curves of both types of conical shapes cross each other near LRV$\sim$ 1.5.

In relation to the hydrodynamic energy, Figure 8.6 reveals that below the point where $\overline{n}/n_{\text{sat}} \sim 0.95$, the decreasing cone is the geometry that optimizes better the hydrodynamic energy of the system. Above this amount, the inset shows that is the cylinder the type of channel that improves better the energy efficient. Therefore, to sum up, the decreasing-cone has better lifetime than the cylinder and the increasing-cone (in the higher LRV criterions), it has better capability for filtration in the most part of the time-region, and it is the most efficient energetically speaking when the filter is no.

8.4.4 Simulation results for sinusoidally corrugated tubular conduits.

Let us now consider tubular macropores of diameter increasing and decreasing successively along their axis. Again this macropore geometry is experimentally realizable, and studies exist on macropore networks composed by pores with spherical shape and interconnections (throats) of small radius forming sinus-like shapes. For an example see [145]. Also relevant is the fact that some theoretical studies have analyzed these porous media as a network of pores with sinus-like shapes. [150, 151]

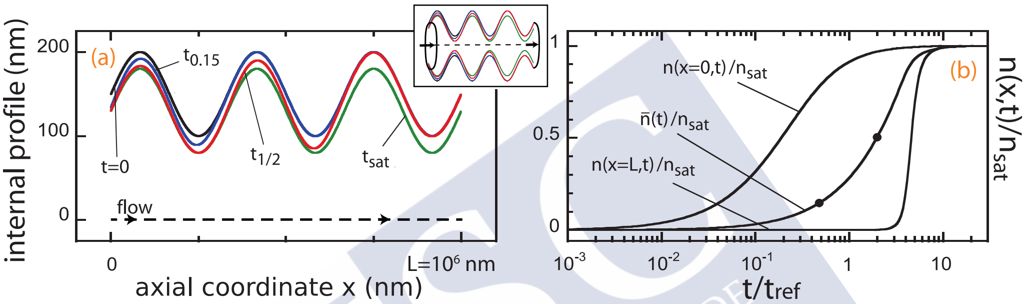

Figure 8.4: Results of our numerical simulations for a nanofunctionalized macropore conduit of the sinusoidally corrugated geometry pictured in the inset of (a) (with a nominal diameter value 200 nm for the narrower section and 400 nm for the wider section, and therefore 300 nm as average diameter). Sections 7.2.4, 7.2.5 and 8.4.4 of the main text provide parameter values and further details of these simulations. Figure (a) shows the internal profile of the trapped-impurity layer as time advances and nanoimpurities accumulate in the walls. The times t_{ref}, t_{sat}, $t_{0.15}$ and $t_{1/2}$ are defined as in Figure 8.1 and its caption (in figure (b) $t_{0.15}$ and $t_{1/2}$ are signaled as solid points). Figure (b) shows the time-evolution of the areal density n of trapped impurities evaluated at both the entrance and the exit of the conduit, and also the average $\bar{n}(t)$. See also Table 8.2 and Figure 8.5 for further information on these simulations.

A $\sin(x)$-like diameter functionality is possibly one of the simplest of the corrugated geometries, and could a priory be expected to serve as a fair first approximation to, at least, the most essential features of real corrugated pores. [145, 150, 151] In Figure 8.4 we present the results for our simulations using for the diameter profile the function $d(x) = (300\,\text{nm}) + (100\,\text{nm})\sin(6\pi x/L)$, *i.e.*, the maximum, minimum and mean diameter are the same as in the previous two Subsections, and $d(x)$ presents three oscillations over the conduit's length (we

diameter of cylindrical conduit	**LRV$_0$**	**LRV≥ 5 lifetime**	**LRV≥ 2 lifetime**	**LRV≥ 1 lifetime**
250 nm	7.7	1.16 t_{ref}	1.28 t_{ref}	3.56 t_{ref}
300 nm	5.6	0.18 t_{ref}	1.79 t_{ref}	1.77 t_{ref}
350 nm	4.3	-	2.22 t_{ref}	0.95 t_{ref}
400 nm	3.3	-	2.66 t_{ref}	0.53 t_{ref}

Table 8.1: Summary of the main filtration performance figures for nanofunctionalized macropore conduits of cylindrical geometry and different diameters, obtained by using the numerical simulation procedures and parameter values described in Sections 7.2.4, 7.2.5 and 8.4.1 (see also Figures 8.1 and 8.5 for plots of the detailed time evolution of the simulation results). The reference time t_{ref} is the same as defined in Figure 8.1 and its caption. The initial logarithmic removal values, LRV$_0$, obtained from these simulations fully coincide with the direct application of Equation (8.4). The operational lifetime using the LRV≥ 5 criterion is null for the cylinders in which LRV$_0 < 5$, and is not shown.

have checked that increasing the number of oscillations would not qualitatively affect our results; note also that according to Equation (8.6) LRV$_0^{\text{sinus}}$ does not depend on the number of oscillations).

The time-evolution of the internal profiles shown in Figure 8.4(a) evidences that in the corrugated conduits the impurities accumulate first in the initial oscillation periods, and within that tendency they accumulate first in their narrower portions. This result is coherent with a naive vision of crudely considering the corrugated conduits as a combination in series of alternately increasing and decreasing cones. The time-evolution of the average $\bar{n}(t)$ and of the filtration performance LRV(t) also resembles somewhat the results obtained for cones. However, it must be noted that the initial LRV performance is better than the one of the cylindrical and conical shapes (see Table 8.2 and Figure 8.5). The difference is almost of one logarithmic unit with respect to the cylinder. Concerning the operational lifetime, with the LRV≥ 5 criterion it is almost as long as in the decreasing cone (14% shorter) and still much longer than for cylinders (276% longer). This is achieved without penalizing the LRV≥ 1 lifetime: on the contrary, with the LRV≥ 1 criterion the operational lifetime is the longest in Table 8.2 (being in particular 108% longer than for the equivalent cylinder). Moreover, the LRV≥ 2 criterion neither penalizes the lifetime, because is also 108% longer than the cylinder.

In terms of the hydrodynamic energy rate, it can be seen in Figure 8.6 that for $\overline{n}/n_{\text{sat}} < 0.9$, the sinus geometry mimics quite well the behavior of its equivalent cylinder. However, for higher values, the sinus becomes energetically less efficient, and starts to become more similar to the increasing cone, which is the one less efficient. To sum up, the sinus geometry optimizes the lifetimes and the LRV, but is less efficient than the decreasing cone in terms of hydrodynamic energy.

conduit geometry (average diameter 300 nm)	$\mathbf{LRV_0}$	**LRV**≥ 5 **lifetime**	**LRV**≥ 2 **lifetime**	**LRV**≥ 1 **lifetime**
cylinder	5.6	$0.17\ t_{\mathrm{ref}}$	$1.28\ t_{\mathrm{ref}}$	$1.71\ t_{\mathrm{ref}}$
increasing cone	6.2	$0.21t_{\mathrm{ref}}$	$1.79\ t_{\mathrm{ref}}$	$2.93\ t_{\mathrm{ref}}$
decreasing cone	6.2	$0.74\ t_{\mathrm{ref}}$	$2.22\ t_{\mathrm{ref}}$	$2.53\ t_{\mathrm{ref}}$
sinusoidally corrugated	6.4	$0.64\ t_{\mathrm{ref}}$	$2.66\ t_{\mathrm{ref}}$	$3.56\ t_{\mathrm{ref}}$

Table 8.2: Summary of the main filtration performance figures for conduits with different geometries but equal average diameter 300 nm, obtained by using the numerical simulation procedures and parameter values described in Sections 7.2.4 and 7.2.5. The reference time t_{ref} is the same as defined in Figure 8.1 and its caption. The LRV_0 values obtained from these simulations fully coincide with the direct application of Equations (8.4) to (8.6).

8.5 Conclusions

To sum up, we have studied the performance of macropores (conduits of micrometric diameter) with nanostructured inner walls, with regards to their performance and operational lifetime when used as filters of nanoparticles in suspension in aqueous liquids (nanofluids). We have considered different geometries, including cylinders of different diameters and tubes with diameter varying along the direction of the fluid flow (increasing and decreasing conical tubes and sinus-corrugated tubes). We focused mainly on the influence of the nominal geometry over the initial logarithmic removal value LRV_0, the operational lifetimes, energetic balances, and the spatial profile of the trapped-impurity layer in the inner walls of the conduits.

We first studied the impact of the diameter size for cylindrical macropore conduits. We found that decreasing the diameter improves the LRV_0 and operational lifetimes and maintains the hydrodynamic energy rate $\mathcal{E}$.

Then we tested tubular macropores with cross-sectional diameter varying along the flow direction, and found that these variations allow to improve the filtration characteristics without decreasing the average diameter of the conduit. In particular *i)* increasing-conical conduits have, with respect to cylinders with the same average diameter, moderately better LRV_0 significantly longer operational times (about 70% longer) and worse hydrodynamic energetic rates; *ii)* decreasing-conical conduits equally improve LRV_0 and extend even further the operational times for high-LRV filtration requirements (more than 300% longer than equivalent cylinders) while the low-LRV operational lifetime is extended less than for the previous case. Moreover, is the geometry that improves better the energetic balances; and *iii)* sinus-corrugated tubular conduits improve the LRV_0 values by almost one logarithmic unit with respect to equivalent cylinders, and present extended operational lifetimes for both high- and low-LRV requirements (about 275% and 100% longer than equivalent cylinders, respectively). Furthermore, for the region far from the saturated regime, it keeps an energetic balance similar to the case of the cylinder.

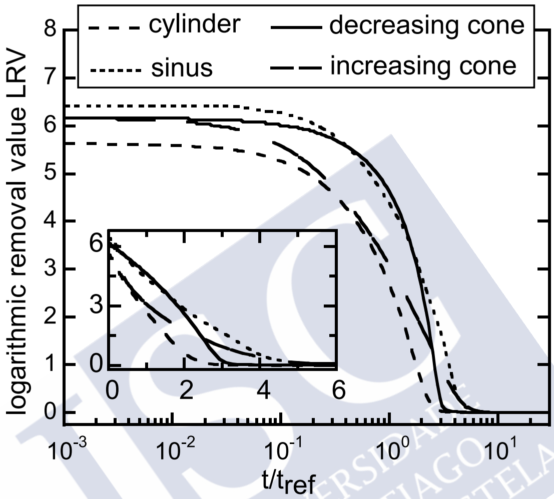

Figure 8.5: Logarithmic removal value LRV as a function of time resulting from our simulations of nanofunctionalized macropore conduits with different geometries and the same average nominal diameter 300 nm. Note that the cylinder leads to the lowest LRV_0 (defined as $\mathrm{LRV}(t = 0)$) and the lowest operational lifetimes (defined as the times at which the filtration performance reaches a certain LRV threshold; see also Table 8.2). Note also that the time axis is logarithmic and normalized by the same common reference time t_{ref} as in Figures 8.1 to 8.4 and Tables 8.1 and 8.2.

Our results also reveal that the nanoenhanced conduits get covered by trapped nanoimpurities at a faster pace in the regions with either smaller diameters or nearer to the entrance of the flow in the conduit. When both types of regions do not coincide in space, their competition may significantly increase some operational lifetimes. For example, when comparing increasing and decreasing conical macropores, in spite of having equal LRV_0, their time evolution is significantly different from each other (note, *e.g.*, their LRV$\geq$ 5 lifetimes in Table 8.2).

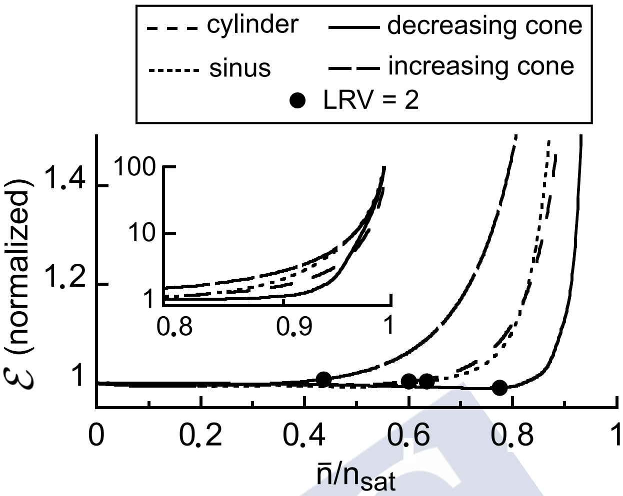

Figure 8.6: Hydrodynamic energy energy rate $\mathcal{E}$ obtained from our simulations of nanofunctionalized macropore conduits with different geometries and the same average nominal diameter 300 nm. Note again that $\overline{n}/n_{\rm sat}$ is proportional to the total number of trapped impurities n_{tot} (in particular, both $\overline{n}$ and $n_{\rm tot}$ are equal when normalized to their respective saturation values)

In consequence, our calculations suggest that a possible way to improve water nanofiltration using nanofunctionalized macropore media and membranes is to optimize the macropore shape so to achieve the desired characteristics (improved initial filtration performance, improved filtration lifetime, etc.). The proposed custom geometries seem to be well feasible in practice, given that they have been already attained by several groups in non-functionalized macropore media and membranes. [145–149] Finally, we remark that our methodology could be applied to study geometries different from the examples that have been considered in this thesis.

Final conclusions

Part I: A first-principles study of the interplays between structural and superconducting energies in cuprate superconductors

With the aim of obtaining new information about the pairing in high-temperature cuprate superconductors (HTS), we have extended the so-called Chester equations to be valid for polyatomic and type-I or II superconductors. These new extended-Chester equations provide relationships for the difference between the normal and the superconducting state of, mainly, the kinetic energy of the nucleus, the kinetic energy of the electrons, and the Coulomb interaction energy.

Then, we have applied these extended-Chester equations to available measurements in different HTS materials, to the case of cuprate HTS, obtaining information, *e.g.*, about the role of the kinetic energy of the oxygen nucleus in the superconductivity of these type of materials through the phase diagram. We have quantified the energetic balances using experimental data available for three typical cuprate superconductors. [24–28] Our results indicate that the phononic contribution is not doping-independent, but rather evidence three different regions in the phase diagram: In the underdoped side, we find that the kinetic energy savings of the oxygen nucleus favors the superconductivity. In contrast, in the slightly overdoped side the movement of the oxygen nucleus opposes to the superconductivity and, finally, in the highly overdoped side the nucleus contribution is almost negligible.

Part IIA: Some applied researches of micro- and nano-structured superconductors

We have analyzed three different (but related) cases in which micro and nanostructuration may serve to optimize the functional behavior of some superconducting devices.

First, we performed numerical computation to optimize the operational characteristics of radiation bolometric transition edge sensors based on high-temperature superconductors (HTS TES), through the consideration of nanostructuring and 1D-patterning of the doping level (and hence of the superconducting critical temperature T_c). Our results identify, for instance, that a certain discrete 4-step combination of nanostructured-doping zones may significantly improve the bolometric characteristics of HTS TES (*e.g.*, saturation power, operation temperature width, sensitivity).

Secondly, we have also presented numerical simulations of some 2D-patterned HTS films, demonstrating that, *e.g.*, such structuring may be tailored to sharpen the superconducting transition temperature-width (as desirable, *e.g.*, for some fault-current limiters).

Finally, for this part IIA, we presented experimental measurements og hybrid HTS+piezoelectric thin film devices, focusing on the characterization of the strain that can be induced by applying a transversal (piezo)voltage, on the so-induced shift of the critical temperature, and on the thermal fluctuation effects (paraconductivity) in such devices.

Part IIB: Some applied studies of functional nanofluid filters based on electrostatic nanostructured media

We have described theoretical and computational methods used to study the removal of nanoimpurities from liquids using filter media composed of pore conduits of micrometric diameter and nanostructured inner walls. Those methods are focused on the study of the influence of the conduit nominal geometry over filtration features such as the logarithmic removal value, the operational lifetimes and the energy performance. We also obtain the spatial profiles of the trapped-impurity layer in the inner walls of the conduits. Our results suggest, for instance, that decreasing-conical and sinusoidal-corrugated conduits have better initial trapping capability and longer operational lifetime (almost half an order of magnitude longer) than cylinders of the same average diameter. These geometries also improve the energy efficiency of the filtration (watts per spent removed nanoimpurity), with the decreasing-cone geometry particularly standing out in this respect.

Resumen en castellano

Esta tesis presenta investigaciones realizadas con financiación de la Xunta de Galicia y del Ministerio de Educación de España en forma de becas predoctorales. Ambas instituciones requirieron la inclusión de aspectos fundamentales y aplicados. De esta manera, el trabajo doctoral se compone de dos partes:

La **Parte I** presenta resultados novedosos obtenidos utilizando un estudio de primeros principios en materiales superconductores de alta temperatura (HTS), realizados en el contexto de una colaboración con el Profesor A.J. Leggett, en cuyo laboratorio realicé dos estancias doctorales.

El estudio presenta una extensión, para el caso de los HTS, de ecuaciones derivadas originalmente para superconductores simples por G.V. Chester. Estas ecuaciones ligan la energía ahorrada en la superconductividad con las propiedades estructurales de estos materiales. Después, aplicamos estas ecuaciones extendidas a varios HTS prototípicos.

La **Parte II** se centra en el el desarrollo de varios estudios aplicados en diferentes materiales funcionales y dispositivos micro y nanoestructurados. Hemos dividido estos estudios en dos partes: En la parte IIA, nos centramos de nuevo en HTS y proponemos diferentes diseños estructurales que optimizan su funcionalidad como sensores bolométricos de radiación (un desarrollo que ha dado lugar a la petición de la patente española con código P201930020) y también estudiamos otros sistemas HTS estructurados (filmes patroneados con puntos 2D; híbridos formados por filmes de HTS sobre sustratos piezoeléctricos).

En la parte IIB estudiamos medios microporosos electrostáticamente nanoestructurados de un tipo recientemente introducido en la industria de varias maneras (entre otras, membranas microporosas recubiertas con nanoalúmina) para la filtración de nanofluidos (líquidos que portan nanoentidades en suspensión). Empleando ecuaciones de un modelo previamente desarrollado en Santiago de Compostela, encontramos las diferentes configuraciones de microgeometrías que son capaces de optimizar la eficiencia energética y la capacidad de filtración de filtros basados en estos medios.

Presentamos ahora una breve pero más detallada introducción de los diferentes estudios fundamentales y aplicados realizados en este trabajo:

Parte I: Un estudio de primeros principios de las interacciones entre las energías estructurales y superconductoras en cupratos superconductores.

En contraste con lo que sucede con los superconductores clásicos, los superconductores BCS en los cuales hay un mecanismo fonónico que explica la formación de los pares de Cooper y que está bien aceptado y es profundamente entendido, [1] los cupratos superconductores de alta temperatura (y otros superconductores complejos fuertemente correlacionados) son todavía un puzle sin resolver en lo que respecta al mecanismo microscópico de apareamiento superconductor. [2, 3] Arrojar luz, aunque sea parcialmente en el descubrimiento de la naturaleza de estos mecanismos es de máximo interés. [4]

Probablemente, debido al éxito de la teoría BCS, la mayor parte de la comunidad centró sus intentos para explicar estos materiales no convencionales intentando introducir algún tipo de Hamiltoniano efectivo, describiendo el sistema en términos de unos pocos grados de libertad (a menudo diferentes en cada aproximación: fonónico, modelos magnéticos, etc.) que, esperanzadoramente, podrían dominar la amplia variedad de fenomenología medida para este tipo de superconductividad. [5–8] Sin embargo, hasta esta fecha, ninguna teoría ha destacado con un buen nivel de aceptación en la comunidad científica que sea capaz de explicar todas las propiedades relevantes de estos compuestos. Además, la mayor parte de estos superconductores son sistemas electrónicos complejamente correlacionados, lo que significa, entre otras características, que se espera que sea difícil, o incluso imposible, reducir el problema a un Hamiltoniano efectivo (por ejemplo, teniendo en cuenta la interacción Coulombiana de largo alcance, que se cree que juega un papel importante en los HTS). [2]

Todo esto lleva a pensar si este es el único camino para tratar de abordar este problema, o si se debe intentar alguna metodología alternativa.

Siguiendo esta línea de ideas, una aproximación diferente al problema es comenzar por un Hamiltoniano de primeros principios e intentar obtener las propiedades del superconductor de él. La solución exacta de todas las propiedades obtenidas mediante la mecánica estadística de estos sistemas es por supuesto imposible de conseguir con la potencia computacional que tenemos en la actualidad. Sin embargo, utilizando esta metodología es posible obtener resultados generales, pero no por ello menos importantes. [3, 9]

Una manera prometedora de encontrar información del Hamiltoniano general del sistema es centrarse en la evolución de los promedios energéticos termodinámicos cuando cambian del estado normal al estado superconductor. [9–12] La energía termodinámica básica a estudiar es el Hamiltoniano completo promediado térmicamente, definido como la energía interna U. Cuando un compuesto pasa el estado superconductor, su energía interna decrece, pues este nuevo estado minimiza U.

Además, el Hamiltoniano total del sistema es una suma de diferentes tipos de energías, siendo la manera más fácil de describirlo como una suma de todas las energías cinéticas de todas las partículas más la energía Colombiana de interacción entre todas las partículas cargadas. Sería también muy informativo conocer cómo cada una de estas contribuciones promediadas térmicamente evolucionan del estado normal al estado superconductor. De hecho, si fuésemos capaces de saber exactamente en qué lugares de esta suma se ahorra la energía que explica la energía de condensación superconductora, podríamos ser capaces de descartar teorías microscópicas que no dan lugar a ahorros energéticos en estas contribuciones, de manera que podríamos fijarnos en nuevas teorías teniendo esta información en cuenta.

Para los HTS, esta aproximación no es desconocida, y al menos hay un precedente parcialmente relacionado en la discusión entre diferentes grupos de algunos modelos teóricos [10–15] que exploran las interacciones interlaminares como posible origen de la transición superconductora en HTS. En particular, P.W. Anderson y sus colaboradores [13–15] propusieron el modelo de efecto túnel interlaminar (ILT) en el cual la condensación superconductora reduce la energía cinética de los electrones conductores que se mueven en la dirección perpendicular a los planos de CuO_2. Poco después, A.J. Leggett propuso un escenario en el que la transición superconductora puede explicarse a través de ahorros en la energía Coulombiana, siendo posiblemente dominados por el rango del espectro situado en el infrarrojo medio (el llamado escenario MIR). Esto dio lugar a una serie de comparaciones experimentales y teóricas [16–18] que principalmente obtuvieron que el ahorro de energía cinética de los electrones de conducción que se mueven entre los planos no es suficientemente fuerte como para explicar la energía de condensación de estos materiales, indicando entonces que el mecanismo ILT no parece ser el dominante en la condensación superconductora.

En diferentes ocasiones, varios grupos han centrado sus esfuerzos en la medida de estos ahorros energéticos entre el estado normal y el superconductor en los HTS. [16, 19–22] Por ejemplo, hubo intentos de medir el ahorro energético cinético total para los electrones de conducción en cupratos utilizando la regla de suma de “banda única” dentro de modelos de enlace fuerte. [22, 23] Estas medidas mostraron un comportamiento variado a lo largo del diagrama de fase de los cupratos: Para la parte muy sobredopada del diagrama de fase, la superconductividad incrementa esta energía cinetica; para la otra parte del diagrama de fase, la condensación viene acompañada de ahorros de la energía cinética que son suficientemente grandes como para explicar la energía de condensación. [22]

Una referencia particularmente relevante para nuestros propios esfuerzos en esta tesis es el escenario MIR introducido por A.J. Leggett, [10–12] construido sobre un Hamiltoniano de primeros principios cuyas propiedades se cree que son probablemente comunes a todos los HTS. [10–12] Dentro de estas suposiciones, Leggett introduce la posibilidad de un ahorro energético Coulombiano en la región del infrarrojo medio del espectro para los HTS. A pesar de los esfuerzos experimentales, [19–21] este escenario todavía no ha sido testado experimentalmente. Posibles nuevos estudios experimentales arrojarán algo de luz en la relevancia de este escenario.

Sin embargo, el Hamiltoniano introducido por A.J. Leggett, aunque es comparativamente bastante general, no es el Hamiltoniano exacto del sistema. Como ejemplo, no tiene en cuenta la energía cinética de los núcleos del sistema, que da información sobre el rol de los fonones en el mecanismo superconductor. Se ha vuelto bastante frecuente descartar este término del Hamiltoniano de los HTS debido a la idea general de que los fonones juegan un papel residual en el mecanismo superconductor. Esto sería coherente con una conjetura común que explica que la razón por la cual el efecto isotópico parece muy pequeño, pero apreciable para los cupratos con T_c máxima en su diagrama de fases, es que una hay una contribución BCS (fonónica) que contribuye de manera constante a la energía de condensación y es independiente del dopaje. Por lo tanto, el mecanismo BCS, y el efecto isotópico, serían despreciables cuando otros mecanismos más relevantes producen una T_c alta. Sin embargo, más allá de estos argumentos cualitativos, sigue faltando una prueba cuantitativa del papel del mecanismo fonónico en estos materiales.

En esta tesis, vamos a estudiar un método más general para obtener información sobre los cupratos superconductores, utilizando el Hamiltoniano total del sistema. Nuestro análisis se basa en el método introducido por primera vez por G.V. Chester en 1956, antes de la aparición de la teoría BCS, que se centra en el estudio de la evolución del estado normal al estado superconductor de los promedios térmicos de la energía cinética de los núcleos del sistema, la energía cinética de todos los electrones, y la energía Coulombiana de interacción entre todas las partículas cargadas. Como era común en aquella época, Chester asume en su trabajo el estudio para superconductores monoatómicos de tipo I. [9]

En nuestro estudio, adaptamos las ecuaciones de Chester para la obtención de las diferencias energéticas para extender su validez a un superconductor tipo II poliatómico genérico. Consecuentemente, empleamos un Hamiltoniano para materiales poliatómicos qe es una suma de tres términos, *i.e.*, a energía cinética de los núcleos del sistema, la energía cinética de todos los electrones, y la energía Coulombiana de interacción entre todas las partículas cargadas. Posteriormente extendemos para este caso poliatómico los tres teoremas empleados por Chester en su formalismo original. Además, expresamos estas ecuaciones en función de la energía de condensación del sistema, de manera que las ecuaciones de Chester extendidas también son válidas para superconductores de tipo II.

Posteriormente expresamos las ecuaciones en términos de magnitudes que han sido medidas para algunos HTS. Esto lleva a obtener, por ejemplo, a identificar los términos despreciables en las ecuaciones para los HTS y a obtener la ecuación para la variación de la energía cinética de los núcleos de oxígeno entre el estado normal y el superconductor en función de magnitudes medidas experimentalmente. De hecho, obtenemos los balances energéticos para tres cupratos prototípicos a lo largo de todo su diagrama de fase utilizando datos experimentales disponibles. [24–28] Nuestros resultados sugieren, por ejemplo, que hay un ahorro Coulombiano en la transición superconductora que dobla la energía de condensación. Esto está de acuerdo con el escenario MIR. Además, nuestros resultados también indican que la contribución fonónica no es independiente del dopaje, y de hecho hay evidencia de tres regiones diferentes en el diagrama de fases: en el lado subdopado, encontramos ahorros de energía cinética en los núcleos de oxígeno que favorecen la superconductividad. En contraste, en el lado levemente sobredopado el movimiento de los oxígenos se opone a la superconductividad, mientras que en el altamente sobredopado la contribución de los núcleos de oxígeno es casi despreciable.

Parte IIA: Algunas investigaciones aplicadas en superconductores micro- y nano-estructurados.

Como se comentó antes, el trabajo doctoral también está compuesto de estudios (la mayoría computacionales y/o experimentales) dedicados a la optimización de materiales funcionales usados como dispositivos o para otras aplicaciones. La primera parte de estos estudios se centra de nuevo en los HTS, mientras que la segunda parte se centra en materiales diferentes. En relación con los estudios aplicados en sistemas HTS, hemos dedicado una parte del trabajo a la optimización de dispositivos bolométricos detectores de radiación basados en HTS (lo cual ha dado lugar a la petición de la patente española con número P201930020). Además, hemos realizado dos estudios complementarios adicionales en filmes de HTS con patroneados 2D y en dispositivos híbridos basados en sustratos piezoeléctricos+filmes HTS. Introducimos a continuación brevemente estas tres contribuciones:

IIA.1- Optimización del diseño de bolómetros HTS utilizando nanoestructuración de dopaje y patroneado 1D.

Los bolómetros son sensores de radiación electromagnética que detectan la energía incidente a través del incremento de temperatura T causada por la absorción de los fotones que inciden en el dispositivo. Los sensores formados por una matriz de bolómetros de tamaños micrométricos (microbolómetros) son usualmente utilizados, *e.g.*, para cámaras infrarrojas, detectores en criptografía cuántica, astrofísica, satélites, aviación, etc, principalmente cuando los requerimientos de alta sensibilidad son mayores que el coste. [29–34] Los superconductores operando levemente por encima de la temperatura de transición T_c son de los candidatos más idóneos para bolómetros, por su extrema sensibilidad con la temperatura T en observables fáciles de medir como la resistencia eléctrica R (sensores de transición resistiva, TES), y también por su amplio rango espectral, rápida velocidad de respuesta, y otras características operacionales competitivas.

Una figura clave para estudiar la eficiencia de estos dispositivos es el denominado “coeficiente térmico de resistencia”, o TCR, dado por:

$$\mathrm{TCR} = \left| \frac{1}{R}\frac{\mathrm{d}R}{\mathrm{d}T} \right| .$$

Una sensibilidad bolométrica alta requiere valores altos de TCR. Los TES resistivos fabricados con superconductores de baja T_c (los denominados TES de baja T_c) consiguen TCR enormes ($\sim 1000\,\mathrm{K}^{-1}$) [29, 35] o incluso mayores (por comparación, el $\mathrm{V}_x\mathrm{O}_y$, el material más común y no superconductor utilizado para bolómetros baratos, posee un $\mathrm{TCR} \sim 0.025\,\mathrm{K}^{-1}$) [34]. Esto convierte a los TES de baja T_c en la elección tecnológica adecuada para medir las radiaciones más débiles, como la radiación de fondo de microondas. [29–31] Sin embargo, la necesidad de la utilización de sistemas criogénicos basados en helio líquido limita la extensión en la aplicación de los TES de baja T_c.

Después del descubrimiento de los HTS, varios autores han explorado su uso como sensores bolométricos (los denominados HTS TES) que poseen una criogenia más simple basada en nitrógeno líquido. [36–41] El $\mathrm{YBa}_2\mathrm{Cu}_3\mathrm{O}_{7-\delta}$ (YBCO) es el compuesto HTS más usado para esta aplicación, usualmente con dopaje que da lugar a la T_c máxima, *i.e.*, $\delta \sim 6.9$. Como se muestra en las Referencias [36–41], los filmes de YBCO proporcionan una competitividad viable respecto a los bolómetros basados en $\mathrm{V}_x\mathrm{O}_y$. No solo proporcionan un $\mathrm{TCR} \sim 1.5\,\mathrm{K}^{-1}$ muy superior, y menor ruido a su temperatura operacional $T \sim 90\,\mathrm{K}$, sino que también tienen una respuesta térmica mayor que los basados en $\mathrm{V}_x\mathrm{O}_y$. Además, el resto de los parámetros que contribuyen a una mayor sensibilidad (conductividad térmica, absorbancia en el infrarrojo, etc.) son también favorables o al menos competitivos con los bolómetros semiconductores. [36–41]

Sin embargo, los HTS TES propuestos hasta el momento todavía comparten algunas de las principales desventajas de los TES de baja T_c: Primero, la estabilidad térmica del baño criogénico es todavía un problema (pues los sistemas de nitrógeno líquido son más simples pero tienden a oscilar térmicamente más que los basados en helio líquido). Segundo, ambos tipos de TES tienen un T_cR válido únicamente en la temperatura de transición, con intervalos de temperatura operativos del orden de $0.1\,\mathrm{K}$ o menos para los TES de baja T_c, y de alrededor de $1\,\mathrm{K}$ para los HTS que se han propuesto hasta ahora. [36–41] Esto hace que sea fácil que se saturen (bajo régimen dinámico).

Los HTS TES propuestos hasta hoy son homogéneos en su composición nominal y temperatura crítica, [36–40] Sin embargo, en los años más recientes se han desarrollado diferentes técnicas para la imposición de patrones regulares de HTS en filmes, creando diseños a medida, hasta las escalas micro- y nanométricas. [42–47] Este tipo de nanoestructuraciones de HTS se ha convertido en uno de los principales objetos de estudio de dos sucesivas acciones COST europeas (NanoSC y NANOCOHYBRI, [46]).

Sin embargo, hasta donde nosotros sabemos, ningún autor ha considerado hasta la fecha la posibilidad de imponer un diseño de un patrón nanoestructurado con el objetivo de mejorar las características operacionales de un bolómetro basado en un filme de YBCO.

Hemos estudiado esta posibilidad utilizando principalmente métodos computacionales. Para ello, proponemos mejoras de los microbolómetros HTS TES resistivos considerando el uso de nanoestructuraciones y patroneados del dopaje local p (el número de portadores por celda unidad). En particular, en nuestros cálculos consideraremos el HTS prototípico YBCO, en el cual el dopaje local p se puede variar fácilmente cambiando la estequiometría de oxígeno δ (*e.g.*, mediante desoxigenación local, bombardeo de iones utilizando diferentes máscaras, etc.), y nos centramos en patroneados 1D (*i.e.*, p, o δ, variando a lo largo de una dirección). Nos centramos en obtener un incremento del intervalo de temperatura operacional, ΔT, en el cual i) el TCR es grande y ii) R es lineal con T (*i.e.*, $\mathrm{d}R/\mathrm{d}T$ es constante con T, que es otra característica deseable que simplifica tanto el control electrónico del microbolómetro como la estabilidad del dispositivo criogénico). Proponemos varios diseños de patroneados que mejoran sucesivamente tanto ΔT com TCR (y también otros parámetros bolométricos). Nuestro diseño más optimizado obtiene un muy competitivo TCR $\sim 5\,\mathrm{K}^{-1}$ y $T \sim 13\,\mathrm{K}$ (y ha dado lugar a la petición de la patente española con código P201930020).

IIA.2- Modificación de la anchura de la transición resistiva de filmes HTS utilizando patroneados de puntos 2D de T_c.

Los estudios comentados previamente sobre patroneados 1D en filmes HTS se suplementan en esta tesis con dos estudios complementarios. El primero está diseñado para enseñar que la forma de la transición resistiva en un filme de HTS puede ser también modificada a medida usando un patroneado 2D (en vez del más simple, pero efectivo, patroneado 1D usado previamente). De nuevo utilizamos principalmente aproximaciones computacionales, y en este caso nos centramos en obtener el efecto contrario sobre la transición encontrado previamente con las patroneados 1D: Ahora buscamos la posibilidad de un estrechamiento de la transición (disminuyendo ΔT) en vez de ensanchándola. Esto puede ser de interés para algunos dispositivos aplicados, como super-termómetros (sensibles en una pequeña ventana de temperaturas T) [48] o limitadores de corriente resistivos (dado que ΔT puede influenciar tanto la ocurrencia como la velocidad de las avalanchas térmicas y por lo tanto su habilidad para responder a subidas de corriente ultrarrápidas y su tiempo de recuperación). [49, 50]

Nuestros resultados en este estudio indican que el estrechamiento de la transición resistiva puede obtenerse a través de ciertos patroneados 2D con variaciones de T_c. Nuestros diseños más optimizados decrecen ΔT alrededor de un 75% frente a los filmes de YBCO no estructurados (y presumiblemente disminuirían en una cantidad similar el tiempo de respuesta de un limitador de corriente resistivo).

IIA.3- Dispositivos superconductores formados por sustratos piezoeléctricos+ filmes HTS.

Nuestro segundo estudio complementario de HTS tratados como materiales funcionales es un trabajo experimental. Hemos realizado varias medidas y caracterizaciones de dispositivos híbridos formados por piezoeléctricos+HTS. Estos sistemas, fabricados en nuestro grupo de investigación en Santiago de Compostela, consisten en una capa de YBCO de alrededor de 100 nm de grosor crecida encima de un monocristal del piezoeléctrico $\mathrm{Pb(Mg_{1/3}Nb_{2/3})_{0.72}Ti_{0.28}O_3}$. Hemos depositado contactos eléctricos a ambos lados de los híbridos, permitiéndonos aplicar voltaje sobre el piezoeléctrico a medida, que produce un cambio a medida en la tensión que se ejerce sobre el HTS. Debido a que la tensión induce un cambio en la T_c en estos superconductores, esto abre un camino para estudiar (y/o funcionalmente utilizar) la variación de la T_c con la simple aplicación de un voltaje externo.

Nos hemos centrado en la caracterización de la tensión que puede ser inducida aplicando un (piezo)voltaje transversal, en el salto inducido en la temperatura crítica, y en los efectos de las fluctuaciones térmicas (paraconductividad) en estos dispositivos.

Parte IIB: Algunos estudios aplicados de filtros de nanofluidos basados en medios electrostáticos nanoestructurados.

La parte IIB de esta tesis cambia el foco de los materiales y dispositivos superconductores, y en vez de eso fija un tema diferente en el campo de los materiales funcionales micro- y nano-estructurados. Esta temática diversa es un requerimiento de los organismos que han financiado este trabajo. Específicamente, estudiamos materiales microporosos electropositivamente nanoestrucrurados, de un tipo que ha sido introducido recientemente en al investigación académica [51–57] y que ya se ha comercializado en la industria [58–60] como medio adecuado para la filtración eficiente de nanofluidos (*i.e.*, la eliminación de nanoimpurezas que forman parte de una suspensión fluida que pasa por un medio microporoso electrostáticamente nanoestructurado). Nuestro objetivo específico en este estudio ha sido encontrar micro-geometrías que optimizan la eficiencia de la nanofiltración y la eficiencia energética (tos objetivos que no son necesariamente equivalentes). Para ello, hemos empleado un modelo teórico desarrollado en la 2013 en nuestro grupo de investigación en Santiago de Compostela [61] que proporciona una explicación cuantitativa para el incremento observado en la eficiencia de filtración. [51–60] Específicamente, computamos numéricamente las ecuaciones de este modelo (discretizado también en esta tesis) para obtener las características de filtración para diferentes microgeometrías, buscando aquellas que proporcionan o bien mejor porcentaje de filtración de nanoimpurezas, o mejor eficiencia energética por impureza filtrada. Este primer parámetro es de interés obvio para algunas de las aplicaciones en las cuales estos medios están siendo comercializados (eliminación de virus, filtración de agua para beber, eT_c.) mientras que para otras aplicaciones es más interesante optimizar el segundo parámetro (eficiencia energética es de vital importancia, *e.g.*., para efluentes industriales a larga escala).

Nuestros resultados indican, por ejemplo, que los conos decrecientes y los microconductos corrugados sinusoidalmente tienen una mejor tasa de eliminación de nanoimpurezas (y mayor tiempo de vida operacional, para los criterios standard) que el encontrado en el caso simple de conductos cilíndricos. Estas geometrías también incrementan la eficiencia energética de la filtración (Watts por nanoimpureza filtrada), sobre todo en el caso de la geometría de cono decreciente.


USC
UNIVERSIDADE
DE SANTIAGO
DE COMPOSTELA

Bibliography

[1] Bardeen, J.; Cooper, L.N.; Schrieffer, J.R. Microscopic Theory of Superconductivity. *Phys. Rev.* **1957**, *106*, 162-164.

[2] Leggett, A.J. Quantum Liquids. Bose Condensation and Cooper Pairing in Condensed-Matter Systems. Oxford University Press. **2006**, Chapter 7.8, 323-324.

[3] M. Tinkham, *Introduction to Superconductivity*, 2nd edition McGraw-Hill, New York, **1996**.

[4] Keimer, B.; Kivelson, S.A.; Norman, M.R.; Uchida, S.; J. Zaanen, J. From quantum matter to high-temperature superconductivity in copper oxides. *Nature*, **2015**, *518*, 179-186.

[5] Batista, C.D.; Aligia, A.A. Effective Hamiltonian for cuprate superconductors. *Phys. Rev. B*, **1993**, *47*, 8929-8935.

[6] Aji, V.; Varma, C.M. Spin order accompanying loop-current order in cuprate superconductors. *Phys. Rev. B*, **2007**, *75*, 224511-1–6.

[7] Wagner, J. Optical, magnetic, and single-particle excitations in the multiband Hubbard model for cuprate superconductors. *Phys. Rev. B*, **1991**, *43*, 10517-10529.

[8] Shih, C.T.; Lee, T.K.; Eder, R.; Mou, C.Y.; Chen, Y.C. Enhancement of Pairing Correlation by t' in the Two-Dimensional Extended t-J Model. *Phys. Rev. Lett.* **2004**, *92*, 227002-1–4.

[9] Chester, G.V.; Difference between normal and Superconducting States of a Metal. *Phys. Rev.* **1956**, *103*, 1693-1699.

[10] Leggett, A.J. Midinfrared" Scenario for Cuprate Superconductivity, *Proc. Natl. Acad. Sci. U.S.A.* **1999**, *96*, 8365-8372.

[11] Leggett, A.J., Cuprate Superconductivity: Dependence of T c on the c-Axis Layering Structure. *Phys. Rev. Lett.*, **1999** *83*, 392-395.

[12] Leggett, A.J., WHERE Is the Energy Saved in Cuprate Superconductivity?, *J. Phys. Chem. Solids*, **1998**, *59*, 1729-1732.

[13] Wheatley, J.; Hsu, T.; Anderson, P.W. Interlayer effects in High-Tc Superconductors. *Nature*, **1988**, *333*, 121.

[14] Chakravarty, S.; Sudbo, A.; Anderson, P.W.; Strong, S. Interlayer Tunneling and Gap Anisotropy in High-Temperature Superconductors. *Science*, **1993**, *261*, 337-340.

[15] Anderson, P.W. The Theory of Superconductivity. *Physica C*, **1991**, *185-189*, 185-189.

[16] Ramallo, M.V. On the energy saved by interlayer interactions in the superconducting state of cuprates *Europhys. Lett.* **2004**, *65*, 249-255.

[17] Leggett, A.J.; lnterlayer Tunneling Models of Cuprate Superconductivity: Implications of a Recent Experiment. *Science*, **1996**, *274*, 587-589.

[18] Schültzmann, J.; Somal, H.S.; Tsvetkov, A.; van der Marel, D.; Koops, G.E.J.; Koleshnikov, N.; Ren, Z.F.; Wang, J.H.; Brück, E.; Menovsky, A.A. Experimental test of the interlayer pairing models for high-T_c superconductivity using grazing-incidence infrared reflectometry. *Phys. Rev. B* **1997**, 55, 11118-11121.

[19] Levallois, J.; Tran, M.K.; Pouliot, D.; Presura, C.N.; Greene, L.H.; Eckstein, J.N.; Uccelli, J.; Giannini, E.; Gu, G.D.; Leggett, A.J.; van der Marel, D. Temperature-Dependent Ellipsometry Measurements of Partial Coulomb Energy in Superconducting Cuprates. *Phys. Rev. X.* **2016**, *6*, 031027-1–24.

[20] Husain, A.; Mitrano, M.; Rak, M.S.; Rubeck, S.; Uchoa, B.; Schneeloch, J.; Zhong, R.; Gu, G.; Abbamonte, P. Crossover of Charge Fluctuations across the Strange Metal Phase Diagram. *arXiv:1903.04038v1*, **2019**.

[21] Mitrano, M.; Husain, A.; Vig, S.; Kogar, A.; Rak, M.S.; Rubeck, S.; Schmalian, J.; Uchoa, B.; Schneeloch, J.; Zhong, R.; Gu, G.; Abbamonte, P. Anomalous density fluctuations in a strange metal. *Proc. Natl. Acad. Sci. U.S.A.* **2018**, *115*, 5392-5396.

[22] Carbone, F.; Kuzmenko, A.B.; Molegraaf, H.J.A.; van Heumen, E.; Lukovac, V.; Marsiglio, F.; van der Marel, D. Doping dependence of the redistribution of optical spectral weight in $Bi_2Sr_2CaCu_2O_{8+\delta}$.*Phys Rev. B*, **2006**, *74*, 064510-1–8.

[23] Marsiglio, F. Sum rule anomaly from suppression of inelastic scattering in the superconducting state. *Phys. Rev. B*, **2006**, *73*, 064507-1–7.

[24] Tallon, J.L.; Williams, G.V.M.; Loram, J.W. Factors affecting the optimal design of high-T c superconductors - the pseudogap and critical doping. *Physica C*, **2000**, *338*, 9-17.

[25] Loram, J.W.; Luo, J.L.; Cooper, J.R.; Liang, W.Y.; Tallon, J.L. The Condensation Energy and Pseudogap Energy Scale of Bi:2212 from the Electronic Specific Heat.*Physica C*, **2000**, **341-348**, 831-834.

[26] Momono, N.; Matsuzaki, T.; Oda, M.; Ido, M. Superconducting Condensation Energy and Pseudogap Formation in $La_{2-x}Sr_xCuO_4$: New Energy scale for Superconductivity. *Journal of the Physical Society of Japan*, **2002**, *71*, 2832-2835.

[27] Pringle, D.J.; Williams, G.V.M.; Tallon, J.M. Effect of doping and impurities on the oxygen isotope effect in high-temperature superconducting cuprates. *Phys. Rev. B*, **2000**, *62*, 12527-12533.

[28] Mourachkine, A. The oxygen isotope effect on critical temperature in superconducting copper oxides. *Supercond. Sci. Technol.* **2004**, *17*, 721-723.

[29] Zadeh, I.E.; Los, J.W.N.; Gourggues, R.B.M.; Steinmetz, V.; Bulgarini, G.; Dobrovolskiy, S.M.; Zwiller, V.; Dorenbos, S.N. Single-photon detectors combining high efficiency, high detection rates, and ultrahigh timing resolution. *Appl. Phys. Lett. Photonics* **2017**, *2*, 111301-1–7.

[30] Jankovi; L.; Gournis, D.; Trikalitis, P.N.; Arfaoui, I.; Cren, T.; Rudolf, P.; Sage, M.H.; Palstra, T.T.M.; Kooi, B; De Hosson, J.; Karakassides, M.A.; Dimos, K.; Moukarika, A.; Bakas, T. Carbon Nanotubes Encapsulating Superconducting Single-Crystalline Tin Nanowires. *Nano Lett.* **2006**, *6*, 1131-1135.

[31] Ma, X.; Hartmann, N.F.; Baldwin, J.K.S.; Doorn, S.K.; Htoon, H. Room-temperature single-photon generation from solitary dopants of carbon nanotubes. *Nat. Nanotech.* **2015**, *10*, 671-675.

[32] Eaton, H.A.C. Observing Photons in Space, chapter 29. In *Infrared imaging bolometers* Volume 9, AG of the series ISSI Scientific Report Series. Huber, C. E.; PauluhnJ, A.; CulhaneJ, L.; TimothyKlaus, G.; Zehnder, W. Springer: Switzerland, **2013**, 515-524.

[33] Golt'sman, G.N.; Okunev, O.; Chulkova, G.; Lipatov, A.; Semenov, A.; Smirnov, K.; Voronov, B.; Dzardanov, A.; Williams, C.; Sobolewski, R. Picosecond superconducting single-photon optical detector. *Appl. Phys. Lett.* **2001**, *79*, 705-707.

[34] Abdel-Rahman, M.; Ilahi, S.; Zia, M.F.; Alduraibi, M.; Debbar, N.; Yacoubi, N.; Ilahi, B. Temperature coefficient of resistance and thermal conductivity

of Vanadium oxide 'Big Mac' sandwich structure. *Infrared Phys. & Technol.* **2015**, 71, 127-130.

[35] Bonetti, J.A.; Day, P.; Kenyon, M.; Turner, A.; LeDuc, H.G.; Kuo, C.L.; Bock, J.J. Electrical and Thermal Characterization of Membrane-Isolated, Antenna-Coupled, TES Bolometers for the SPIDER Experiment. *J. Low Temp. Phys.* **2008**, *151* 138-143.

[36] Kaila, M.M. Theoretical Analysis of Responsivity of a High Temperature Superconductor (HTSC)-Hot Electron Far Infrared Bolometer (HEFIB). *J. Superond. and Nov. Mag.* **2001**, *14*, 569-573.

[37] Khrebtov, I.A. Noise Properties of High Temperature Superconducting Bolometers. *Fluctuation and Noise Letters* **2002**, *2*, 51-69.

[38] Kaiser, G.; Thurk, M.; Seidel, P. Signal-to-noise ratio improvement of HTSC bolometers for cryocooler operation using a thermal compensation principle. *Cryogenics* **1995**, *35*, 463-465.

[39] Khrebtov, I.A.; Tkachenko, A.D. High-Temperature superconductor bolometers for the IR region. *J. Opt. Technol.* **1999**, *66*, 735-741.

[40] Zhang, Z.M.; Frenkel, A. Thermal and Nonequilibrium Responses of Superconductors for Radiation Detectors. *Journal of Superconductivity* **1994**, *7*, 871-884.

[41] Wen, B.; Yakobov, R.; Vitkalov, S.A.; Sergeev, A. Superconducting cuprate heterostructures for hot electron bolometers. *Appl. Phys. Lett.* **2013**, *103*, 222601-1–5.

[42] Crassous, A.; Bernard, R.; Fusil, S.; Bouzehouane, K.; Bourdais, D.L.; Enouz-Vedrenne, S.; Briatico, J.; Bibes, M.; Barthélémy, A.; Villegas, J.E. Nanoscale electrostatic manipulation of magnetic flux quanta in ferroelectric/superconductor $BiFeO_3/YBa_2Cu_3O_{7-\delta}$ heterostructures. *Phys. Rev. Lett.* **2011**, 107, 247002-1–5.

[43] Katzer, C.; Stahl, C.; Michalowski, P.; Treiber, S.; Schmidl, F.; Seidel, P.; Albrecht, J.; SchÃ¼tz, G. Gold nanocrystals in high-temperature superconducting films: Creation of pinning patterns of choice. *New Journal of Physics* **2013** 15, 113029-1–12.

[44] Vestgården, J.I.;, Yurchenko, V.V.; Wördenweber, R.; Johansen, T.H. Mechanism for flux guidance by micrometric antidot arrays in superconducting films. *Phys. Rev. B* **2012**, 85, 014516-1–8.

[45] For instance, the International Workshop Advances in Nanostructured Superconductors: Materials, Properties and Theory, Madrid, Spain, May 2014; the Coherent Superconducting Hybrids and Related Materials, Les Arcs

1800, France, March 2018; the Workshop on vortex behavior in unconventional superconductors, Braga, Portugal, October 2018; the International conference on 'Nano confined superconductors and their application', Garmish, Germany, September 2016.

[46] Like the european networks NanoSC (http://nanosc-cost.eu) or NANOCOHYBRI (http://nanocohybri.eu).

[47] Verde, J.C.; Doval, J.M.; Ramos-Álvarez, A.; Sóñora, D.; Ramallo, M.V. Resistive Transition of High-T_c Superconducting Films With Regular Arrays of T_c-Domains Induced by Micro- or Nanofunctionalization. *IEEE Trans. Applied Supercond.* **2016**, 26, 8800204-1–4.

[48] Liebenberg, D.H.; Allen, L.D.F. Thin-film superconductors as sensitive thermometers, *J. Appl. Phys.*, **1970**, *41*, 4050-4053.

[49] Baldan, C.A.; Lamas, J.S.; Shigue, C.Y.; Ruppert, E. Test of a modular fault current limiter for 220V line using coated conductor tapes with shunt protection, *IEEE Trans. Appl. Supercond.*, **2011**, *21*, 1242-1245.

[50] Maza, J.; Ferro, G.; Veira, J.A.; F. Vidal, F. Transition to the normal state induced by high current densities in $YBa_2Cu_3O_{7-\delta}$ thin films: A thermal runaway account, *Phys. Rev. B*, **2008**, *78*, 094512-1–9.

[51] Wegmann, M.; Michen, B.; Graule, T.; Nanostructured surface modification of microporous ceramics for efficient virus filtration. *J. Eur. Ceram. Soc.* **2008**, *28*, 1603-1612.

[52] Wegmann, M.; Michen, B.; Luxbacher, T.; Fritsch, J.; Graule, T.; Modification of ceramic microfilters with colloidal zirconia to promote the adsorption of viruses from water. *Water Res.* **2008**, *42*, 1726-1734.

[53] Lv, Y.; Wang, Z.; Liu, S.; Hao, L.; Sang, Y.; Liu, D.; Wang, J.; Boughton, R.I. 2009 Silver nanoparticle-decorated porous ceramic composite for water treatment. *J. Membrane Sci.* **2009**, *331*, 50-56.

[54] Hambsch, B.; Bösk, M.; Eberhagen, I.; Müller, U.; Removal of bacteriophages with different surface charges by diverse ceramic membrane materials in pilot spiking tests. *Water Sci. and Technol.* **2012**, *66*, 151-157.

[55] Meder, F.; Wehling, J.; Fink, A.; Piel, B.; Ki, K.; Frank, K.; Rosenauer, A.; Treccani, L.; Koeppen, S.; Dotzauer, A.; Rezwan, K.; The role of surface functionalization of colloidal alumina particles on their controlled interactions with viruses. *Biomaterials* **2013**, *34*, 4203-4213.

[56] Yang, D.; Fan, T.; Zhang, D.; Zhu, J.; Wang, Y.; Du, B.; Yan, Y.; Biotemplated hierarchical porous material: the positively charged leaf. *Chem-Eur. J.* **2013**, *19*, 4742-4747.

[57] Yang, D.; Du, B.; Yan, Y.; Li, H.; Zhang, D.; Fan, T.; Rice-husk-templated hierarchical porous TiO_2/SiO_2 for enhanced bacterial removal. *ACS Appl. Mater. Inter.* **2014**, *6*, 2377-2385.

[58] Tepper, F.; Kaledin, L.; Kaledin, T.; Non-woven electrostatic media for chromatographic separation of biological particles. *J. Liq. Chromatogr. R. T.* **2009**, *32*, 607-627.

[59] Tepper, F.; Kaledin, L.; Nanostructured chem-bio non-woven filter. *Nanoscience and Nanotechnology for Chemical and Biological Defense* **2009**, 1016, 273-288.

[60] Theron, J.; Walker, J.A.; Cloete, T.E.; 2008 Nanotechnology and water treatment: applications and emerging opportunities. *Crit. Rev. Microbiol.* **2008**, *34*, 43-69.

[61] Ramallo, M.V.; An effective-charge model for the trapping of impurities of fluids in channels with nanostructured walls. *Nanoscale Res. Lett.* **2013**, *8*, 19-1–7.

[62] Frank, H.; Lancaster, R. Electropositive Filtration Technology in Automobile Manufacturing Applications. presented for *WQA-Aquatech 2008*, **2008**, Mandala Bay, Las Vegas, Nevada.

[63] van der Marel, D.; Leggett, A.J.; Loram, J.W.; Kirtley, J.R. Condensation energy and high-Tc uperconductivity *Phys. Rev. B* **2002**, *66*, 140501-1–4.

[64] Loram, J.W.; Luo, J.; Cooper, J.R.; Liang, W.Y.; Tallon, J.L. Evidence on the pseudogap and condensate from electronic specific heat. *Journal of Physics and Chemistry of Solids*, **2001**, em 62, 59-64.

[65] Luo, J.L.; Loram, J.W.; Cooper, J.R.; Tallon, J. Doping Dependence of Condensation Energy and Upper Critical Field in $Y_0.8Ca_0.2Ba_2Cu_30_{7-\delta}$ from Specific Heat Measurement. *Physica C*, **2000**, *341-348*, 1837-1840.

[66] Feynman, R.P. Forces in Molecules. *Phys. Rev.*, **1939**, *56*, 340-343.

[67] Bornemann, H.J.; Morris, D.E.; Liu, H.B.; Narwankar, P.K. Dependence of the oxygen isotope effect upon hole density in $Bi_2Sr_2Ca_{1-x}Y_xCu_2O_{8+\delta}$ and $Y_{1-x}Ca_x$ $Ba_2Cu_4O_8$. *Physica C*, **1992**, *191*, 211-218.

[68] Batlogg, B.; Kourouklis, G.; Weber, W.; Cava, R.J.; Jayaraman, A.; White, A.E.; Short, K.T.; Rupp, L.W.; Rietman, E. A. Nonzero Isotope Effect $La_{1.85}Sr_0.15CuO_4$ *Phys. Rev. Lett.* **1987**, *59*, 912-914.

[69] Bourne, L.C.; Zettl, A. Barbee, T.W.; Cohen, M.L. Complete absence of isotope effect in $YBa_2Cu_30_7$. Consequences phonon-mediated superconductivity. *Phys. Rev. B* **1987**, *36*, 3990-3993.

[70] Zech, D.; Conder, K.; Keller, H.; Kaldis, E.; Müller, K.A. Doping dependence of the oxygen isotope effect in $YBa_2Cu_3O_x$. *Physica B*, **1996**, *219 and 220*, 136-138.

[71] Franck, J.P.; Experimental Studies of the Isotope Effect in High Tc Superconductors. *Physica C*, **1997**, *282-287*, 198-201.

[72] Crawford M.K.; Farneth, W.E.; Mccarron, E.M.; Harlow, R.L.; Moudden, A.H. Oxygen Isotope Effect and Structural Phase Transitions in La_2CuO_4-Based Superconductors. *Science*, **1990**, *250*, 1390-1394.

[73] Chen, X.J.; Liang, B.; Ulrich, C.; Lin, C.T.; Struzhkin, V.V.; Wu, Z.; Hemley, R.J.; Mao, H.K.; Lin, H.Q. Oxygen isotope effect in $Bi_2Sr_2Ca_{n-1}Cu_nO_{2n+4+\delta}$ (n = 1 , 2 , 3...) single crystals. *Phys. Rev. B*, **2007**, *76*, 140502-1–4.

[74] Batlogg, B.; Cava, R.J.; Jayaraman, A.; Van Dover, R.B.; Kourouklis, G.A.; Sunshine, S.; Murphy, S.W.; Rupp, L.W.; Chen, H.S.; White, A.; Short, K.T.; Mujsce, A.M.; Rietman, E.A. Isotope Effect in the High-T_c Superconductors $Ba_2YCu_30_7$ and $Ba_2EuCu_3O_7$. *Phys. Rev. Lett.*, **1987**, *58*, 2333-2336.

[75] Franck, J.P.; Harker, S.; Brewer. J.H. Copper and Oxygen Isotope Effects in $La_{2-x}Sr_xCuO_4$. *Phys. Rev. Lett.* **1993**, *71*, 283-286.

[76] Zhao, G.M.; Kirtikar, V.; Singh, K.K.; Sinha, A.P.B.; Morris, D.E. Large copper isotope effect in oxygen depleted $YBa_2Cu_3O_y$: Importance of Cu-dominated phonon modes in the pairing mechanism. *Phys. Rev. B*, **1996**, *54*, 14956-14959.

[77] Franck, J.P.; Lawrie, D.D. The Copper Isotope Effect in Oxygen-Deficient $YBa_2Cu_3O_{7-\delta}$. *Journal of Superconductivity*, **1995**, *8*, 591-594.

[78] Soddy, F. The Atomic Volume of Isotopes. *Nature*, **1921**, *107*, 41-42.

[79] Pasler, V.; Schweiss, P.; Meingast, C. 3D-XY Critical Fluctuations of the Thermal Expansivity in Detwinned $YBa_2Cu_3O_{7-\delta}$ Single Crystals Near Optimal Doping. *Phys. Rev. Lett.* **1998**, *81*, 1094-1097.

[80] Bandyopadhyay, J.; Gupta, K.P. Low temperature lattice parameter of nickel and some nickel-cobalt alloys and Grfineisen parameter of nickel. *Cryogenics*, **1977**, 345-347.

[81] Paszkowicz, W.; Piszora, P.; Lasocha, P.; Margiolaki, I.; Brunelli, M. Fitch, A. Lattice Parameter of Polycrystalline Diamond in the Low-Temperature Range. *Acta Physica Polonica A*, **2010**, *117*, 323- 327.

[82] Mouallem-Bahout, M.; Gaudé, J.; Calvarin, G.; Gavarri, J.R.; Care, C. Anisotropic thermal expansion and Griineisen coefficients of the bismuth cuprate 2-2-1-2. *Materials Letters*, **1994**, *18*, 181-185.

[83] Williams, G.V.M.; Tallon, J.L.; Quilty, J.W.; Trodahl, H.J.; Flower, N.E. Absence of an Isotope Effect in the Pseudogap in $YBa_2Cu_4O_8$ as Determined by High-Resolution ^{89}Y NMR. *Phys. Rev. Lett.*, **1998**, *80*, 377-380.

[84] Raffa, F.; Ohno, T.; Mali, M.; Roos, J.; Brinkmann, D.; Conder, K.; Eremin, M. Isotope Dependence of the Spin Gap in $YBa_2Cu_4O_8$ as Determined by Cu NQR Relaxation. *Phys. Rev. B.*, **1998**, *26*

[85] Temprano, D.R.; Mesot, J.; Janssen, S.; Conder, K.; Furrer., A. Large Isotope Effect on the Pseudogap in the High-Temperature Superconductor $HoBa_2Cu_4O_8$. *Phys. Rev. Lett.* **2000**, *84*, 1990-1993.

[86] Temprano, D.R.; Conder, K.; Furrer, A.; Mutka, H.; Trounov, V.; Müller, K.A. Oxygen and copper isotope effects on the pseudogap in the high-temperature superconductor $La_{1.81}Ho_{0.04}Sr_{0.15}CuO_4$ studied by neutron crystal-field spectroscopy. *Phys. Rev. B*, **2002**, *66*, 184506-1–4.

[87] Bud'ko, S.L.; Lapertot, G.; Petrovic, C.; Cunningham, C.E.; Anderson, N.; Canfield, P.C. Boron Isotope Effect in Superconducting MgB2. *Phys. Rev. Lett.*, **2001**, *86*, 1878-1880.

[88] M.V. Ramallo, J.C. Verde, N. Cotón and F. Vidal, *Non-Ohmic Electrical Transport in the Vicinity of the Superconducting Transition: Implications for the Study of the Phase Diagram of the Underdoped Cuprate Superconductors*, *J. Supercond. Nov. Magn.* **2014**, *28*, 323..

[89] Verde, J.C., Ramallo, M.V. Herramientas computacionales en el laboratorio LBTS. In *Películas micro- y nanoestructuradas de superconductores de alta temperatura: Computación de su transición resistiva.* GIDFI. ISBN: 978-1-68073-062-3 Santiago de Compostela, Spain, **2016**, 39-47.

[90] Oktem, B.; Bozbey, A.; Avci, I.; Tepe, M.; Abukay, D.; Fardmanesh, M. The superconducting transition width and illumination wavelength dependence of the response of MgO substrate YBCO transition edge bolometers. *Physica C* **2007**, *458*, 6-11.

[91] Maza, J., Vidal, F. Critical-temperature inhomogeneities and resistivity rounding in copper oxide superconductors. *Phys. Rev. B.* **1991**, *43*, 10560.

[92] Solov'ev, A.L.; Dmitriev, V.M. Fluctuation conductivity and pseudogap in YBCO high-temperature superconductors (Review). *Low Temp. Phys.* **2009**, *35*, 169-197.

[93] Gallardo, M.C.; Burriel, R.; Romero, F.J.; Gutiérrez, F.J.; Salje, E.K.H. Low-temperature calorimetric study of SrTiO_3. *J. Phys.: Condens. Matter* **2002**, *14*, 1881-1886

[94] Yu, C.; Scullin, M.L.; Ramamoorthy, M.H.; Majumdar, A. Thermal conductivity reduction in oxygen-deficient strontium titanates. *Appl. Phys. Lett.* **2008**, *92*, 191911

[95] Richards, P.L. Bolometers for intrarred and millimeter waves. *J. Appl. Phys.* **1994**, *1*, 1.

[96] Barišić, M.; Chan, M.K.; Li, Y.; Yu, G.; Zhao, X.; Dressel, M.; Smontara, A.; Greven, M. Universal sheet resistance and revised phase diagram of the cuprate high-temperature superconductors. *PNAS* **2013**, 110, 12235-12240.

[97] Barišić, N.; Badoux, S.; Chan, M.K.; Dorow, C.; Tabis, W.; Vignolle, B.; Yu, G.; Béard, J.; Zhao, X.; Proust, C.; Greven, M. Universal quantum oscillations in the underdoped cuprate superconductors. *Nat. Phys.* **2013**, *9*, 761-764.

[98] Tafti, F.F.; Laliberté, F.; Dion, M.; Gaudet, J.; Fournier, P.; Taifeller, L. Nernst effect in the electron-doped cuprate superconductor $Pr_{2-x}Ce_xCuO_4$: Superconducting fluctuations, upper critical field H_{c2}, and the origin of the T_c dome. *Phys. Rev. B* **2014** *90* 024519-1–14.

[99] Carballeira, C.; Currás, S.R.; Viña, J.; Veira, J.A.; Ramallo, M.V.; Vidal, F. Paraconductivity at high reduced temperatures in $YBa_2Cu_3O_{7-\delta}$ superconductors. *Phys. Rev. B* **2001**, *63*, 144515-1–7.

[100] Ramallo, M.V.; Pomar, A.; Vidal, F. In-plane paraconductivity and fluctuation-induced magnetoconductivity in biperiodic layered superconductors: Application to $YBa_2Cu_3O_{7-\delta}$. *Phys. Rev. B.* **1996**, *54*, 4341-4356.

[101] Mosqueira, J.; Ramallo, M.V.; Recolevschi, A.; Torrón, C.; Vidal, F. Crossing point of the magnetization versus temperature curves and the Meissner fraction in granular $La_{1.9}Sr_{0.1}CuO_4$ superconductors: Random orientation and inhomogeneity effects. *Phys. Rev. B* **1999**, *59*, 4394-4403.

[102] Cotón, N.; Ramallo, M.V.; Vidal, F. Effects of critical temperature inhomogeneities on the voltage-current characteristics of a planar superconductor near the Berezinskii-Kosterlitz-Thouless transition. *Supercond. Sci. Technol.* **2011**, *24*, 085013-1–8.

[103] Cotón, N; Mercey, B.; Mosquiera, J.; Ramallo, M.V.; Vidal, F. Synthesis from separate oxide targets of high quality $La_{2-x}Sr_xCuO_4$ thin films and dependence with doping of their superconducting transition width. *Supercond. Sci. Technol.*, **2013**, *26*, 075011-1–11.

[104] Lawrence, W.E.; Doniach, S. in Proceedings of the Twelfth International Conference on Low-Temperature Physics, Kyoto, Japan, 1970, edited by E. Kanda Keigatu, Tokyo, **1971**, p. 361

[105] Ying, Q.Y.; Kwook, H.S. Kosterlitz-Thouless transition and conductivity fluctuations in Y-Ba-Cu-O thin films. *Phys. Rev. B* **1990**, *42*, 2242-2247.

[106] Cotón, N.; Ramallo, M.V.; Vidal, F. Critical temperatures for superconducting phase-coherence and condensation in $La_{2-x}Sr_xCuO_4$. *arXiv:1309.5910v3*, **2013**.

[107] Halperin, B.I.; Nelson, D.R. Resistive Transition in Superconducting Films. *J. Low Temp. Phys.* **1979**, *36*, 599-616.

[108] Mosqueira, J.; Cabo, L.; Vidal, F. Structural and T_c inhomogeneities inherent to doping in $La_{2-x}Sr_xCuO_4$ superconductors and their effects on the precursor diamagnetism. *Phys. Rev. B* **2009**, 214527-1–8.

[109] Mihailovic, D.; Optical experimental evidence for a universal length scale for the dynamic charge inhomogeneityy of cuprate superconductors. *Phys. Rev. Lett.* **2005**, *94*, 201001-1–4.

[110] See, *e.g.*, Electrical Transport and Optical Properties of Inhomogeneous Media, Ed by Garland, J.C. and Tanner, B. D. AIP, New York, USA, **1978**, 2.

[111] Covington, M.; Scheuerer, R.; Bloom, K.; Greene, L.H. Tunneling and anisotropic charge transport properties of superconducting oriented $YBa_2Cu_3O_7$ thin films *Appl. Phys. Lett.* **1996**, *68* 1717-1719.

[112] Caprara, S.; Grilli, M.; Benfatto, L.; Castellani, C. Effective medium theory for superconducting layers: A systematic analysis including space correlation effects. *Phys. Rev. B*, **2011**, *84*, 014514-1–11.

[113] Tallon, J.L.; Bernhard, C.; Shaked, H. Generic superconducting phase behavior in high-T_c cuprates: T_c variation with hole concentration in $YBaCu_3O_{7-\delta}$ *Phys. Rev. B.* **1995**, *51*, 12911-12914.

[114] Seebe, B. Ed., *Handbook of applied superconductivity*, Bristol, UK: Institute of Physics Publishing, **1998**.

[115] Braginski, A.I. Superconducting electronics coming to market, *IEEE Trans. Appl. Supercond.*, **1999**, *9*, 2825-2836.

[116] Baselmans, J.J.A.; Hajenius, M.; Gao, J.R.; Baryshev, A.; Kooi, J.; Klapwijk, T.M.; Voronov, B.; de Korte, P.; Gol'tsman, G. NbN hot electron bolometer mixers: Sensitivity, LO power, direct detection and stability, *IEEE Trans. Appl. Supercond.*, **2005**, *15*, 484-489.

[117] Ramallo, M.V.; Vidal, F. On the width of the full-critical region for thermal fluctuations around the superconducting transition in layered superconductors, *Europhys. Lett.*, **1997**, *9*, 177-182.

[118] Torrón, C.; Díaz, A.; Jegoudez, J.; Ramallo, M.V.; Revcolevschi, A.; Veira, J.A.; Vidal, F. Measurements of the magnetic susceptibility above the superconducting transition of $Y_1Ba_2Cu_3O_{7-\delta}$ single crystals in the weak magnetic field limit, *Physica C*, **1993**, *212*, 440-450.

[119] Pomar, A.; Ramallo, M.V.; Maza, J.; Vidal, F. Measurements of the fluctuation-induced magnetoconductivity in the *a*-direction of an untwinned $Y_1Ba_2Cu_3O_{7-\delta}$ single crystal in the weak magnetic field limit, *Physica C*, **1994**, *225*, 287-293.

[120] Vidal, F.; Ramallo, M.V. Multilayering effects on the thermal fluctuations of Cooper pairs around the superconducting transition in cuprates, in *The gap symmetry and fluctuations in high-T_c superconductors*, J. Bok *et al.*, Eds. New York, NY, USA: Kluwer **1998**, 443-464.

[121] Viña, J.; Campá, J.A.; Carballeira, C.; Currás, S.R.; Maignan, A.; Ramallo, M.V.; Rasines, I.; Veira, J.A.; Wagner, P.; Vidal, F. Universal behavior of the in-plane paraconductivity of cuprate superconductors in the short-wavelength fluctuation regime, *Phys. Rev. B*, **2002**, *65*, 212509-1–4.

[122] Burlachkov, L.; Mogilko, E.; Schlesinger, Y.; Strelniker, Y. M.; Havlin, S. Resistive transition anisotropy in superconducting granular ceramics: Interplay of effective medium approximation and percolation, *Phys. Rev. B*, **2003**, *63*, 104509-1–9.

[123] Schilling, J.S. Handbook of High-Temperature Superconductivity. Theory and Experiment. Springer Science + Business Media, LLC. **2007**. Editors: Schrieffer, J.R.; Brooks, J.S. Chapter 11.

[124] Tomita, T.; Schilling, J.S.; Chen, L.; Veal, B.W.; Claus, H. Enhancement of the Critical Current Density of $YBa_2Cu_3O_x$ Superconductors under Hydrostatic Pressure. *Phys. Rev. Lett.* **2006**, *96*, 077001-1–4.

[125] Hardy, F.; Hillier, N.J.; Meingast, C.; Colson, D.; Li, Y.; BariÅ¡iÄ‡, N.; Yu, G.; Zhao, X.; Greven, M.; Schilling J.S. Enhancement of the Critical Temperature of $HgBa_2CuO_{4+\delta}$ by Applying Uniaxial and Hydrostatic Pressure: Implications for a Universal Trend in Cuprate Superconductors. *Phys. Rev. Lett.*, **2010**, *105*, 167002-1–4.

[126] Welp, U.; Grimsditch, M.; Fleshler, S.; Nessler, W.; Downey, J.; Crabtree, W.; Guimpel, J. Effect of Uniaxial Stress on the Superconducting Transition in $YBa_2Cu_3O_7$. *Phys. Rev. Lett.* **1992**, *69*, 2130-2133.

[127] Locquet, J.P.; Perret, J.; Fompeyrine, J.; Mächler, E.; Seo, J.W.; Van Tendeloo, G. Doubling the critical temperature of $La_{1}.9Sr_{0}.1CuO_{4}$ using epitaxial strain. *Nature*, **1998**, *394*, 453-456.

[128] Zhaia, H.Y.; Chu, W.K. Effect of interfacial strain on critical temperature of $YBa_2Cu_3O_{7-\delta}$ thin films. *Appl. Phys. Lett.* **2000**, *76*, 3469-3471.

[129] Zhu, Y.; Tsai, C.F.; Wang, H. Atomic interface sequence, misfit strain relaxation and intrinsic flux-pinning defects in different $YBa_2Cu_3O_{7-\delta}$ heterogeneous systems. *Supercond. Sci. Technol.* **2013**, *26*, 025009-1–10.

[130] Pahlke, P.; Trommler, S.; Holzapfel, B.; Schultz, L.; Hühne, R. Dynamic variation of biaxial strain in optimally doped and underdoped $YBa_2Cu_3O_{7-\delta}$ thin films. *Journal Appl. Phys.* **2013**, *113*, 123907-1–6.

[131] Trommler, S.; Hühne, R.; Iida, K.; Pahlke, P.; Haindl, S.; Schultz, L.; Holzapfel, B. Reversible shift in the superconducting transition for $La_{1.85}Sr_{0.15}CuO_4$ and $BaFe_{1.8}Co_{0.2}As_2$ using piezoelectric substrates. *New journal of Physics*, **2010**, *12*, 103030-1–6.

[132] Trommler, S.; Molatta, S.; Hänisch, J.; Iida, K.; Schultz, L.; HÃ¼hne, R. Strain Dependence of Critical Fields–Studied on Piezoelectric Substrates. *IEEE Transac. on Applied Supercond.* **2015**, *25*, 8499404-1–4.

[133] Hühne, R.; D Okai, D.; Dörr, K.; Trommler, S.; Herklotz, A.;Holzapfel, B.; Schultz, L. Dynamic investigations on the influence of epitaxial strain on the superconducting transition in $YBa_2Cu_3O_{7-x}$. *Supercond. Sci. Technol.* **2008**, *21*, 075020-1–4.

[134] Meingast, C.; Wolf, T.; Kläser, M.; Müller-Vogt, G. Uniaxial pressure dependence of T_c in $(Y_{1-y}Ca_y)_1Ba_2Cu_3O_x$ single crystals via high-resolution thermal expansion *J. Low Temp. Phys.* **1996**, *105*, 1391-1396.

[135] Cabo, L.; Soto, F.; Ruibal, M.; Mosqueira, J.; Vidal, F. Anomalous precursor diamagnetism at low reduced magnetic fields and the role of T_c inhomogeneities in the superconductors $Pb_{55}In_{45}$ and underdoped $La_{1.9}Sr_{0.1}CuO_4$. *Phys. Rev. B*, **2006**, *73*, 184520-1–9.

[136] Mosqueira, J.; Dancausa, J.D.; Vidal, F. Diamagnetism above the superconducting transition in underdoped $La_{1.9}Sr_{0}.1CuO_{4}$: Chemical disorder versus phase incoherent superconductivity. *Phys. Rev. B*, **2011** *84*, 174518-1–12.

[137] Herklotz, A.; Plumhof, J.D.; Rastelli, A.; Schmidt, O.G.; Schultz, L.; Dörr, K. Electrical characterization of PMN-28%PT(001) crystals used as thin-film substrates. *J. Appl. Phys.* **2010**, *108*, 094101-1–7.

[138] Thiele, C.; K. Dörr, K.; Bilani, O.; Rödel, J.; Schultz, L. Influence of strain on the magnetization and magnetoelectric effect in $La_{0.7}A_{0.3}MnO_3$/PMN-PT(001) (A = Sr, Ca). *Phys. Rev. B*, **2007**, *75*, 054408-1–8.

[139] Park, J.H.; Lee, J.H.; Kim, M.G.; Jeong, Y.K.; Oak, M.A.; Jang, H.M.; Choi, H.J.; Scott, J.F. In-plane strain control of the magnetic remanence and cation-charge redistribution in $CoFe_2O_4$ thin film grown on a piezoelectric substrate. *Phys. Rev. B*, **2010**, *81*, 134401-1–6.

[140] Biegalski, M.D. Dörr, K.; Kim, D.H.; Christen, H.M. Applying uniform reversible strain to epitaxial oxide films. *Appl. Phys. Lett.* **2010**, *96*, 151905-1–3.

[141] O. Bilani-Zeneli, O.; Rata, A.D.; Herklotz, A.; Mieth, O.; Eng, L.M.; Schultz, L.; Biegalski, M.D.; Christen, H. M.; Dörr, K. $STiO_3$ on piezoelectric PMN-PT(001) for application of variable strain. *J. Appl. Phys.* **2008**, *104*, 054108-5.

[142] Levin, A.A.; Thiele, C.; Paufler, P.; Meyer, D. C. In-situ X-ray investigation of a $PbMg_{1/3}Nb_{2/3}O_3$-28%$PbTiO_3$ single-crystal plate in an external electric field. *Appl. Phys. A*, **2006**, *84*, 37-45.

[143] Levin, A.A.; Weibach, T.; Pommrich, A.I.; Bilani-Zeneli, O.; Meyer, D.C. In situ X-ray investigation of lattice strain in $SrTiO_3/La_{0.7}Sr_{0.3}MnO_3$ thin films induced by piezoelectric $PbMg_{1/3}Nb_{2/3}O_3$-28%$PbTiO_3$ substrate in an external electric field *Appl. Phys. A*, **2009**, *96*, 575-580.

[144] Rouquerol, J.; Avnir, D.; Fairbridge, C.W.; Everett, D.H.; Haynes, J.M.; Pernicone, N.; Ramsay, J.D.F.; Sing, K. S. W.; Unger, K. K. Recommendations for the characterization of porous solids (Technical Report) *Pure and Applied Chemistry.* **1994**, *66*, 1739-1758.

[145] Mehdizadeh, H.; Somo, S.I.; Bayrak, E.S.; Brey, E.M.; Cinar, A.; Design of Polymer Scaffolds for Tissue Engineering Applications. *Ind. Eng. Chem. Res.* **2015**, *54*, 2317-2328.

[146] Xu, Y.; Zhang, B.; Recent advances in porous Pt-based nanostructures: synthesis and electrochemical applications. *Chem. Soc. Rev.* **2014**, *43*, 2439-2450.

[147] Wharton, J.E.; Jin, P.; Sexton, L.T.; Horne, L.P.; Sherrill, S.A.; Mino, W.K.; Martin, C.R.; A Method for Reproducibly Preparing snthetic Nanopores for Resistive-Pulse Biosensors. **2007**, *8*, 1424-1430.

[148] Apel, P.Y.; Korchev, Y.E.; Siwy, Z.; Spohr, R.; Yoshida, M.; Diode-like single-ion track membrane prepared by electro-stopping. *Nucl. Instr. and Meth. in Phys. Res. B* **2001**, *184*, 337-346.

[149] Wu, X.; Rajaeskaran, R.; Martin, C. R.; An Alternating Current Electroosmotic Pump Based on Conical Nanopore Membranes. *ACS Nano.* **2016**, *10*, 4637-4643.

[150] Balhoff, M.T.; Wheeker, M.F.; A predictive Pore-Scale Model for Non-Darcy Flow in Porous Media. *SPE Journal* **2009**, *14*, 579-587.

[151] Veyskarami, M.; Hassani, A.H.; Ghazanfari, M.H.; Modeling of non-Darcy flow through anisotropic porous media: Role of pore space profiles. *Chem. Eng. Sci.* **2016**, *151*, 93-104.

[152] Thauvin, F.; Mohanty, K.K.; Network Modeling of Non-Darcy Flow Through Porous Media. *Transport Porous Med.* **1998**, *31*, 19-37.

[153] Wang, X; Thauvin, F.; Mohanty, K.K.; Non-Darcy flow through anisotropic porous media. *Chem. Eng. Sci.* **1999**, 54, 1859-1869.

[154] Ghosal, S.; Lubrication theory for electro-osmotic flow in a microfluidic channel of slowly varying cross-section and wall charge. *J. Fluid Mech.* **2002**, *459*, 103-128.

[155] Ghosal, S.; The effect of wall interactions in capillary-zone electrophoresis. *J. Fluid Mech.* **2003**, *491*, 285-300.

[156] Ghosal, S.; Fluid mechanics of electroosmotic flow and its effect on band broadening in capillary electrophoresis. *J. Fluid Mech.* **2004**, *25*, 214-228.

[157] Sparreboom, W.; van der Berg, A.; Eijkel, J.C.T.; Transport in nanofluidic systems: a review of theory and applications. *N. J. of Phys.* **2010**, *12*, 015004-1–23.

[158] Zhang, J.; Todd, B.D.; Travis, K.P; Viscosity of confined inhomogeneous nonequilibrium fluids. *J. Chem. Phys.* **2004**, *121*, 10778-10786.

[159] Kroll, S.; Treccani, L.; Rezwan, K.; Grathwohl, G.; Development and characterisation of functionalised ceramic microtubes for bacteria filtration. *J. Membrane Sci.* **2010**, *365*, 447-455.

[160] E. L. Cussler. Typical values of diffusion coefficients. In *Diffussion Mass Transfer in Fluid Systems*; Crane, G. Ed.; Cambridge University Press: New York, USA, **2007**, 143.

.

J.C. Verde publications and patents

The following is the list of already published works authored by Jose Castaño Verde related to this thesis, presenting investigations of different aspects of micro and nanostructured materials:

- M.V. Ramallo, J.C. Verde, N. Cotón and F. Vidal, *Non-Ohmic Electrical Transport in the Vicinity of the Superconducting Transition: Implications for the Study of the Phase Diagram of the Underdoped Cuprate Superconductors*, J. Supercond. Nov. Magn., **28**, 323 (2014).
- F. Soto, C. Carballeira, J.M. Doval, J. Mosqueira, M.V. Ramallo, A. Ramos-Álvarez, D. Sóñora, J.C. Verde and F. Vidal. *Thermal fluctuations near a phase transition probed through the electrical resistivity of high-temperature superconductors*, Supercond. Sci. Technol. **28**, 085015 (2015).
- J.C. Verde, J.M. Doval, A. Ramos-Álvarez, D. Sóñora and M.V. Ramallo, *Resistive Transition of High-T_c Superconducting Films With Regular Arrays of T_c-Domains Induced by Micro- or Nanofunctionalization*, IEEE Trans. Appl. Supercond. **26**, 8800204 (2016).
- J.M. Doval, A. Ramos-Álvarez, D. Sóñora, J.C. Verde, M. Ruibal, J.A. Veira, J. Maza and F. Vidal, *Transition to the Normal State Induced by High Current Densities in High-T_c Superconductor Microbridges Under Applied Magnetic Fields*, IEEE Trans. Appl. Supercond. **26**, 8000805 (2016).
- A. Ramos-Álvarez, D. Sóñora, J.D. Dancausa, J.M. Doval, J.C. Verde, J. Mosqueira and F. Vidal, *A procedure to protect granular and porous samples from oxygen contamination in high resolution magnetization measurements: Application to granular High-T_c cuprate superconductors*, IEEE Trans. Appl. Supercond. **26**, 7201103 (2016).

- R. I. Rey, C. Carballeira, J.M. Doval, J. Mosqueira , M.V. Ramallo, A. Ramos-Álvarez, D. Sóñora, J.A. Veira, J.C. Verde and F. Vidal, *The conductivity and the magnetization around* T_c *in optimally-doped* $YBa_2Cu_3O_{7-\delta}$ *revisited: quantitative analysis in terms of fluctuating superconducting pairs*, Supercond. Sci. Technol. **32**, 045009 (2019).

Published books:

- J.C. Verde, M.V. Ramallo. Libro completo: *Películas micro- y nanoestructuradas de superconductores de alta temperatura: Computación de su transición resistiva.* GIDFI. ISBN: 978-1-68073-062-3 Santiago de Compostela, Spain, 2016.

Works in submission:

- J.C. Verde, C. Montero-Orille, A.S. Viz and M.V. Ramallo. *Calculations of doping nanostructuring and patterning to improve the functionality as ohmic bolometers of high-temperature superconductors*, submitted to Nanomaterials.

- J.C. Verde, A.S. Viz and M.V. Ramallo.. *Water nanofiltration using nanofunctionalized macropore media: Influence of the macropore geometry on the filtration performance and operational lifetime*, in preparation for submission in Phys. Rev. E.

Patent

- J.C. Verde, C. Montero-Orille, A.S. Viz and M.V. Ramallo. Spanish patent request with number P201930020 for ”Sensor bolométrico resistivo”. Institution: UNIVERSIDADE DE SANTIAGO DE COMPOSTELA. S/Ref: Bolómetros

Summary

This thesis is divided in two parts:

Part I presents novel results using a first-principle study of the high-temperature cuprate superconductor (HTS) materials, performed in the framework of a collaboration with Professor A.J. Leggett, in whose laboratory I performed different stays.

The study presents an extension, to the case of HTS, of equations originally derived for simple superconductors by G.V. Chester. They link the energy saved by the superconductivity with the structural properties of the materials. Then, we apply these extended equations to various prototypical HTS.

Part II is devoted to various applied studies in different micro and nanostructured functional materials and devices. We divided these studies in two groups: In part IIA, we focus again on HTS and propose structuration designs that optimize their functionality as bolometric sensors of electromagnetic radiation (a development that led to our Spain's patent application coded P201930020) and we also study other structured HTS systems (2D dot-pattern structured films; hybrid superconductor+piezoelectric films).

In part IIB, we study instead electrostatic nanostructured micropore (ENM) media of the type recently introduced by industry in various forms (among other, nanoalumina-coated microporous membranes) for filtration of nanofluids (liquids carrying nanoentities in suspension). By employing model equations previously developed in Santiago de Compostela, we find microgeometry configurations able to optimize the energy efficiency and performance of filters based on such media.